Studies of final states in small x deep inelastic scattering

Sabine Christiane Lang

Studies of Final States in Small x Deep Inelastic Scattering

A thesis submitted for the degree of
Doctor of Philosophy
by

Sabine Christiane Lang

University of Durham
Department of Mathematical Sciences
September 1997

Der kleine Gott ...
In jeden Quark begräbt er seine Nase.

Goethe, *Faust*

Abstract

We investigate the possibility of identifying $\ln(1/x)$ dynamics from studies of the final state in electron – proton deep inelastic scattering (DIS) in the small x region of the HERA collider at DESY. Motivated by recent observations at HERA we consider again the measurement of DIS events containing an identified forward jet as proposed by Mueller. We find that the shape of the x distribution of the data is described well by a prediction based on $\ln(1/x)$ dynamics.

Since forward jets are difficult to identify and measure accurately in the experiments we suggest the study of deep inelastic events containing an energetic isolated photon. We quantify the enhancement arising from the leading $\ln(1/x)$ gluon emissions with a view to using such events to identify the underlying dynamics in the small x regime at HERA.

To overcome the small event rate of jet + γ we propose that the forward jet may alternatively be identified through a single energetic decay product, the π^0. We investigate the feasibility of utilizing these deep inelastic + forward π^0 events as an indicator of the small x dynamics. Motivated by this study the H1 collaboration recently performed a DIS + π^0 measurement. Therefore we update our BFKL prediction imposing the H1 cuts in the calculation. We fix the normalisation by comparing with HERA data for DIS + jet.

Finally we study the transverse momentum (p_T) spectrum of charged particles produced in DIS at small Bjorken x in the central region between the current jet and the proton remnants. Again we normalize the BFKL prediction by comparing with the H1 DIS + jet data. We calculate the spectrum at large p_T with the BFKL $\ln(1/x)$ resummation included and then repeat the calculation with it omitted. We find that data favour the former.

Acknowledgements

Firstly, my deepest gratitude goes to my supervisor, Professor Alan Martin, for all his help during the last three years and for triggering my interest in small x physics.

I am equally indebted to Professor Jan Kwiecinski for his uncounted explanations and neverending patience. Thank you also for making my stay in Krakow so enjoyable.

I am grateful to Drs. Krzysztof Golec, Michael Kuhlen, Erwin Mirkes, Ewelina Mroczko and Peter Sutton for many interesting discussions on the subject of this thesis.

I would also like to express my thanks to the late Professor Euan Squires and Professor Wojciech Zakrzewski for supervision in the Department of Mathematical Sciences.

A big thank you goes to Claire Lewis for being such a good friend during my time in Durham. It was fun sharing a house, an office and a supervisor with you. Time to get those phones... I am also very grateful to Matthias Heyssler for being a very good friend. I appreciated our many delightful conversations and your help. Furthermore I would like to thank Elena Boglione — it was nice to share an office with you. Thanks also to everyone else on the top floor of the Physics Department for providing such a good atmosphere.

Finally, and most importantly, I would like to thank my family — Mama, Papa, Simone and Opa — for their love, encouragement and support without which this work would have never been possible.

Dedicated to
Mama, Papa, Simone and Opa
with love

Declaration

I declare that no material presented in this thesis has previously been submitted for a degree at this or any other university.

The research described in this thesis has been carried out in collaboration with Professors A. D. Martin and J. Kwiecinski. Chapters 1 and 2 provide an introduction to the subject and are not original. The material presented in Chapters 3 – 6 and 8 has been published as follows:

- *Deep inelasic events containing a forward photon as a probe of small x dynamics* J. Kwiecinski, S. C. Lang and A. D. Martin, Phys. Rev. **D54** (1996) 1874.
- *Forward π^0 trigger of the deep inelastic + jet probe of BFKL dynamics* J. Kwiecinski, S. C. Lang and A. D. Martin, Phys. Rev. **D55** (1997) 1273.
- *Single particle spectra in deep inelastic scattering as a probe of small x dynamics* J. Kwiecinski, S. C. Lang and A. D. Martin, Durham preprint DTP/97/56, hep-ph/9707240.

Contents

1 The structure of the proton **1**

1.1 From atoms to quarks 1

1.2 Deep inelastic scattering 3

1.2.1 Description of the cross section 6

1.3 The naive quark parton model 8

1.3.1 Bjorken scaling 9

1.3.2 Interpretation of x 9

1.3.3 Parton distributions 10

1.3.4 Structure functions 14

1.4 The QCD-improved parton model 16

1.4.1 QCD description of scaling violations 17

2 Resumming leading logarithms — evolution equations **22**

2.1 A second look at DGLAP evolution 22

2.2 The double leading logarithm approximation 25

2.3 BFKL evolution 27

2.3.1 The leading order BFKL equation 28

2.3.2 Analytic solution of the leading order BFKL equation 34

2.3.3 Properties of the leading order BFKL equation 36

2.3.4 Next-to-leading order corrections to the BFKL equation 38

2.4 Parton screening and the GLR equation 42

2.5 Summary 43

3 Deep inelastic events containing an identified forward jet 45

3.1 The DIS + forward jet measurement - Mueller's proposal 45

3.2 The cross section for deep inelastic + jet events 51

3.2.1 Calculation of the quark box diagram 54

3.2.2 Analytic form of the solution Φ of the BFKL equation for fixed α_S . 56

3.2.3 Numerical evaluation of Φ for running α_S 58

3.2.4 Predictions for the differential structure function 59

3.3 Cuts for the DIS + jet process 61

3.3.1 The HERA electron acceptance region 61

3.3.2 DIS + jet event kinematics 64

3.4 Summary and outlook 67

4 Deep inelastic events containing a forward photon 69

4.1 An alternative to the DIS + forward jet measurement 69

4.2 Basic QCD formula for the DIS + photon process 71

4.2.1 Calculation of the matrix element for the subprocess 72

4.2.2 The differential structure function for the DIS + γ process 73

4.3 Cuts to select the DIS + forward photon events 76

4.3.1 The isolation cut 77

4.3.2 The hemisphere cut 78

4.3.3 The beam pipe cut 79

4.4 Predictions for DIS + photon production 81

4.4.1 Dependence of the DIS + photon cross section on the cuts 81

4.4.2 The DIS + photon cross section 83

4.5 Discussion 85

5 Forward π^0 trigger of the deep inelastic + jet probe of BFKL dynamics 87

5.1 Proposal of the DIS + forward π^0 measurement 87

5.2 Fragmentation functions 89

5.2.1 Parton Model 89

5.2.2 Scaling violations 93

5.2.3 Determination of fragmentation functions from experiment 94

5.2.4 Relation between fragmentation functions for charged and neutral pions 96

5.3 QCD formalism for the DIS + forward π^0 process 97

5.3.1 The DIS + forward jet cross section – a reminder 97

5.3.2 The DIS + forward π^0 cross section 98

5.4 Cuts for the DIS + π^0 process 99

5.4.1 The hemisphere cut 100

5.4.2 The beam pipe cut 101

5.5 Predictions for the DIS + π^0 cross section 102

5.5.1 Dependence of the DIS + π^0 cross section on the k_π integration region and on the fragmentation scale 104

5.5.2 Background from photons which are fragments of the forward jet . 105

5.5.3 Comparison with the DIS + forward jet measurement 107

5.6 Discussion 109

6 Deep inelastic + jet — comparison with the data 110

6.1 Motivation 110

6.2 Description of the DIS + forward jet data 111

6.2.1 Calculation of the DIS + jet cross section 111

6.2.2 Cuts imposed by the H1 collaboration 112

6.2.3 Normalisation of the BFKL prediction 114

6.3 Predictions for the cross section for DIS + jet events 114

6.3.1 Comparison with the data for different cuts on k_{jT} 116

6.3.2 Dependence on the cuts on the transverse momentum integration in the BFKL equation 117

6.3.3 Effect on the DIS + jet cross section of varying the charm quark mass 117

6.4 Summary and conclusion 119

7 An update of the DIS + π^0 prediction 121

7.1 Motivation 121

7.2 Calculation of the DIS + π^0 cross section 122

7.2.1 Normalizing the solution Φ of the BFKL equation 123

7.2.2 Cuts imposed in the calculation of the cross section 123

7.3 New predictions for the DIS + π^0 cross section 126

7.3.1 Comparison of the DIS + π^0 cross sections obtained including and neglecting BFKL evolution 127

7.3.2 A comment on the new cuts 129

7.3.3 Comparison with the DIS + forward jet rate 133

7.4 Comparison with the H1 data 135

7.5 Summary and conclusions 137

8 Single particle spectra in DIS as a probe of small x dynamics 140

8.1 Focussing on the diffusion in $\ln k_T^2$ accompanying BFKL evolution 140

8.2 Formalism for charged particle production 142

8.2.1 Normalisation of the prediction 142

8.2.2 The cross section for charged particle production 143

8.3 Predictions for the single particle p_T spectra 145

8.3.1 Calculation of the single particle spectrum 146

8.3.2 Comparison with the H1 data 147

8.4 A closer look at the single particle p_T spectra 151

8.4.1 Contributions to the spectrum from the three different regions . . . 151

8.4.2 The pseudorapidity interval 153

8.5 Conclusion 156

9 Summary and conclusions **157**

A Analytic solution of the BFKL equation for fixed coupling **162**

B Calculation of the Mellin transform of the BFKL kernel **167**

Bibliography **169**

Chapter 1

The structure of the proton

1.1 From atoms to quarks

For the last one hundred years great effort has been devoted to the investigation of the structure of matter [1]. Already in the nineteenth century molecules were found to be made up from *atoms*. That these atoms themselves have substructure became apparent soon after with the first step being provided by the discovery of the *electron* in 1897. A few years later Rutherford and collaborators performed their famous experiments in which they let α particles scatter off gold foil. That the α particles were reflected at much larger angles than one would expect if atoms were the basic constituents of matter led him to propose that the atoms themselves were built up from even smaller constituents in 1911. It seemed an atom contains a massive *nucleus* and large regions of empty space. This discovery triggered a lot of theoretical and experimental work. On the theoretical side models for the atom were developed and non-relativistic quantum mechanics was formulated. The new theory turned out to be quite successful as it indeed allowed for a description of previously unexplained experimental data concerning the spectra of hydrogen, the inelastic scattering of electrons off atoms and x-ray scattering. However, the non-relativistic quantum mechanics predictions were based on the assumption that the nucleus is pointlike. That this is not the case was indicated by the discovery of the neutron

[1] We can only provide a short overview here. More detailed reviews may be found in [1] and [2].

in 1932 combined with the results of the SLAC experiments in which now higher energy electron beams where elastically scattered off atoms. The nucleus was then thought of as made up from *nucleons*, i.e. from protons and neutrons that had to be held together by a new force which unlike the electromagnetic force also acts on electrically neutral objects and which extends over the dimensions of the nucleon. This new force was named the *strong* force because it had to be strong enough to overcome the Coulomb repulsion between protons and to hold the nucleons together within the small volume of the nucleus. Later, with the discovery of more and more new particles, a classification for strongly interacting particles was introduced. These so-called *hadrons* were divided according to their spin into *baryon* which are fermions and *mesons* which are bosons. In 1964 Gell-Mann [3] and Zweig [4] both proposed that hadrons may still not be the fundamental objects, but rather the fundamental building blocks are spin-$\frac{1}{2}$ particles with fractional charges which they called *quarks*. In their theory baryons are composed from three quarks and mesons from a quark (q) and an antiquark ($\overline{q}$). The quarks are characterized by their *flavour* which can assume six different values, up (u), down (d), charm(c), strange (s), top (t) and bottom (b). So a proton, for example, has the quark content uud and a K^+ meson $u\overline{s}$. This quark model allowed an explanation of the properties of hadrons, however, since there was no experimental evidence for the existence of quarks, it was generally simply regarded as a helpful mathematical framework. That hadrons indeed have substructure was only revealed in the experiments at the Stanford electron linear accelerator (SLAC) which were started in 1968. With the help of a high energy electron beam pointlike constituents were found in the proton which were named *partons*. Soon after it became clear that these partons were nothing else but the quarks of Gell-Mann and Zweig.

Our modern day understanding of the structure of hadrons evolved out of the need to find explanations for some problems which the quark model left unsolved. Firstly, it was not clear why only the combinations qqq and $q\overline{q}$ occured and not, for example, qq. Secondly, no free quarks had been observed. A third problem arose when the Δ^{++} resonance was discovered which has spin $\frac{3}{2}$ and quark content uuu. The three u quarks can be in a state where their spins are parallel, but this state then violates the exclusion principle. A solution to this problem is the introduction of a new quantum number,

colour. If colour assumes three different values – blue, green and red, say – the Δ^{++} can be antisymmetric in its colour wavefunction and therefore obeys the exclusion principle. The proposal of colour has a second advantage: it in fact leads to the solution of the other two problems which we mentioned above if one also postulates that hadrons are colour singlets (or *colourless*) under the non-Abelian SU(3) colour symmetry group. As a consequence of the introduction of colour a new gauge theory was developed, namely *Quantum Chromodynamics* (QCD).

QCD describes the interaction between quarks and *gluons*. The gluons are massless bosons whose role is similar to the role of the photon in Quantum Electrodynamics (QED). However, unlike the photon in QED, gluons carry colour charge themselves which allows them to interact *amongst each other* rather than only with quarks. QCD is a *non-Abelian* theory. As a direct consequence of the self-coupling of gluons in QCD colour charges are "antiscreened" in contrary to the charge screening of the electric charge in QED. This means that as the distance between two quarks or gluons increases the colour force between them also increases. So it follows naturally that they are *confined* inside the hadron and that the observation of free quarks is not possible. If, on the other hand, the distance between two field quanta is decreased the colour force decreases which implies that at very short distances the quarks inside a hadron behave as quasi-free particles. This property is called *asymptotic freedom* and forms the basis of perturbative QCD calculations. QCD has already proved very successful in describing many hadronic phenomena. However, as we will discuss in this thesis, the DESY electron – proton collider HERA offers us the opportunity to probe QCD in a new, previously unexplored kinematic regime. In particular we will study the QCD prediction for the quark and gluon content of the proton in the so-called "small x" region.

1.2 Deep inelastic scattering

Above we saw that with the increasing energy of the probe successive layers of substructure inside matter could be revealed. So to investigate the structure of the proton obviously a very energetic probe is needed. The best conditions for probing the proton are provided

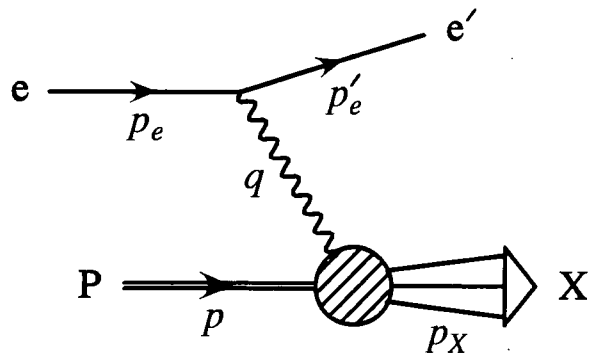

Figure 1.1: Inelastic electron - proton scattering in the one photon exchange approximation.

by deep inelastic lepton – proton scattering [2] which we will now discuss. For simplicity we will concentrate on the deep inelastic scattering of an electron (or positron) off the proton, that is the process $ep \to eX$. Here X represents all fragments of the proton which occur in the final state. The process is shown diagrammatically in Fig. 1.1. The proton p can be at rest as in the fixed target experiments or in motion as in collider experiments. The four momenta of the proton, the incoming electron and the scattered electron are p, p_e and p'_e, respectively. We neglect the electron mass. The incoming electron emits a virtual photon of four momentum q which probes the proton. We define the virtuality Q^2 of the photon by

$$Q^2 \equiv -q^2 = -(p_e - p'_e)^2 \tag{1.1}$$

where then $Q^2 > 0$. At large Q^2 the probe could also be a Z boson. However, we will assume here that $Q^2 \ll M_Z^2$ – which is the case for the processes under consideration in this thesis – and neglect the contribution from Z exchange. The higher Q^2 the more substructure the photon can resolve in the proton and eventually the partonic constituents of the proton will become "visible". In fact, the expression "deep" in deep inelastic scattering (DIS) means that $Q^2 \gg M_P^2$ where M_P is the mass of the proton. The scattering is called "inelastic" when the invariant mass of the hadrons in the final state $W^2 = (p+q)^2 \gg M_P^2$.

What is the energy loss ν of the electron when it emits the photon? To calculate ν we

[2] Reviews of deep inelastic lepton – proton scattering can for example be found in refs. [1, 2, 5 – 8].

consider the scattering in the proton rest frame which is equal to the laboratory frame for fixed target experiments. In this frame the incoming and outgoing electron have energy E_e and E'_e, respectively, and therefore $\nu = E_e - E'_e$. The photon, the proton and the hadronic final state have the four momenta

$$q = (\nu, \boldsymbol{q}), \qquad p = (M_P, \mathbf{o}), \qquad p_X = (M_P + \nu, \boldsymbol{q}) \tag{1.2}$$

in the proton rest frame. In the case of elastic scattering the mass on-shell condition for the intact proton is then given by

$$p_X^2 = (M_P + \nu)^2 - \boldsymbol{q}^2 = M_P^2. \tag{1.3}$$

Using $q^2 = \nu^2 - \boldsymbol{q}^2$ we find

$$\nu = \frac{Q^2}{2M_P} \tag{1.4}$$

and the frame invariant definition

$$\nu = \frac{p \cdot q}{M_P}. \tag{1.5}$$

The scattering can be described completely in terms of the variables Q^2 and ν.

As we shall see it is, however, convenient to introduce the dimensionless variable *Bjorken* x, which is defined as

$$x \equiv \frac{Q^2}{2M_P\nu}. \tag{1.6}$$

Evaluating the denominator using (1.2) we find

$$x = \frac{Q^2}{2p \cdot q}. \tag{1.7}$$

We will give an interpretation of x below. Another independent dimensionless variable describing the process is

$$y \equiv \frac{p \cdot q}{p \cdot p_e}. \tag{1.8}$$

Evaluating this expression in the proton rest frame we find $y = \nu/E_e$ which shows that y corresponds to the fractional energy loss of the electron in this frame. Both x and y are limited to the interval $[0, 1]$. That $x \leq 1$ can be seen in the following way. Baryon

number conservation implies that the invariant mass of the final state hadrons is at least as large as the proton mass. Therefore

$$W^2 = (p+q)^2 \geq M_P^2 \tag{1.9}$$

which after substituting the expressions for the momenta given in (1.2) yields

$$2M_P\nu \geq Q^2. \tag{1.10}$$

Note that $2M_P\nu = Q^2$, i.e. $x = 1$, corresponds to elastic scattering.

1.2.1 Description of the cross section

We will focus now on the simplest cross section which can be measured in an experiment, the so-called "inclusive" cross section, in which only the outgoing electron is observed in the final state. The inclusive cross section is the sum of the cross sections for all possible hadronic final states. In Fig. 1.1 the sum of all hadronic final states was represented by X. We consider the case where the electron is unpolarized. Investigating the structure of the S-matrix element for the process depicted in Fig. 1.1 one finds that the inclusive cross section can be written as the product of a lepton tensor $L_{\mu\nu}$ and a hadron tensor $W^{\mu\nu}$ [5],

$$d\sigma \sim L_{\mu\nu} W^{\mu\nu}. \tag{1.11}$$

The lepton tensor $L_{\mu\nu}$ describes the emission of the virtual photon by the electron, i.e. the top part of the diagram in Fig. 1.1. It can be calculated in quantum electrodynamics with the help of the Feynman rules. We obtain

$$\begin{aligned} L_{\mu\nu} &= \frac{1}{2} \sum_{spins} \left[\overline{u}(p'_e)\gamma_\mu u(p_e)\right] \left[\overline{u}(p'_e)\gamma_\nu u(p_e)\right]^* \\ &= 2\left[p_{e\mu}p'_{e\nu} + p'_{e\nu}p_{e\mu} - g_{\mu\nu}(p'_e \cdot p_e)\right]. \end{aligned} \tag{1.12}$$

The hadron tensor $W^{\mu\nu}$ contains all information concerning the interaction of the virtual photon with the proton, i.e. the lower part of the diagram in Fig. 1.1. We have [5]

$$\begin{aligned} W^{\mu\nu} &= \sum_X \frac{1}{2M_P} (2\pi)^3 \, \delta(p_X - p - q) \\ &\quad \times \sum_{spins'} \langle P(p)|J^\mu(0)|X(p_X)\rangle \langle X(p_X)|J^\nu(0)|P(p)\rangle \end{aligned} \tag{1.13}$$

where the sum runs over the final spins and where J^μ is the electromagnetic current. Since we sum over all final states and since we consider only unpolarized protons, $W^{\mu\nu}$ can only depend on the four momenta p and q. We write down the most general tensor form for $W^{\mu\nu}$ which can be formed from the two four momenta [6, 7]:

$$W^{\mu\nu} = -W_1 g^{\mu\nu} + \frac{W_2}{M_P^2} p^\mu p^\nu + \frac{W_4}{M_P^2} q^\mu q^\nu + \frac{W_5}{M_P^2}(p^\mu q^\nu + q^\mu p^\nu). \tag{1.14}$$

Here we omitted a term depending on the antisymmetric tensor $\epsilon_{\mu\nu\rho\tau}$ which does not contribute here because the electromagnetic current J^μ on which $W^{\mu\nu}$ depends does not violate parity. We can simplify (1.14) by noting that J^μ is a hermitian operator and by requiring conservation of the electromagnetic current, that is $\partial_\mu J^\mu = 0$. Proceeding in this way we find that only two of the four terms in (1.14) are independent. We then have

$$W^{\mu\nu} = W_1 \left(-g^{\mu\nu} + \frac{q^\mu q^\nu}{q^2}\right) + \frac{W_2}{M_P^2}\left(p^\mu - \frac{p\cdot q}{q^2} q^\mu\right)\left(p^\nu - \frac{p\cdot q}{q^2} q^\nu\right). \tag{1.15}$$

W_1 and W_2 are unknown scalar functions which depend on the two independent Lorentz invariants that we can form from p and q. Often used are Q^2 and ν, or we could also take Q^2 and x which was defined in (1.6). The functions W_1 and W_2 parametrize our ignorance about the structure of the proton. They can be measured in deep inelastic scattering experiments and, in principle, can be calculated from QCD. If we substitute (1.15) and (1.12) into the expression (1.11) for the unpolarized cross section and include the flux factor and the phase space factor for the outgoing electron, we find [6]

$$\frac{d\sigma}{dE_e' d\Omega} = \frac{\alpha^2}{4E_e^2 \sin^4(\theta_{ee}/2)}\left[W_2(\nu, q^2)\cos^2\frac{\theta_{ee}}{2} + 2W_1(\nu, q^2)\sin^2\frac{\theta_{ee}}{2}\right] \tag{1.16}$$

in the proton rest frame. Here E_e' is the energy of the scattered electron and θ_{ee} its angle with respect to the direction of the incoming electron. Recall that we neglected the electron mass.

1.3 The naive quark parton model

We now extend our study of deep inelastic scattering concentrating on a particular model, the so-called *parton model* [9]. The parton model is based on the assumption that a fast moving proton appears as a collection of partons which travel in approximately the same direction. These partons share the proton's three momentum. If the wavelength of a virtual photon probe is short enough, i.e. Q^2 large, it sees the proton as consisting of non-interacting quarks and is being absorbed by a single quark which appears to be pointlike. The interaction of the photon with the proton can then be expressed as the sum of the incoherent scatterings off all charged partons within the proton. This is called the *impulse approximation.* In the parton model we can represent deep inelastic *ep* scattering by the diagram shown in Fig. 1.2 where we indicated that the virtual photon scatters off a single quark inside the proton.

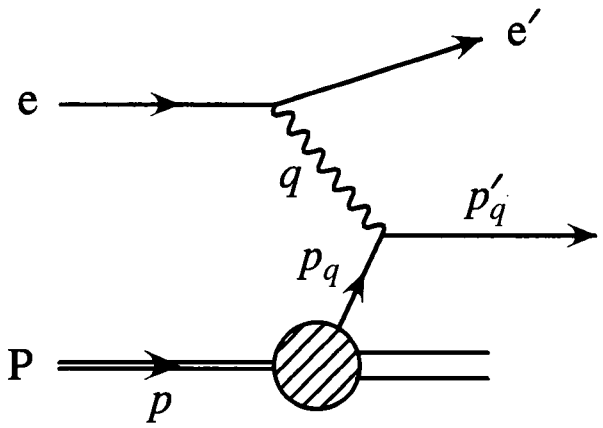

Figure 1.2: Deep inelastic *ep* scattering in the parton model.

Despite its introduction prior to the arrival of quantum chromodynamics, the parton model is still of importance today. In this section we will introduce some observables which are used to describe the structure of the proton within the framework of the parton model. We will extend these ideas in the following section where we will include QCD corrections.

1.3.1 Bjorken scaling

We already mentioned that as Q^2 increases the photon probe sees a parton inside the proton as pointlike. The inelastic electron - proton scattering can then be interpreted as the elastic scattering of an electron off a quark. If the parton appears as pointlike there is no dimensionful scale describing the scattering. This implies that the functions W_1 and W_2 which we introduced in (1.15) must be dimensionless. They can therefore not depend on ν and Q^2 separately but only on the ratio of these two variables. In 1969 Bjorken [10] showed that in the limit

$$Q^2 \to \infty, \qquad \nu \to \infty \tag{1.17}$$

with $x = Q^2/2M_P\nu$ fixed, W_1 and W_2 become functions of the dimensionless variable x and do not depend on Q^2. This property is called *Bjorken scaling.* In the limit (1.17) we have

$$M_P W_1(\nu, Q^2) \to F_1(x) \tag{1.18}$$

$$\nu W_2(\nu, Q^2) \to F_2(x). \tag{1.19}$$

So if the functions F_1 and F_2 are measured in an experiment they should not vary with Q^2. We will see if this is the case in Section 1.4.

1.3.2 Interpretation of x

Deep inelastic scattering in the parton model is often studied in the so-called infinite momentum frame in which the proton is travelling very fast. We can choose the direction of motion of the proton as the z-axis. Then the four momentum of the proton $p^\mu \simeq (p, 0, 0, p)$ with $p \gg M_P$. Since the proton moves very fast its constituents have to travel in approximately the same direction for the proton to remain whole. This implies that the transverse components of the struck parton's momentum can be neglected, and its momentum can therefore be written as

$$p_q^\mu = \xi p^\mu. \tag{1.20}$$

Since the parton model assumes that the parton stays close to its mass shell both before and after the interaction we have the following mass shell constraint for the scattered parton:

$$m_q^2 = p_q'^2 = (\xi p + q)^2 \simeq 2p \cdot q\, \xi - Q^2. \tag{1.21}$$

Here we neglected the proton mass since $p \gg M_P$ due to our choice of frame. For $Q^2 \gg m_q^2$, the mass of the parton, we then find

$$\xi = \frac{Q^2}{2p \cdot q} = x. \tag{1.22}$$

We see that the kinematic variable x which we introduced earlier in the parton model can be interpreted as the fraction of the proton's momentum which is carried by the struck quark in the infinite momentum frame.

1.3.3 Parton distributions

Now we know that if the momentum p of the proton is large compared to the masses of the particles involved in the scattering the fraction of the proton's momentum which the struck quark carries is equal to x. But what is the probability that a quark has a certain momentum fraction? We define the *parton distribution* $f_i(x)$ as the probability of finding a parton i in the proton with a fraction x of its momentum. That is $f_i(x)dx$ is the number of partons of type i which have a momentum between xp and $(x + dx)p$. We will use the following notation: we write the u-quark distribution

$$f_u(x) \equiv u(x) \tag{1.23}$$

and analogously for all other quark and antiquark flavours and the gluon.

In the original quark model of Gell-Mann and Zweig the quark content of the proton is *uud*. These three quarks are referred to as *valence* quarks. They carry the quantum numbers of the proton. However, we have to also allow these valence quarks to radiate gluons. Via the pair creation mechanism the gluons can then produce additional quark-antiquark pairs which are called *sea* quarks. Therefore the probability of finding for

example a u-quark inside the proton is given by the sum of the probabilities of finding a valence quark u_V and a sea quark u_S. In our notation

$$u(x) = u_V(x) + u_S(x) \tag{1.24}$$

and for a $\overline{u}$-quark

$$\overline{u}(x) = u_S(x). \tag{1.25}$$

When the proton is probed at a scale Q the sea quarks of all flavours with $m_q \lesssim Q$ can be found.

The parton model does not predict the magnitude of the parton distributions, they have to be obtained from experiment. Nevertheless there are some straightforward constraints.

Sum rules

We have already mentioned that the quantum numbers of the proton, that is charge, baryon number and strangeness, are carried by the valence quarks. The correct quantum numbers are obtained for two valence u-quarks and one valence d-quark inside the proton, and therefore we have

$$\int_0^1 dx\,[u(x) - \overline{u}(x)] = \int_0^1 dx\, u_V(x) = 2 \tag{1.26}$$

$$\int_0^1 dx\,[d(x) - \overline{d}(x)] = \int_0^1 dx\, d_V(x) = 1 \tag{1.27}$$

$$\int_0^1 dx\,[s(x) - \overline{s}(x)] = 0. \tag{1.28}$$

Furthermore, the momenta of all partons inside the proton must add up to the momentum p of the proton, i.e.

$$\sum_i \int_0^1 dx\, xp\, f_i(x) = p, \tag{1.29}$$

which implies that

$$\sum_i \int_0^1 dx\, x\, f_i(x) = 1. \tag{1.30}$$

These sum rules already provide us with some constraints on the parton distributions but so far we have not fixed their shape in x.

Behaviour in the limits $x \to 1$ and $x \to 0$

Additional information on the parton distributions can be obtained by studying their behaviour as $x \to 0$ or 1. We start by considering the limit $x \to 1$. In this case we can predict the x dependence of the parton distributions by applying spectator counting rules [11]. The idea is to count the number of partons which do not take part in the interaction, the so-called spectators. If $x \to 1$ for one parton then this parton must carry almost all of the proton's momentum while the spectators share the remaining fraction. So clearly the parton distribution has to vanish as $x \to 1$. Also hard gluon exchanges between the valence quarks are necessary to transfer most of the proton's momentum to one parton. The spectator counting rules predict that the distribution for parton i behaves as [7]

$$f_i(x) \sim (1-x)^{2n_s-1} \tag{1.31}$$

as $x \to 1$. Here n_s is the minimum number of spectators present in the proton. Let us for example consider the distribution of a valence quark in the proton. Then $n_s = 2$ since there are at least two spectators, namely the other two valence quarks. This is shown symbolically in Fig. 1.3(a) where the parton whose distribution we are studying is marked by an arrow. There we also indicated the hard gluon exchanges. Figs. 1.3(b) and (c) indicate n_s for the gluon and the sea quark distributions. In summary the counting rules predict

$$\begin{aligned} q_V(x) &\sim (1-x)^3 \\ q_S(x) &\sim (1-x)^7 \\ g(x) &\sim (1-x)^5 \end{aligned} \tag{1.32}$$

as $x \to 1$.

The behaviour in the limit $x \to 0$, on the other hand, is given by *Regge theory*, a theory which allowed for the description of the scattering of strongly interacting particles before the advent of QCD. Regge theory predicts that the total cross section of an elastic scattering process behaves as

$$\sigma_{tot} \sim s^{\alpha(0)-1} \tag{1.33}$$

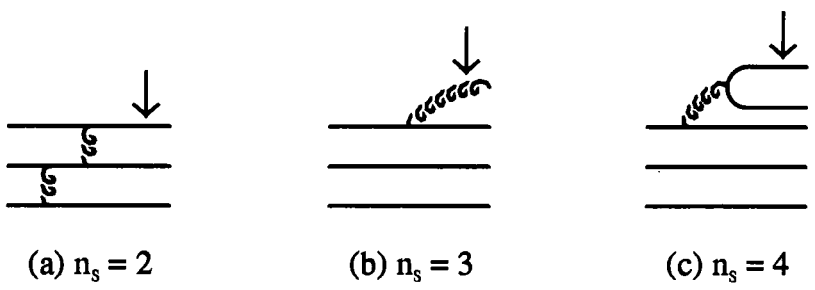

Figure 1.3: The minimum number of spectators, n_s, for (a) a valence quark, (b) a gluon, and (c) a sea quark. The parton under consideration is marked by an arrow.

at high energies where s is the centre-of-mass energy squared. Here $\alpha(0)$ is the *intercept* of a *Regge trajectory* which is an approximately linear function in the Mandelstam variable t, the (negative of the) four momentum transfer squared, that is

$$\alpha(t) \simeq \alpha(0) + \alpha' t. \tag{1.34}$$

A Regge trajectory relates the mass m of a particle with its spin J. For $t > 0$ particles with similar quantum numbers lie on (approximately exchange degenerate) Regge trajectories with

$$\alpha(m^2) = J \tag{1.35}$$

at integer values of J. More detail can for example be found in refs. [12, 13]. Of importance here is that Regge theory also predicts the x dependence of the parton distributions as $x \to 0$ in terms of trajectories. We have [7]:

$$\begin{aligned} q_V(x) &\sim x^{-\alpha_R(0)} \\ q_S(x) &\sim x^{-\alpha_{I\!P}(0)} \\ g(x) &\sim x^{-\alpha_{I\!P}(0)} \end{aligned} \tag{1.36}$$

as $x \to 0$ where α_R is the so-called leading meson trajectory with intercept $\alpha_R(0) \simeq \frac{1}{2}$ and $\alpha_{I\!P}$ is the soft Pomeron trajectory with $\alpha_{I\!P}(0) \simeq 1$.

Together with the sum rules the constraints (1.32) and (1.36) in the limits $x \to 0$ and 1 can be used to develop physically reasonable parametrisations for parton distributions which only depend on x.

1.3.4 Structure functions

Once we know the parton distributions we can obtain the cross section for deep inelastic ep scattering in the parton model. In this model we can express the cross section for this process as the incoherent sum of the cross sections for all possible electron - parton scatterings weighted by the probability that a parton carrying a fraction ξ of the proton's momentum is struck inside the proton. Choosing x and Q^2 as the two independent variables we have the differential cross section

$$\frac{d^2\sigma}{dxdQ^2} = \sum_q \int_0^1 d\xi \, f_q(\xi) \, \frac{d^2\hat{\sigma}_{eq}}{dxdQ^2} \tag{1.37}$$

where the sum runs over all quark and antiquark flavours. We indicate by a hat the variables for the partonic eq subprocess. The cross section for eq scattering can be calculated and one finds [6, 7]

$$\frac{d\hat{\sigma}_{eq}}{d\hat{t}} = \frac{2\pi\alpha^2 e_q^2}{\hat{s}^2} \left(\frac{\hat{s}^2 + \hat{u}^2}{\hat{t}^2} \right) \tag{1.38}$$

with e_q the charge of quark q in units of the electron charge e. We evaluate the invariants for the partonic subprocess neglecting masses in the following way:

$$\begin{aligned} \hat{s} &= (p_q + p_e)^2 = (xp + p_e)^2 \simeq 2xp \cdot p_e \simeq xs \\ \hat{t} &= (p_e - p_e')^2 = -Q^2 \simeq -xys \\ \hat{u} &= -\hat{s} - \hat{t} = -x(1-y)s. \end{aligned} \tag{1.39}$$

Here we used the centre-of-mass energy squared $s = (p+p_e)^2 \simeq 2p \cdot p_e$ which we substituted in (1.8) to obtain

$$y \simeq \frac{2p \cdot q}{s} = \frac{Q^2}{xs}. \tag{1.40}$$

Utilizing expressions (1.39) we can simplify (1.38) to give

$$\frac{d\hat{\sigma}_{eq}}{dQ^2} = \frac{2\pi\alpha^2 e_q^2}{Q^4} \left[1 + (1-y)^2 \right]. \tag{1.41}$$

Since as we showed above $x = \xi$ we can introduce a δ-function $\delta(x - \xi)$ in (1.41) and take the differential in x. Then we substitute the resulting expression into (1.37) leading to

$$\frac{d^2\sigma}{dxdQ^2} = \frac{4\pi\alpha^2}{xQ^4} \sum_q \int_0^1 d\xi \, f_q(\xi) \, e_q^2 \, \frac{x}{2} \left[1 + (1-y)^2 \right] \delta(x - \xi) \tag{1.42}$$

for the *ep* cross section.

On the other hand we can also derive an expression for the cross section $d^2\sigma/dxdQ^2$ from $L_{\mu\nu}$ and $W^{\mu\nu}$ given in (1.12) and (1.15), respectively. Instead of W_1 and W_2 it is convenient to introduce the *structure functions* F_1 and F_2, given by

$$F_1 \equiv M_P W_1 \tag{1.43}$$

$$F_2 \equiv \frac{p\cdot q}{M_P} W_2. \tag{1.44}$$

Substituting into (1.15) we obtain [6, 7]

$$\frac{d^2\sigma}{dxdQ^2} = \frac{4\pi\alpha^2}{xQ^4}\left[y^2 x\, F_1(x) + (1-y)\, F_2(x)\right] \tag{1.45}$$

for $s \gg M_P^2$. Simply rewriting the equation we find

$$\frac{d^2\sigma}{dxdQ^2} = \frac{4\pi\alpha^2}{xQ^4}\left\{\frac{1}{2}y^2\left[2xF_1(x) - F_2(x)\right] + \frac{1}{2}\left[1+(1-y)^2\right]\, F_2(x)\right\}. \tag{1.46}$$

Now, however, we notice that we have derived two expressions for the cross section for deep inelastic *ep* scattering, (1.42) and (1.46). We compare the coefficients of $[1+(1-y)^2]$ and y^2 in the two equations and obtain the structure functions in the parton model:

$$F_2(x) = \sum_q e_q^2 x f_q(x) \tag{1.47}$$

$$F_1(x) = \frac{F_2(x)}{2x}. \tag{1.48}$$

Equation (1.48) is known as the Callan-Gross relation and is a property of the spin-$\frac{1}{2}$ nature of the quarks. Note that F_1 and F_2 only depend on x, not on Q^2; we say that they show Bjorken scaling. Although the first measurements at SLAC [14] confirmed this and led to the parton model, subsequent more precise measurements [15, 16] showed that Bjorken scaling is violated. In the following section we will see why this is the case.

1.4 The QCD-improved parton model

Above we found that in the naive quark parton model the structure functions are independent of Q^2. Let us now imagine we probe the proton with a photon whose virtuality Q^2 is even higher. As Q^2 increases the photon not only resolves the valence quarks but also gluons and sea quarks. This means that an increasing number of partons is sharing the proton's momentum. Therefore, the higher Q^2 the more likely it is to find partons with small momentum fraction x and the less likely it is to discover partons with high x. This implies that the parton distributions, and therefore the structure function F_2, rise with Q^2 at small x and fall with Q^2 at high x. In perturbative QCD we can calculate these

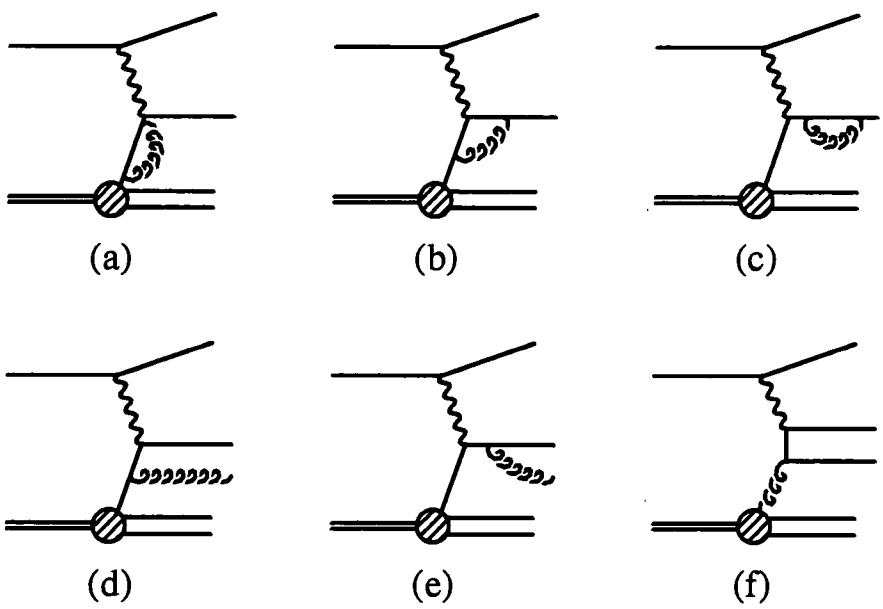

Figure 1.4: The $\mathcal{O}(\alpha_S)$ contributions to deep inelastic ep scattering from (a) – (c) virtual gluons, (d) – (e) real gluons, and (f) a gluon inside the proton.

scaling violations if Q^2 is large enough for the strong coupling constant α_S to be small. Then the parton model diagram Fig. 1.2 corresponds to the leading order expression and we have to include the $\mathcal{O}(\alpha_S)$ contributions. The processes contributing to deep inelastic ep scattering at $\mathcal{O}(\alpha_S)$ are shown diagrammatically in Fig. 1.4. Diagrams (a) – (c) represent the virtual gluon contributions whereas diagrams (d) and (e) show contributions due

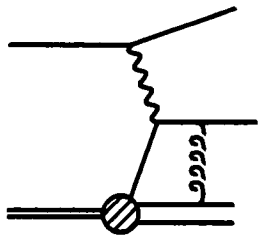

Figure 1.5: A higher twist contribution to deep inelastic ep scattering.

to the emission of real gluons. Note that at $\mathcal{O}(\alpha_S)$ the virtual photon can interact with a gluon in the proton via a quark - antiquark pair (γg fusion), see Fig. 1.4(f). Actually at this order the struck quark could also interact with a quark in the final state as is shown in Fig. 1.5. These final state interactions are referred to as higher twist contributions and are suppressed by a factor $\sim 1/Q^2$ compared to the diagrams in Fig. 1.4 [8]. Therefore the parton model assumption that the timescale on which the interaction of the photon with a parton occurs is a lot shorter than the interaction time for partons inside the proton is still true here if Q^2 is large. Hence we can work in the framework of the *QCD-improved parton model.*

1.4.1 QCD description of scaling violations

Above we explained that QCD predicts that Bjorken scaling is violated and that the structure function F_2 depends on Q^2. As we shall now see, QCD does not tell us the absolute value of F_2 for a given Q^2, rather it describes how F_2 varies with Q^2 from a given input.

In the previous section we found that in the quark parton model F_2 is given by (1.47) which we can rewrite in the form

$$\begin{aligned} \frac{F_2}{x} &= \sum_q \int_0^1 d\xi \, q(\xi) \, e_q^2 \, \delta(\xi - x) \\ &= \sum_q \int_0^1 \frac{d\xi}{\xi} \, q(\xi) \, e_q^2 \, \delta\left(1 - \frac{x}{\xi}\right). \end{aligned} \tag{1.49}$$

The effect of including the $\mathcal{O}(\alpha_S)$ contributions due to emission of real gluons (Figs. 1.4(d)

and (e)) can be calculated in perturbative QCD with the result [2]

$$\frac{F_2(x,Q^2)}{x} = \sum_q \int_0^1 \frac{d\xi}{\xi} q(\xi)\, e_q^2 \left\{ \delta\left(1-\frac{x}{\xi}\right) + \frac{\alpha_S}{2\pi} P_{qq}\left(\frac{x}{\xi}\right) \ln\left(\frac{Q^2}{\mu^2}\right) \right\}. \tag{1.50}$$

Here P_{qq} is a so-called *splitting function* which can be calculated using perturbative QCD. We will explain its meaning below. The $\ln(Q^2/\mu^2)$ arises from the integration over the transverse momentum squared k_T^2 of the emitted gluon. We have

$$\int_{\mu^2}^{Q^2} \frac{dk_T^2}{k_T^2} = \ln\left(\frac{Q^2}{\mu^2}\right) \tag{1.51}$$

where we introduced an arbitrary lower limit μ^2 to avoid integrating over the singularity at $k_T = 0$ which corresponds to the gluon being emitted collinearly to the parent quark. So (1.50) contains an arbitrary parameter and a potentially singular term $\ln(Q^2/\mu^2)$. However, we are able to restore the perturbative expansion by factoring the initial state singularities into redefined parton distributions at some mass scale M^2 (which depends on the factorisation scheme used). This procedure introduces the Q^2 dependence into the parton distributions which now have the form

$$q(x,Q^2) = q(x) + \frac{\alpha_S}{2\pi} \int_x^1 \frac{d\xi}{\xi} q(\xi,Q^2)\, P_{qq}\left(\frac{x}{\xi}\right) \ln\left(\frac{Q^2}{\mu^2}\right). \tag{1.52}$$

F_2/x then has the same form as (1.49) but with $q(\xi) \to q(\xi,Q^2)$. The running parton densities $q(x,Q^2)$ are finite because F_2 is an observable. They have the important property of universality which we will now briefly explain. The factorisation theorem tells us that a hadronic cross section can be written as the product of the parton density which contains all information on the soft process and the partonic cross section $\hat{\sigma}_i$ which describes the hard scattering [17]. We have

$$\sigma = \sum_i f_i \otimes \hat{\sigma}_i \tag{1.53}$$

where f_i is the density of parton i, $f_i = q_i$ or g. The hard scattering term $\hat{\sigma}_i$ can be calculated from perturbative QCD. It depends on the partonic process under consideration but is independent of the hadron which contains the interacting parton. The parton densities on the other hand are *universal.* This means that they are independent of the partonic process. They only depend on the parent hadron, so for example the u quark

density inside the pion differs from that in the proton. Therefore the same parton densities can be used both in hadron – hadron and in hadron – lepton interactions.

How do the parton densities vary with Q^2? If we differentiate (1.52) we find

$$\frac{\partial q(x,Q^2)}{\partial \ln(Q^2/Q_0^2)} = \frac{\alpha_S}{2\pi}\int_x^1 \frac{d\xi}{\xi}\, q(\xi,Q^2)\, P_{qq}\left(\frac{x}{\xi}\right). \tag{1.54}$$

This is a *DGLAP equation* (Dokshitzer-Gribov-Lipatov-Altarelli-Parisi) [18, 19]. It tells us how a parton distribution evolves with Q^2 once we know its x dependence at some scale Q_0^2. (In the following we set $Q_0^2 = 1$ GeV^2.) These "starting distributions" $q(x,Q_0^2)$ are not given by perturbative QCD and at present have to be determined from experiment.

Let us now return to the splitting function P_{qq}. An interpretation of P_{qq} can be found by defining the function

$$P_{q\leftarrow q}(z,Q^2) \equiv \delta(1-z) + \frac{\alpha_S}{2\pi}\, P_{qq}(z)\, \ln\left(\frac{Q^2}{\mu^2}\right) + \textit{higher orders}. \tag{1.55}$$

$P_{q\leftarrow q}(z,Q^2)$ describes the probability density of finding a quark inside the parent quark which carries away a fraction z of its momentum. For example in (1.50) a quark with a fraction ξ of the proton's momentum emitted a gluon reducing the quark's momentum fraction to x, so that $z = x/\xi$, see Fig. 1.6. We have already mentioned that P_{qq} can be calculated in perturbative QCD. To lowest order one finds [7]

$$P_{qq}(z) = \frac{4}{3}\,\frac{1+z^2}{1-z} \tag{1.56}$$

which is obviously singular for $z = 1$. This singularity is canceled if we include the virtual contributions to F_2/x shown in Figs. 1.4. P_{qq} is then modified to [7]

$$P_{qq}(z) = \frac{4}{3}\,\frac{1+z^2}{(1-z)_+} + 2\delta(1-z) \tag{1.57}$$

where we used the "+ prescription" defined by

$$\int_0^1 dz\, \frac{f(z)}{(1-z)_+} = \int_0^1 dz\, \frac{f(z)-f(1)}{1-z} \tag{1.58}$$

with $(1-z)_+ = 1-z$ for $z < 1$. We have now regularized final and initial state singularities in F_2/x. The remaining ultraviolet divergencies are swept into the running of the coupling α_S.

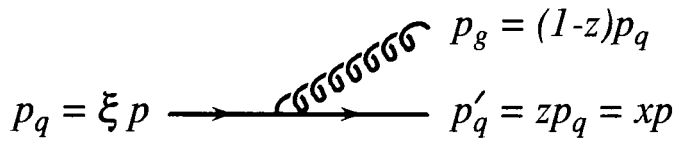

Figure 1.6: A quark of momentum $p_q = \xi p$ emits a gluon and remains with momentum $p'_q = xp$ where p is the momentum of the proton. Then the final quark carries a fraction $z = x/\xi$ of the parent quark's momentum.

DGLAP equations

We still have to add the contribution to F_2/x from the photon – gluon fusion process displayed in Fig. 1.4(f) which has the form [6]

$$\frac{F_2^{(\gamma^* g \to q\overline{q})}(x,Q^2)}{x} = \sum_q e_q^2 \int_x^1 \frac{d\xi}{\xi}\, g(\xi)\, \frac{\alpha_S}{2\pi}\, P_{qg}\left(\frac{x}{\xi}\right) \ln\left(\frac{Q^2}{\mu^2}\right) \tag{1.59}$$

where P_{qg} is defined in analogy to P_{qq}, that is $P_{qg}(z)$ is a measure for the probability that a gluon annihilates into a $q\overline{q}$ pair where the quark carries a fraction z of its momentum. Including this contribution in (1.54) leads to the complete DGLAP equation for the quark density [6]:

$$\frac{dq_f(x,Q^2)}{d\ln Q^2} = \frac{\alpha_S}{2\pi} \int_x^1 \frac{d\xi}{\xi} \left\{ q_f(\xi,Q^2)\, P_{qq}\left(\frac{x}{\xi}\right) + g(\xi,Q^2)\, P_{qg}\left(\frac{x}{\xi}\right) \right\} \tag{1.60}$$

for all quark flavours f separately. Similarly one can derive the DGLAP evolution equation for the gluon density which is given by [6]

$$\frac{dg(x,Q^2)}{d\ln Q^2} = \frac{\alpha_S}{2\pi} \int_x^1 \frac{d\xi}{\xi} \left\{ \sum_f q_f(\xi,Q^2)\, P_{gq}\left(\frac{x}{\xi}\right) + g(\xi,Q^2)\, P_{gg}\left(\frac{x}{\xi}\right) \right\}. \tag{1.61}$$

The structure functions P_{qg}, P_{gq} and P_{gg} have interpretations analogous to P_{qq} and can also be calculated in perturbative QCD. The leading order expressions are for example given in refs. [6, 7], and next-to-leading in refs. [17, 20].

So in summary we found that in perturbative QCD the evolution of the quark and gluon densities is described by the DGLAP equations (1.60) and (1.61). The starting distributions for the evolution at a low scale Q_0^2 have to be determined from experiment assuming an input form in x which obeys the sum rules and the limiting behaviour which

we discussed above. This procedure is followed in the so-called global analyses; for some recent sets see [21 – 23]. Alternatively one may generate the parton distributions dynamically starting from an input form for the valence quarks and a valence-like input for the sea quarks and gluons, as was done in [24].

This concludes the basic introduction into deep inelastic *ep* scattering. In the next chapter we will return to the DGLAP equations and discuss in which region in (x, Q^2) they are valid. Then we will investigate alternative evolution equations which are appropriate in different regions.

Chapter 2

Resumming leading logarithms — evolution equations

In this chapter we are concerned with large logarithms in the perturbative expansion which can occur when x is small or/and when Q^2 is large. These large logarithms need to be resummed to ensure convergence. In principle, all $\alpha_S^m \ln^n(1/x) \ln^p(Q^2/Q_0^2)$ should be summed, however as we will see in practice only the leading and sometimes the next-to-leading terms either in $\ln(1/x)$ or $\ln(Q^2/Q_0^2)$ or $\ln(1/x)\ln(Q^2/Q_0^2)$ in the perturbative expansion are included. The resummation leads to an evolution equation which describes how the gluon density evolves either with decreasing x or with increasing scale Q^2 (depending on which terms are summed). In the following we will give an overview over various evolution equations.

2.1 A second look at DGLAP evolution

In the previous chapter we explained that the DGLAP equations describe the evolution of the parton densities with Q^2 for given starting distributions at a lower scale Q_0^2. Our aim is now to show that the leading order DGLAP equations resum the leading terms in $\ln(Q^2/Q_0^2)$. (We again set $Q_0^2 = 1$ GeV^2.)

Let us for simplicity focus on the non-singlet distribution $q_{NS} \equiv q - \overline{q}$ and keep the

coupling α_S fixed. Imagine now that a quark of momentum ξp emits a gluon and remains with momentum xp, so that the final quark carries a fraction $z = x/\xi$ of the parent quarks momentum. Then we can rewrite the corresponding DGLAP equation in the following way [7]:

$$\begin{aligned}\frac{\partial q_{NS}(x,Q^2)}{\partial \ln Q^2} &= \frac{\alpha_S}{2\pi}\int_x^1 \frac{d\xi}{\xi} P_{qq}\left(\frac{x}{\xi}\right) q_{NS}(\xi,Q^2) \\ &= \frac{\alpha_S}{2\pi}\int_0^1 d\xi \int_0^1 dz\, \delta(x-\xi z)\, P(z)\, q_{NS}(\xi,Q^2). \end{aligned} \tag{2.1}$$

As a next step we take moments with the n-th moment being defined by

$$M_n(Q^2) \equiv \int_0^1 \frac{dx}{x} x^n\, q(x,Q^2). \tag{2.2}$$

Then we find that the evolution equation of the n-th moment is given by

$$\begin{aligned}\frac{\partial M_n(x,Q^2)}{\partial \ln Q^2} &= \frac{\alpha_S}{2\pi}\int_0^1 \frac{dz}{z} z^n P(z) \int_0^1 \frac{d\xi}{\xi} \xi^n q_{NS}(\xi,Q^2) \\ &\equiv \frac{\alpha_S}{2\pi} \qquad A_n \qquad M_n(Q^2). \end{aligned} \tag{2.3}$$

We see that taking moments has the advantage that the DGLAP equation factorizes into a term independent of Q^2 (the first integral, A_n) and a term containing all the Q^2 dependence (the second integral, $M_n(Q^2)$). Now we can simply solve this differential equation to obtain

$$M_n(Q^2) = C_n \exp\left[\gamma_n(\alpha_S)\, \ln Q^2\right] \tag{2.4}$$

where the anomalous dimension $\gamma_n(\alpha_S) \equiv \alpha_S A_n/2\pi$ and C_n is a coefficient. Rewriting this equation as a power series expansion we have

$$M_n(Q^2) = C_n \sum_r \frac{1}{r!} \left[\gamma_n(\alpha_S)\, \ln Q^2\right]^r. \tag{2.5}$$

It can be shown [18] that in an axial gauge where the gluon only has two polarisations (and therefore no unphysical polarisation) each term $C_n \frac{1}{r!}(\gamma_n \ln Q^2)^r$ corresponds to a *ladder diagram* with r rungs. An example of such a ladder diagram is given in Fig. 2.1(b). The ladder arises from the chain of emissions in Fig. 2.1(a) through application of the optical theorem. We assume here that the parent quark is emitted collinearly with the proton, so that is only carries longitudinal momentum (ξp). The $\ln Q^2$ dependence (including the

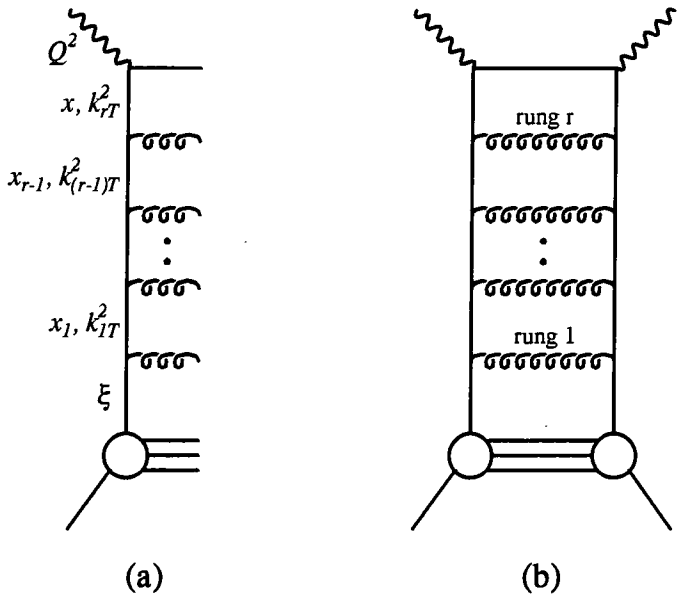

Figure 2.1: Diagrammatic representation of probing the proton at large x with a photon of large virtuality Q^2. Squaring the amplitude shown in (a) produces the ladder diagram in (b). The DGLAP equations sums the leading terms in $\ln Q^2$ which are generated by ladder diagrams of this form with the transverse momenta (k_{iT}) strongly ordered and the longitudinal momenta ($x_i p$) ordered.

factorial) of the term which a ladder diagram with r rungs generates is due to the r nested integrations over the r transverse momenta,

$$\int^{Q^2} \frac{dk_{rT}^2}{k_{rT}^2} \cdots \int^{dk_{3T}^2} \frac{dk_{2T}^2}{k_{2T}^2} \int^{dk_{2T}^2} \frac{dk_{1T}^2}{k_{1T}^2}, \tag{2.6}$$

in the region where they are strongly ordered, i.e.

$$Q^2 \gg k_{rT}^2 \gg \cdots \gg k_{2T}^2 \gg k_{1T}^2. \tag{2.7}$$

The r integrations

$$\int_x^1 \frac{dx_{r-1}}{x_{r-1}} \frac{\alpha_s}{2\pi} P\left(\frac{x}{x_{r-1}}\right) \cdots \int_{x_2}^1 \frac{dx_1}{x_1} \frac{\alpha_s}{2\pi} P\left(\frac{x_2}{x_1}\right) \int_{x_1}^1 \frac{d\xi}{\xi} \frac{\alpha_s}{2\pi} P\left(\frac{x_1}{\xi}\right) q_{NS}(\xi, Q^2) \tag{2.8}$$

yield the $C_n \gamma_n^r$ for ordered longitudinal momentum fractions

$$x < x_{r-1} < \cdots < x_2 < x_1 < \xi. \tag{2.9}$$

So in summary the DGLAP equation resums the $\alpha_S^r (\ln Q^2)^r$ contributions. It corresponds to the sum of ladder diagrams with up to r rungs where the transverse momenta

(squared) are strongly ordered and the longitudinal momentum fractions are ordered. It is valid when $\alpha_S \ln Q^2 \sim 1$, i.e. when Q^2 is large, and when x is large. At present the DGLAP equation is known up to next-to-leading order. The next-to-leading order terms in $\ln Q^2$ are obtained when the strong ordering (2.7) in the transverse momenta along the ladder is relaxed and two adjacent transverse momenta are approximately equal, i.e. when $k_{iT}^2 \simeq k_{(i+1)T}^2$. Then we lose a $\ln Q^2$.

2.2 The double leading logarithm approximation

As we go to smaller values of x the DGLAP equation loses its validity. The reason is that for small x large logarithms in $1/x$ can occur in the perturbative expansion which now have to be resummed. For large Q^2 this is achieved by the double leading logarithm approximation (DLLA) which resums the terms that contain the leading $\ln(1/x)$ and the leading $\ln Q^2$ simultaneously. The DLLA is therefore valid when $\alpha_S \ln(1/x) \ln Q^2 \sim 1$ but $\alpha_S \ln(1/x)$ and $\alpha_S \ln Q^2$ separately are small. Since we will not use the DLLA in the remainder of this thesis we will here just briefly discuss its form.

In the small x region the gluon is the dominant parton because the valence quark distributions have to vanish as $x \to 0$. It can then be shown [25] that in an axial gauge the double leading logarithms are generated by ladder diagrams with only gluon rungs, see Fig. 2.2. In the DLLA limit of the DGLAP equation the transverse momenta are still strongly ordered, i.e. they obey (2.7), but in addition the longitudinal momenta also fulfil strong ordering:

$$x \ll x_{r-1} \ll \cdots \ll x_2 \ll x_1 \ll \xi. \tag{2.10}$$

Let us see what this implies for the gluon distribution. For small x we can approximate the DGLAP equation (1.61) for the gluon density by

$$\frac{dg(x,Q^2)}{d\ln Q^2} = \frac{\alpha_S}{2\pi} \int_x^1 \frac{d\xi}{\xi} g(\xi, Q^2) P_{gg}\left(\frac{x}{\xi}\right). \tag{2.11}$$

For simplicity let us assume that the coupling α_S is fixed. A further simplication is

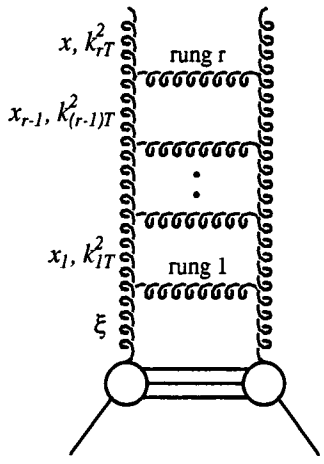

Figure 2.2: Ladder diagram with r gluon rungs. The double leading logarithms are generated by diagrams of this form where both the longitudinal ($x_i p$) and the transverse momenta (k_{iT}) are strongly ordered.

possible since as $x \to 0$ also $z = x/\xi \to 0$ which implies that the splitting function

$$P_{gg}(z) = 6\left[\frac{z}{(1-z)_+} + \frac{1-z}{z} + z(1-z)\right] + \left(\frac{11}{2} - \frac{N_f}{3}\right)\delta(1-z) \simeq \frac{6}{z} \tag{2.12}$$

where N_f is the number of quark flavours. Substituting this into (2.11) we find the gluon density to be

$$xg(x,Q^2) = \frac{3\alpha_S}{\pi}\int^{Q^2}\frac{dk_T^2}{k_T^2}\int_x^1\frac{d\xi}{\xi}\,\xi g(\xi) \tag{2.13}$$

when one gluon is emitted. Now for a diagram with r rungs as shown in Fig. 2.2 we have r nested transverse momentum integrations

$$\frac{3\alpha_S}{\pi}\int^{Q^2}\frac{dk_{rT}^2}{k_{rT}^2}\cdots\frac{3\alpha_S}{\pi}\int^{dk_{3T}^2}\frac{dk_{2T}^2}{k_{2T}^2}\,\frac{3\alpha_S}{\pi}\int^{dk_{2T}^2}\frac{dk_{1T}^2}{k_{1T}^2}, \tag{2.14}$$

which produce a contribution $\frac{1}{r!}(3\alpha_S/\pi)^r(\ln Q^2)^r$. The leading logarithms in $1/x$ come from the r integrations over the longitudinal momentum fractions

$$\int_x^1\frac{dx_{r-1}}{x_{r-1}}\cdots\int_{x_2}^1\frac{dx_1}{x_1}\int_{x_1}^1\frac{d\xi}{\xi}\,\xi g(\xi) \tag{2.15}$$

yielding $\frac{1}{r!}(\ln(1/x))^r G_0$ where we assumed that $\xi g(\xi,Q_0^2) \to G_0$ as $\xi \to 0$ with G_0 a constant. Therefore the gluon distribution can be written as the sum [7]

$$xg(x,Q^2) = G_0\sum_r\left(\frac{1}{r!}\right)^2\left(\frac{3\alpha_S}{\pi}\ln Q^2\ln\left(\frac{1}{x}\right)\right)^r. \tag{2.16}$$

Finally we utilize the modified Bessel function [25]

$$I_0 = \sum_r \frac{(\frac{1}{4}y^2)^r}{(r!)^2} \tag{2.17}$$

where for large y $I_0 \sim \exp(y)/\sqrt{2\pi y}$. We set $\frac{1}{4}y^2 = \frac{3\alpha_S}{\pi}\ln(1/x)\ln(Q^2)$ and find

$$xg(x,Q^2) \sim G_0 \exp\left\{2\left(\frac{3\alpha_S}{\pi}\ln\frac{1}{x}\ln Q^2\right)^{\frac{1}{2}}\right\}. \tag{2.18}$$

for the behaviour of the gluon distribution at small x in the DLLA. Recall that the DLLA is appropriate when $\alpha_S \ln(1/x)\ln Q^2 \sim 1$ but $\alpha_S \ln(1/x)$ and $\alpha_S \ln Q^2$ are small individually. The DLLA corresponds to the sum of gluon dominated ladder diagrams with both the transverse and the longitudinal momenta strongly ordered.

2.3 BFKL evolution

At the DESY *ep* collider HERA we are able to probe the proton in the small x region at *moderate* values of Q^2. Typically at HERA $x/Q^2 \gtrsim 10^{-5}$ GeV^{-2}, so for $Q^2 \sim 5$ GeV^2 we can reach values of x which are smaller than 10^{-4}. There $\alpha_S \ln(1/x)$ can be large which means that now the leading terms in $\ln(1/x)$ in the perturbative expansion need to be resummed. For very small x these contributions will be more important than the leading logarithms in Q^2 and we should therefore leave the Q^2 dependence unchanged rather than performing a resummation. We now relax the strong ordering (2.7) and integrate over the whole k_T phase space.

We can easily get an idea of how the resummation of the leading $\ln(1/x)$ terms affects the gluon density in the proton. In the DLLA we obtained the leading $\ln Q^2$ from the r nested integrations (2.14) over the transverse momenta of the gluons along the chain. The leading $\ln(1/x)$ arose from the integrations (2.15) over the longitudinal momentum fractions. If we now relax the strong ordering of the gluon transverse momenta we find the following behaviour of the gluon distribution:

$$\begin{aligned} xg(x,Q^2) &\sim \sum_r \left(\frac{1}{r!}\right)\left[\frac{3\alpha_S}{\pi}\, c\, \ln\left(\frac{1}{x}\right)\right]^r \\ &\sim \exp\left[\lambda\, \ln\left(\frac{1}{x}\right)\right] \\ &\sim x^{-\lambda} \end{aligned} \tag{2.19}$$

where c is a constant and $\lambda \equiv (3\alpha_S/\pi)c$. We will see in the following that the resummation of the leading $\ln(1/x)$ contributions indeed yields a behaviour of the gluon distribution of this form.

2.3.1 The leading order BFKL equation

The resummation of the leading $\ln(1/x)$ contributions can be performed in a more rigorous manner in QCD. Since we have to include the full Q^2 dependence it is necessary to work with the *unintegrated* gluon distribution $f(x,k_T^2)$ which is related to the conventional scale dependent gluon density in the following way:

$$xg(x,Q^2) = \int^{Q^2} \frac{dk_T^2}{k_T^2}\, f(x,k_T^2). \tag{2.20}$$

Balitskij, Fadin, Kuraev and Lipatov (BFKL) [26] found that summing the leading $\ln(1/x)$ contributions leads to an evolution equation for the unintegrated gluon distribution in terms of $\ln(1/x)$ of the form

$$\frac{\partial f(x,k_T^2)}{\partial \ln(1/x)} = \frac{3\alpha_S}{\pi}\, k_T^2 \int_0^\infty \frac{dk_T'^2}{k_T'^2} \left\{ \frac{f(x,k_T'^2) - f(x,k_T^2)}{|k_T'^2 - k_T^2|} + \frac{f(x,k_T^2)}{[4k_T'^4 + k_T^4]^{\frac{1}{2}}} \right\}, \tag{2.21}$$

the so-called *BFKL equation*. We may write the equation in the symbolic form

$$\begin{aligned} \frac{\partial f(x,k_T^2)}{\partial \ln(1/x)} &= \int dk_T'^2\, K(k_T,k_T')\, f(x,k_T'^2) \\ &= K \otimes f \end{aligned} \tag{2.22}$$

where K is the *BFKL kernel*. A full derivation of the BFKL equation is beyond the scope of this thesis. We will therefore instead give a simple explanation of its origin and outline which contributions are included in the BFKL kernel. After demonstrating how the equation can be solved analytically we will discuss its main properties.

Figure 2.3: Diagrammatic representation of gluon exchange in the t-channel.

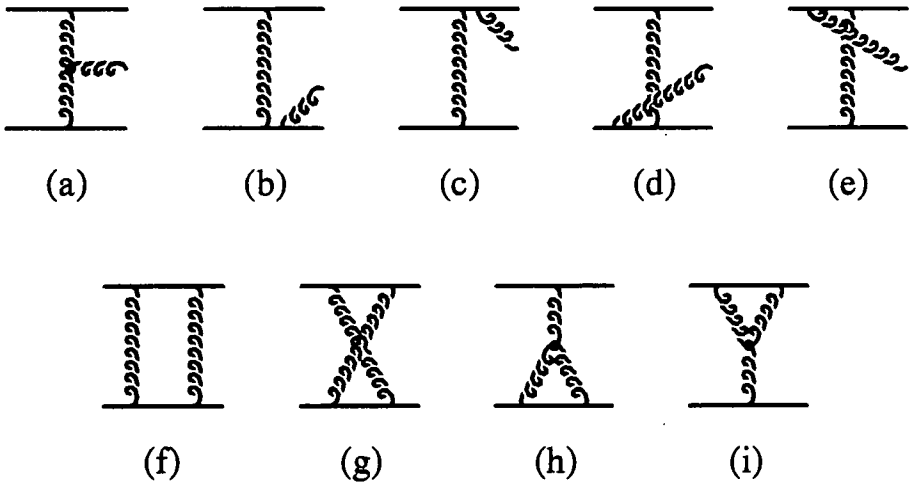

Figure 2.4: The diagrams corresponding to (a) – (e) the emission of real and (f) – (i) virtual gluons.

The BFKL kernel

To see how the structure of the BFKL kernel arises and which contributions it includes it is easiest to consider the scattering of two quarks with the exchange of a gluon in the t-channel ($qq \to qq$). This process is shown diagrammatically in Fig. 2.3. The exchanged gluon is in a colour octet state (although the BFKL equation actually describes the exchange of a colour singlet, see below). The diagram in Fig. 2.3 only gives the leading order contribution and we therefore have to include higher order QCD corrections. The diagrams corresponding to real gluon emissions are displayed in Figs. 2.4(a) – (e). It can be shown that the sum of these diagrams can be represented by the effective diagram shown in Fig. 2.5. The square of the corresponding BFKL vertex factor is given by

$$\Gamma^2(k_T, k'_T) = \overline{\alpha}_S \frac{k_T^2 k_T'^2}{q_T^2} \tag{2.23}$$

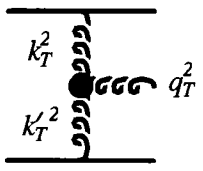

Figure 2.5: The BFKL vertex Γ which corresponds to the sum of the real gluon emissions shown in Figs. 2.4(a) – (e).

(see for example [7]) where we introduced

$$\overline{\alpha}_S \equiv \frac{3\alpha_S}{\pi}. \tag{2.24}$$

Although the contributions depicted in Figs. 2.4(a) – (e) are gauge dependent when considered individually, it can be proven that the resulting effective vertex is gauge independent [13]. The virtual gluon emissions, which due to interference with the t-channel diagram in Fig. 2.3 produce corrections at the same order as the above real emissions, are depicted in Figs. 2.4 (f) – (i). The effect of these virtual corrections is to "reggeize" the gluon exchange [26, 27] in Fig. 2.3 which means that the behaviour of a t-channel gluon with transverse momentum k_T is changed from

$$\frac{s}{k_T^2} \to \left(\frac{s}{k_T^2}\right)^{\alpha_g(k_T^2)}. \tag{2.25}$$

Here α_g is the gluon Regge trajectory and s is the centre-of-mass energy squared of the external particles, i.e. the incoming quarks in this case.

In the calculation of the contributions in Fig. 2.4 to leading logarithmic accuracy the so-called eikonal approximation [13] was used which allowed a simplification of the expressions for the amplitudes. Since this approximation is not only valid for spin-$\frac{1}{2}$ quarks but for particles of any spin we can replace the quark lines in Fig. 2.4 by gluons. We then have the diagram depicted in Fig. 2.6(a) instead of Fig. 2.5. It can be shown [27] that in the regime where the longitudinal momenta of the exchange gluons are strongly ordered adding more and more gluons results in additional factors of effective vertices Γ. Therefore the colour octet amplitude for two quarks scattering into two quark and r gluons in the leading $\ln(1/x)$ approximation may be constructed as a generalisation of the amplitude for $qq \to qq$, as is represented diagrammatically in Fig. 2.6(b). Again the inclusion of

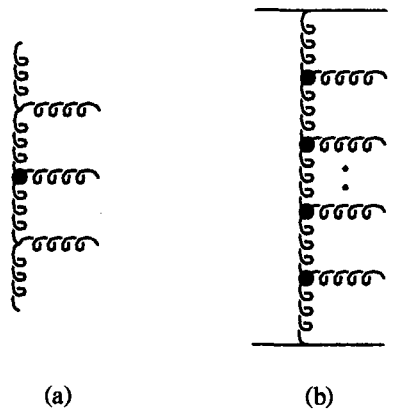

Figure 2.6: (a) The effective vertex as shown in Fig. 2.5 but with the external quark lines replaced by gluons. (b) The colour octet amplitude for $qq \to qq + r$ gluons in the leading $\ln(1/x)$ approximation built up from effective vertices and reggeized gluons in the t-channel.

the virtual correction leads to a reggeisation of the t-channel gluons. Furthermore it can be shown [13] that the emission of quark-antiquark pairs in the chain is suppressed with respect to gluon emission and is therefore neglected in the leading $\ln(1/x)$ approximation.

So far we considered the exchange of a gluon in a colour octet state. The BFKL equation however describes the exchange of a colourless object which is often referred to as the QCD or *BFKL pomeron*. Therefore the (squared) amplitude for this colour singlet exchange can be derived in analogy to the calculation of the colour octet amplitude which we explained above but replacing the octet colour factors by the singlet ones. The BFKL kernel includes the contributions from real gluon emission as well as the virtual corrections. In the BFKL equation (2.21) the real gluon contributions correspond to terms proportional to $f(x, k_T'^2)$ whereas the virtual corrections lead to terms proportional to $f(x, k_T^2)$. The apparent singularity in (2.21) at $k_T'^2 = k_T^2$ cancels in the sum of the real and virtual gluon contributions [28].

Ladder structure of the BFKL equation

Like the DLLA the BFKL equation corresponds to a sum of ladder diagrams with gluon rungs only, see Fig. 2.7. However these BFKL ladders are only *effective* ladder diagrams

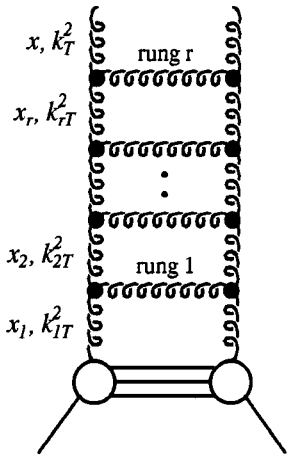

Figure 2.7: The effective gluon ladder diagram for the unintegrated gluon density $f(x, k_T^2)$ in the leading $\ln(1/x)$ approximation.

with BFKL vertices. They contain all the real and virtual gluon contributions discussed above. As for the DLLA the longitudinal momentum fractions along the ladder are strongly ordered, i.e.

$$x_1 \gg x_2 \gg \cdots \gg x_r \gg x, \tag{2.26}$$

which leads to the leading $\ln(1/x)$ terms. The transverse momenta, on the other hand, are now unordered. The BFKL equation (2.21) arises from a recursion relation which allows us to calculate the unintegrated gluon density $f_r(x, k_T^2)$ corresponding to a gluon ladder with r rungs from the gluon density $f_{r-1}(x, k_T^2)$ which can be represented by an $r-1$ rung ladder diagram. This recursion relation has the form [7]

$$f_r(x, k_T^2) \;=\; \int_x^1 \frac{dx_r}{x_r} \int dk_{rT}^2 \; K(k_T, k_{rT})\, f_{r-1}(x_r, k_{rT}^2) \tag{2.27}$$

which we symbolically write as

$$f_r \equiv A \otimes f_{r-1}. \tag{2.28}$$

Since f corresponds to the sum of ladder diagrams,

$$f = \sum_{r=0}^{\infty} f_r, \tag{2.29}$$

we then find

$$f - f_0 = \sum_{r=1}^{\infty} f_r = \sum_{r=1}^{\infty} (A \otimes f_{r-1}) = A \otimes \sum_{r=0}^{\infty} f_r = A \otimes f. \tag{2.30}$$

This yields the BFKL equation in integral form:

$$f(x,k_T^2) \;=\; f_0(x,k_T^2) \;+\; \int_x^1 \frac{dx'}{x'} \int dk_T'^2\, K(k_T,k_T')\, f(x',k_T'^2) \tag{2.31}$$

where f_0 is the so-called driving term which is related to f via the boundary condition that at the starting point x_0 of the evolution

$$f(x=x_0,k_T^2) \;=\; f_0(x_0,k_T^2). \tag{2.32}$$

From the recursion relation (2.27) we also see that the BFKL equation can be expressed in the differential form

$$-\,x\frac{\partial f}{\partial x} \;=\; \int dk_T'^2\, K(k_T,k_T')\, f(x,k_T'^2) \tag{2.33}$$

which is equivalent to (2.21).

So in summary the BFKL equation describes the sum of ladder diagrams with reggeized gluons in the t-channel and conventional gluons as rungs. The vertices are the effective BFKL vertices Γ (see (2.23)) containing the various contributions shown in Fig. 2.5. As already mentioned the exchanged colourless object is generally called the BFKL pomeron.

A cross check

Above we explained that the DLLA corresponds to the sum of gluon ladder diagrams where the transverse momenta of the gluons are strongly ordered. For the BFKL equation we relaxed this strong ordering. So if we introduce strong ordering of the transverse momenta in the BFKL equation we should obtain the DLLA. We can easily see that this is the case since strong ordering implies that $k_T^2 \gg k_T'^2$ and therefore the BFKL kernel

$$K^{\textit{strong ordering}}(k_T,k_T') = \overline{\alpha}_S\,\frac{1}{k_T'^2}\,\Theta(k_T^2-k_T'^2). \tag{2.34}$$

Substituting this expression for the kernel into the recursion relation (2.27) we obtain

$$\begin{aligned} f_r(x,k_T^2) \;&=\; \overline{\alpha}_S \int_x^1 \frac{dx_r}{x_r} \int^{k_T^2} \frac{dk_{rT}^2}{k_{rT}^2}\, f_{r-1}(x_r,k_{rT}^2) \\ &\simeq\; \overline{\alpha}_S\,\frac{1}{r}\,\ln\!\left(\frac{1}{x}\right)\,\frac{1}{r}\,\ln\!\left(\frac{k_T^2}{\mu^2}\right) f_{r-1}(x,k_T^2). \end{aligned} \tag{2.35}$$

Therefore the unintegrated gluon distribution

$$f(x,k_T^2) \;=\; \sum_r f_r(x,k_T^2) \;\simeq\; \sum_r \left(\frac{1}{r!}\right)^2 \left[\overline{\alpha}_S \ln\!\left(\frac{1}{x}\right) \ln\!\left(\frac{k_T^2}{\mu^2}\right)\right]^r \tag{2.36}$$

which on utilizing the modified Bessel function (2.17) yields

$$f(x,k_T^2) \;\sim\; \exp\!\left\{2\left[\overline{\alpha}_S \ln\!\left(\frac{1}{x}\right) \ln\!\left(\frac{k_T^2}{\mu^2}\right)\right]^{\frac{1}{2}}\right\}. \tag{2.37}$$

Finally applying the relation (2.20) between the conventional and the unintegrated gluon density we reproduce the DLLA (2.18) as anticipated.

2.3.2 Analytic solution of the leading order BFKL equation

The leading order BFKL equation (2.21) is written for fixed coupling constant α_S. We will see later that one may introduce by hand the running of the coupling to include some of the next-to-leading order corrections. The BFKL equation then has to be solved numerically. The original equation with fixed coupling can, however, be solved analytically as we demonstrate in Appendix A. Here we only summarize the main steps and results so that we are able to discuss the properties of the solution of the BFKL equation in the following subsection.

When we analyzed the structure of the DGLAP equation in Section 2.1 we took the moments which caused the DGLAP equation to factorize. We were then able to solve the equation. Here we proceed in a similar way: we calculate the Mellin transform of f which has the form

$$\tilde{f}(x,\omega) \;\equiv\; \int_0^\infty dk_T^2\, (k_T^2)^{-\omega-1}\, f(x,k_T^2). \tag{2.38}$$

As a consequence of this the BFKL equation (2.21) factorizes and we have

$$\frac{\partial \tilde{f}(x,\omega)}{\partial \ln(1/x)} \;=\; \tilde{K}(\omega)\, \tilde{f}(x,\omega), \tag{2.39}$$

where $\tilde{K}$ is the Mellin transform of the BFKL kernel K. In Appendix B we obtain

$$\tilde{K}(\omega) \;=\; \overline{\alpha}_S\, [2\Psi(1) - \Psi(\omega) - \Psi(1-\omega)]. \tag{2.40}$$

where Ψ is defined in terms of the Γ function, $\Psi(z) \equiv \Gamma'(z)/\Gamma(z)$. The Mellin transformed BFKL equation (2.39) can easily be solved with the result

$$\tilde{f}(x,\omega) \;=\; \tilde{f}(x_0,\omega)\,\left(\frac{x}{x_0}\right)^{-\tilde{K}(\omega)} \tag{2.41}$$

where $\tilde{f}(x_0,\omega)$ is the Mellin transform of the input distribution $f_0(x,k_T^2)$. The solution of the BFKL equation (2.21) is obtained by performing the inverse Mellin transform

$$f(x,k_T^2) \;=\; \frac{1}{2\pi i}\int_{c-i\infty}^{c+i\infty} d\omega\,(k_T^2)^{\omega}\,\tilde{f}(x,\omega) \tag{2.42}$$

which yields

$$f(x,k_T^2) \;=\; \left(\frac{x}{x_0}\right)^{-\lambda}\,\frac{\tilde{f}(x_0,\frac{1}{2})\,\sqrt{k_T^2}}{\left[2\pi\left(\lambda''\ln\left(\frac{x_0}{x}\right)+A\right)\right]^{\frac{1}{2}}}\,\exp\left[\frac{-\ln^2\left(\frac{k_T^2}{\bar{k}_T^2}\right)}{2\lambda''\ln\left(\frac{x}{x_0}\right)+2A}\right] \tag{2.43}$$

where for simplicity we defined

$$\ln\bar{k}_T^2 \;\equiv\; -\frac{1}{\tilde{f}}\frac{d\tilde{f}}{d\omega}, \qquad A \;\equiv\; \frac{1}{\tilde{f}}\frac{d^2\tilde{f}}{d\omega^2}. \tag{2.44}$$

The exponent λ is the maximum eigenvalue of the Mellin transformed BFKL kernel $\tilde{K}$ which determines the x behaviour of the BFKL solution f. It is given by

$$\lambda \;=\; \frac{3\alpha_S}{\pi}\,4\ln 2 \tag{2.45}$$

and its second derivative

$$\lambda'' \;=\; \frac{3\alpha_S}{\pi}\,28\zeta(3) \tag{2.46}$$

where $\zeta(3) = 1.202$. We will discuss the main features of f and the importance of the magnitude of λ in the following subsection.

2.3.3 Properties of the leading order BFKL equation

Having obtained the solution (2.43) of the leading order BFKL equation we will now investigate its properties. We start by considering the x dependence of f.

$x^{-\lambda}$ behaviour

From (2.43) we see that the solution f behaves as $x^{-\lambda}$ modulated by the logarithmic factor $\sqrt{\lambda'' \ln(x_0/x) + A}$. Here λ is the maximum eigenvalue of the (Mellin transform of the) BFKL kernel as given in (2.45) and λ'' its second derivative, see (2.46). Since $\lambda \sim 0.5$, the solution of the BFKL equation shows a steep rise with decreasing x. In fact, it is this steep increase as $x \to 0$ which is generally used to identify BFKL dynamics and we will follow this approach later in this thesis when we are searching for BFKL signatures at HERA. Due to the factorisation theorem which allows us to calculate observables like for example the structure function F_2 as the convolution of the unintegrated gluon density f and a so-called impact factor the $x^{-\lambda}$ behaviour feeds through into measureable quantities.

Intercept of the BFKL pomeron trajectory

The largeness of λ also has the following consequences. Above we mentioned that the colourless BFKL ladder is often referred to as the BFKL pomeron. The BFKL pomeron appears in hard QCD interactions and its Regge trajectory has the intercept $\alpha_{I\!P}(0) = 1 + \lambda \simeq 1.5$. Firstly, this is much larger than the intercept of the so-called soft pomeron trajectory, $\alpha_{I\!P}^{soft}(0) = 1.08$, which was obtained by Donnachie and Landshoff [29] through fits to hadronic and photoproduction ($Q^2 \simeq 0$) total cross section data and extraction of the dependence on the centre-of-mass energy. Secondly, from (1.33) we see that the magnitude of the BFKL pomeron intercept leads to a behaviour of the total cross section

$$\sigma_{tot} \sim s^{\overline{\alpha}_S 4 \ln 2} \sim s^{\frac{1}{2}} \tag{2.47}$$

at high energies. So σ_{tot} grows with energy which means it will violate the Froissart bound which tells us that cross sections cannot increase faster than $\ln^2 s$ with increasing s (see

for example [13]). We will return to this problem in Section 2.4.

$(k_T^2)^{\frac{1}{2}}$ behaviour and diffusion in $\ln k_T^2$

From (2.43) we can also extract the k_T^2 dependence of the unintegrated gluon distribution as predicted by leading order BFKL dynamics. We see that for increasing k_T^2 f rises with $\sqrt{k_T^2}$ multiplied by an exponential function.

Let us investigate the remaining k_T^2 dependence more closely. It is helpful to recall the general form of a Gaussian distribution $\mathcal{G}(\xi)$ in terms of some variable ξ. We have

$$\mathcal{G}(\xi) = \frac{1}{\sqrt{2\pi}\sigma} \exp\left[-\frac{1}{2}\frac{(\xi - a)^2}{\sigma^2}\right] \tag{2.48}$$

where a is the maximum of the distribution and σ determines its width. A comparison with (2.43) then shows that $f(x, k_T^2)/\sqrt{k_T^2}$ has the shape of a Gaussian in $\ln k_T^2$ with maximum at $\ln \overline{k}_T^2$ and a width given by $\sqrt{\lambda'' \ln(x_0/x) + A}$. Therefore the BFKL evolution of an unintegrated gluon density $f(x, k_T^2)$ from $x = x_0$ to smaller values of x is accompanied by a diffusion in $\ln k_T^2$. The initial width of the Gaussian at x_0 is determined by $f(x_0, k_T^2)$ (which is not necessarily a perfect Gaussian), the longer the evolution the more the distribution broadens. This is for example shown schematically in Fig. 1 of ref. [30]. The diffusion in $\ln k_T^2$ is a consequence of the relaxation of the strong ordering of the transverse momenta which leads to a random walk in k_T^2. It has the side-effect that it may cause a penetration of the infrared region invalidating the perturbative treatment. We will discuss this problem in Section 3.1 and explain how it can be avoided.

To summarize, BFKL dynamics predict an $x^{-\lambda}$ behaviour of the unintegrated gluon density f as we already anticipated in the introduction to Section 2.3. f rises with $\sqrt{k_T^2}$ as k_T^2 increases. The $\sqrt{k_T^2}$ growth is modulated by a Gaussian diffusion factor with leads to a broadening of the distribution which accompanies the BFKL evolution of f to smaller values of x. These are the signatures we will be searching for when trying to identify BFKL dynamics in deep inelastic ep scattering in the small x region at HERA in the following chapters.

2.3.4 Next-to-leading order corrections to the BFKL equation

Above we discussed the BFKL equation in leading order which resums the leading logarithms in $\ln(1/x)$. In the remainder of this thesis we will show predictions for observables which are based on this leading order equation. However, since meanwhile next-to-leading corrections have been calculated we will now briefly explain why the next-to-leading order contributions are important, which corrections have to be computed and how they affect the leading eigenvalue λ of the BFKL kernel. Then we will outline how we can proceed as long as the next-to-leading corrections are not available in a form which is straightforward to utilize in phenomenological applications.

The need for the next-to-leading order corrections

There are four main reasons for why it is necessary to know the next-to-leading order corrections to the BFKL equation (2.21). Firstly, as we pointed out, the leading order equation was written for fixed QCD coupling constant. Since the transverse momenta of the gluons along the BFKL ladder may be of the same order one might think that it is appropriate to freeze the coupling at a typical transverse momentum of these gluons. However, due to the diffusion in $\ln k_T^2$ a broader range of transverse momenta can occur along the ladder which implies that the coupling should really be evaluated at the true transverse momenta of the t-channel gluons. Secondly, the leading order BFKL equation does not include energy and longitudinal momentum conservation. Although the terms which violate energy-momentum conservation are formally subleading they can nevertheless be of importance when making BFKL based predictions. Thirdly, in the leading order BFKL formalism jets are only determined in leading order and therefore have no non-trivial substructure [31]. Finally, because the next-to-leading order corrections suppress the strong rise of the unintegrated gluon distributions towards small x there is hope that they allow for a smoother transition between the medium Q^2 behaviour as predicted by BFKL dynamics and the low Q^2 physics and also between the small and large x behaviour.

Calculation of the next-to-leading order corrections

Next-to-leading order corrections to the BFKL equation can be obtained in two different ways [3]. The first approach is motivated by the violation of unitarity of the total cross section (2.47) due to the magnitude of the maximum eigenvalue of the leading order BFKL kernel $\lambda_{LO} \equiv \lambda = \overline{\alpha}_S 4 \ln 2$ which we discussed in Section 2.3.3. Its aim is to restore unitarity in the BFKL formalism. This approach was followed by Bartels, Lipatov and Wüsthoff and by Gribov, Levin and Ryskin whose work we will discuss in Section 2.4. It results in a subset of next-to-leading order correction.

The second procedure is to calculate *all* next-to-leading logarithmic (NLL) corrections. It firstly requires the computation of the real NLL corrections induced by the relaxation of the strong ordering (2.26) of the longitudinal momentum fractions of the gluons along the BFKL ladder. Secondly, the virtual NLL contributions have to be obtained. The real corrections include the vertices corresponding to the emission of two particles with comparable longitudinal momentum fractions, i.e. $g^*g \to gg$ or $q\overline{q}$, $g^*q \to gq$, and $g^*g^* \to gg$ or $q\overline{q}$, and in addition the one-loop corrections to the BFKL vertex. The virtual contributions correspond to the NLL corrections to the gluon reggeisation which arise from the NLL corrections to the Pomeron trajectory. The NLL corrections have been computed by Fadin, Lipatov and collaborators, Camici and Ciafaloni, and Del Duca. However, at present they are not available in a form which can easily be implemented in phenomenological analyses. Nevertheless, it is already evident that the next-to-leading order corrections have a large effect. As was found by Ciafaloni and Camici [33] the maximum eigenvalue of the BFKL kernel in next-to-leading (NLO) order is (for three colours) given by

$$\lambda_{NLO} \simeq \lambda_{LO} \left(1 - 3.4 \frac{3\alpha_S}{\pi} - 0.15 \frac{N_f \alpha_S}{\pi}\right) \tag{2.49}$$

where $\lambda_{LO} = \overline{\alpha}_S 4 \ln 2$. We see that the inclusion of the NLL corrections leads to a large negative shift of the BFKL eigenvalue. Since it is λ which determines the small x behaviour this suggests that the NLL contributions should be included in phenomenological applications of the BFKL equation. Note also that λ_{NLO} depends on N_f, the number of

[3] Reviews of the next-to-leading logarithmic corrections to the BFKL equation can for example be found in [13, 31, 32].

flavours, whereas the leading order result was flavour independent.

Inclusion of some next-to-leading corrections in the calculation

As long as the next-to-leading order corrections to the BFKL equation are not available in a form which can easily be implemented in Monte Carlo computations we may proceed in the following way. We allow the coupling α_S to run in the leading order BFKL equation which amounts to including some of the next-to-leading order contributions. The BFKL equation (2.21) then becomes

$$\frac{\partial f(x,k_T^2)}{\partial \ln(1/x)} = \frac{3\alpha_S(k_T^2)}{\pi} k_T^2 \int_{k_0}^{\infty} \frac{dk_T'^2}{k_T'^2} \left\{ \frac{f(x,k_T'^2) - f(x,k_T^2)}{|k_T'^2 - k_T^2|} + \frac{f(x,k_T^2)}{[4k_T'^4 + k_T^4]^{\frac{1}{2}}} \right\}. \quad (2.50)$$

Here we introduced a lower cutoff k_0^2 on the transverse momentum integration which prevents the diffusion into the infrared region where the coupling constant is large. Imposing the cutoff has the effect of discretizing the eigenvalue spectrum of the (Mellin transform of the) BFKL kernel $\tilde{K}(\omega)$. The maximum eigenvalue becomes dependent on k_0^2 and its magnitude decreases with increasing k_0^2 [30]. Therefore the strong $x^{-\lambda}$ growth as $x \to 0$ is somewhat suppressed. The BFKL equation including running coupling has to be solved numerically introducing also an upper cutoff on the transverse momentum integration. In the calculation of the BFKL based predictions shown in the following chapters we indeed proceeded in this way (see also Section 3.2.3).

Solving the BFKL equation numerically has the additional advantage that it is then possible to require energy-momentum conservation "by hand" in the Monte Carlo program. The role of energy conservation in the BFKL equation was studied in [34]. There it was demanded that for a t-channel gluon in the BFKL ladder carrying four momentum k and a virtual photon probe with four momentum q the centre-of-mass energy for the corresponding subprocess $\hat{s} = (k+q)^2 \geq 0$ which resulted in an upper limit on the square of the transverse momentum k_T^2 of the gluon. The main effect of this constraint is a suppression of the BFKL prediction for the gluon density in the small x region. Here we will restrict ourselves to requiring that the final state partons which fragment into hadrons that are measured in the experiment obey energy momentum conservation.

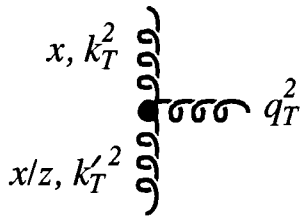

Figure 2.8: Fragment of (the left half of) a BFKL ladder diagram. x and x/z are the fractions of the proton's longitudinal momentum carried by the gluons. The transverse momenta of the gluons along the ladder and of the emitted gluon are denoted by k_T, k'_T and q_T, respectively.

Higher order corrections can also be included by noting that the virtualities of the exchanged gluons along the BFKL ladder should arise dominantly from the transverse components of their momenta rather than from the longitudinal ones, otherwise we lose a $\ln(1/x)$. So for a gluon of transverse momentum k'_T as shown in Fig. 2.8 we have $|k'|^2 \simeq k_T'^2$. This leads to the so-called kinematic constraint [35]

$$k_T^2 > z q_T^2 \tag{2.51}$$

where the variables are defined in Fig. 2.8. The introduction of this kinematic constaint in the leading order BFKL equation preserves its scale invariance if the coupling α_S is kept fixed. In this case the equation can be solved analytically and the exponent λ calculated to all orders, as was done in ref. [36]. There it was found that the imposition of the kinematic constraint causes a considerable suppression of the maximum eigenvalue λ. In fact, it turned out that it is not sufficient to only include next-to-leading order corrections to λ but that higher order effects are of importance, see Fig. 2 in ref. [36]. In the calculations presented in this thesis we did not utilize the kinematic constraint.

At the time when the results shown in the following chapters were obtained the full next-to-leading order corrections to the BFKL equation were not available. Therefore all calculations were based on leading order BFKL dynamics where the BFKL equation was solved numerically allowing the coupling to run.

Recall that the BFKL formalism is appropriate in the small x region for moderate values of Q^2. The leading order BFKL equation resums the leading logarithms in $\ln(1/x)$ and corresponds to the infinite sum of gluon ladder diagrams where the longitudinal

momenta of the gluons are strongly ordered and the transverse momenta are comparable in size. The ladder diagrams consist of reggeized gluons in the t channel and conventional gluons as rungs which are connected by effective BFKL vertices. Leading order BFKL dynamics predict a characteristic $x^{-\lambda}$ behaviour of the unintegrated gluon distribution. For increasing k_T^2 f rises with $\sqrt{k_T^2}$ modulo a Gaussian diffusion factor which causes a broadening of the distribution that accompanies the BFKL evolution of f to smaller values of x. As we will see in the remaining chapters these signatures can be used to identify BFKL dynamics at colliders.

2.4 Parton screening and the GLR equation

Of course, the $x^{-\lambda}$ growth of the gluon distribution with decreasing x cannot go on indefinitely, otherwise unitary would be violated. Eventually the density of the gluons inside the proton becomes so large that they cannot be treated as free partons any longer. They begin to interact and screen each other which causes *shadowing* effects [4]. As a consequence of the shadowing the gluon distribution does not rise forever but rather reaches a saturation limit given by [27]

$$x g_{sat}(x, Q^2) = \frac{C}{\alpha_S(Q^2)} R_P^2 Q^2 \tag{2.52}$$

where C is a constant and R_P is the radius of the proton which is probed at scale Q^2. Here is was assumed that the gluons are spread uniformly inside the proton. On the other hand it has been proposed [38, 39] that the gluons may be concentrated in small areas inside the proton, so-called hot-spots. The saturation limit is then described by (2.52) but with R_P replaced by the radius R_{hs} of the hot-spot.

Gribov, Levin and Ryskin (GLR) obtained the correction to the BFKL equation (2.21) due to shadowing effects by considering recombination diagrams as the one shown in Fig. 2.9. The box in the diagram represents all possible QCD diagrams which couple four gluons to two. The two ladders in the lower half of the diagram couple to the proton. The effect of such recombination diagrams is to introduce an additional non-linear term

[4] An introduction to shadowing effects can for example be found in ref. [37].

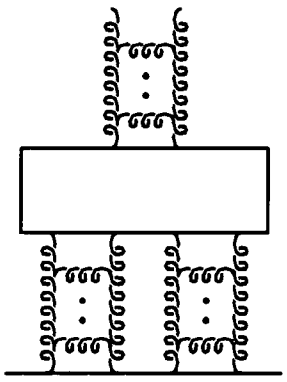

Figure 2.9: The basic gluon recombination diagram which contributes to the GLR equation. The box represents all possible couplings of two gluon ladders to one.

into the BFKL equation which then becomes [27]

$$\frac{\partial f(x,k_T^2)}{\partial \ln(1/x)} = K \otimes f - \frac{81\alpha_S^2(k_T^2)}{16R^2k_T^2}[xg(x,k_T^2)]^2. \tag{2.53}$$

This evolution equation is generally called the *GLR equation.* Here R is a radius determined by the way in which the gluon ladders couple to the proton; depending on the model $R = R_P$ or R_{hs}. The GLR equation is based on some assumptions concerning the form of the three-ladder vertex and the coupling of n ladders to the proton. In the derivation it was also presumed that there are no correlations between two recombining gluon ladders. This is actually not quite true and therefore the GLR equation as it stands may not be valid [5]. In this thesis we will rely on the results of the numerical studies presented in [41]. There it was found that in the (x, Q^2) region accessible at HERA shadowing effects are small unless the gluons inside the proton are concentrated in hot-spots. We will therefore neglect shadowing in the remaining chapters.

2.5 Summary

In this chapter we explained the need for the resummation of large logarithms which can occur in the perturbative expansion. We started by discussing the DGLAP equation which resums the $\alpha_S^r \ln(Q^2)^r$ contributions and is valid when Q^2 is large and x is not

[5] An overview of this problem is given in ref. [40].

small. It corresponds to the sum of ladder diagrams with up to r rungs where the transverse momenta are strongly ordered and the longitudinal momenta are ordered. Next we considered the case where $\alpha_S \ln(1/x)$ and $\alpha_S \ln(Q^2/Q_0^2)$ are both small individually but $\alpha_S \ln(1/x) \ln(Q^2/Q_0^2)$ is large. Then the double leading logarithm approximation should be used which resums the leading terms in $\ln(1/x) \ln(Q^2/Q_0^2)$ and corresponds to the sum of gluon ladder diagrams with strongly ordered transverse and longitudinal momenta. In Section 2.3 we studied the BFKL equation which is appropriate in the small x region for moderate values of Q^2. We saw that it resums the leading terms in $\ln(1/x)$ and that it corresponds to the infinite sum of BFKL ladder diagrams with reggeized gluons in the t-channel which are joint to conventional gluons as rungs by effective vertices. Finally we briefly discussed the recombination effects which are incorporated in the GLR equation.

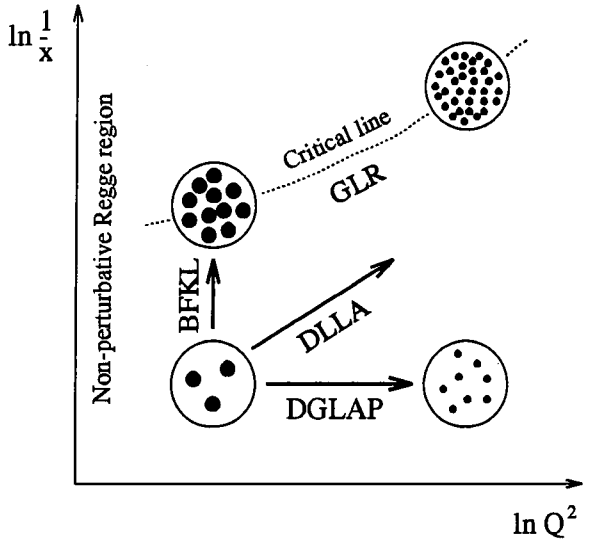

Figure 2.10: The regions of validity [40] in the (x, Q^2) plane of the various evolution equations. The gluon content of the proton as seen by the virtual photon probe is symbolized by dots. The dotted line represents the critical line below which perturbative QCD is applicable.

The regions of validity of the BFKL, the DGLAP and the GLR equation and of the DLLA are depicted in Fig. 2.10 where we also indicated the critical line below which perturbative QCD is applicable. The following chapters are devoted to investigating if the BFKL or the DGLAP equation is appropriate in the HERA small x region.

Chapter 3

Deep inelastic events containing an identified forward jet

In this chapter we motivate the study of the deep inelastic final state and in particular the deep inelastic + forward jet process. We introduce the QCD formalism for the calculation of the cross section for this reaction and discuss which cuts have to be imposed. This in turn will enable us to obtain the cross sections for the DIS + forward γ and the DIS + forward π^0 processes which are the main topics presented in Chapters 4 and 5, respectively. Then, in Chapter 6, we will return to the DIS + jet process. There we will calculate the cross section imposing the cuts which were used by the H1 collaboration in the measurement and normalize to their data. With this normalisation we are able to make predictions to compare with the very recent data on DIS + π^0 and single particle transverse momentum spectra in Chapters 7 and 8.

3.1 The DIS + forward jet measurement – Mueller's proposal

The behaviour of the proton structure function $F_2(x, Q^2)$ at small x reflects the behaviour of the gluon distribution, since the gluon is by far the dominant parton in this regime. Perturbative QCD does not predict the absolute value of the parton distributions, but rather determines how they evolve as a function of the kinematic variables from a given

input. As explained in the previous chapter the evolution of an input gluon distribution can be described in two different limits [6] of QCD leading to the following two evolution equations:

- A *Dokshitzer-Gribov-Lipatov-Altarelli-Parisi (DGLAP) equation* [18, 19] which resums the $\alpha_S^n \ln^n(Q^2/Q_0^2)$ contributions and is valid as long as x is not too small. These leading $\ln Q^2$ contributions come from the configurations in which the transverse momenta k_T of the gluons along the chain are strongly ordered (see Fig. 2.1).
- The *Balitskij-Fadin-Kuraev-Lipatov (BFKL) equation* [26] which should be appropriate as we go to small x since it resums the leading order $\alpha_S^n \ln^n(1/x)$ terms. Here the longitudinal momenta of the gluons along the ladder are strongly ordered (see Fig. 2.7).

The solution of the BFKL equation leads to a singular $x^{-\lambda}$ small x behaviour of the unitegrated gluon distribution, where $\lambda = (3\alpha_S/\pi)4\ln 2$ for fixed α_S and $\lambda \simeq 0.5$ if a reasonable prescription for the running of α_S and for the treatment of the infrared region is assumed [30, 41]. The $x^{-\lambda}$ behaviour of the BFKL gluon feeds through, via the k_T-factorisation theorem [42], into the small x behaviour of the structure function F_2. Therefore it should in principle be possible to identify BFKL resummation effects via a measurement of F_2 at HERA. It turns out, however, that although the data do show a steep rise with decreasing x a distinction between the two limits of evolution is not feasible. In fact, the rise in the latest precise H1 and ZEUS measurements [16] can be well described by next-to-leading order DGLAP evolution down to $Q^2 \sim 2$ GeV^2 and $x \sim 10^{-5}$. A major part of the problem in identifying the underlying small x dynamics is due to the parametric freedom that we have in specifying the initial parton distributions. For instance for a non-singular gluon input we can increase the steepness of F_2 with decreasing x by simply reducing Q_0^2 and increasing the DGLAP evolution length, $\ln(Q^2/Q_0^2)$. Alternatively, we could use (as in the global parton analyses [22, 23]) a singular input form $xg(x, Q_0^2) \sim x^{-\lambda}$, with λ chosen to fit the data. Also subleading $\ln(1/x)$ corrections will reduce the $x^{-\lambda}$ BFKL growth, see Section 2.3.4. In addition there are non-perturbative ambiguities in

[6] Of course in practice we need to sum all $\alpha_S^m \ln^n(1/x) \ln^p(Q^2/Q_0^2)$ contributions.

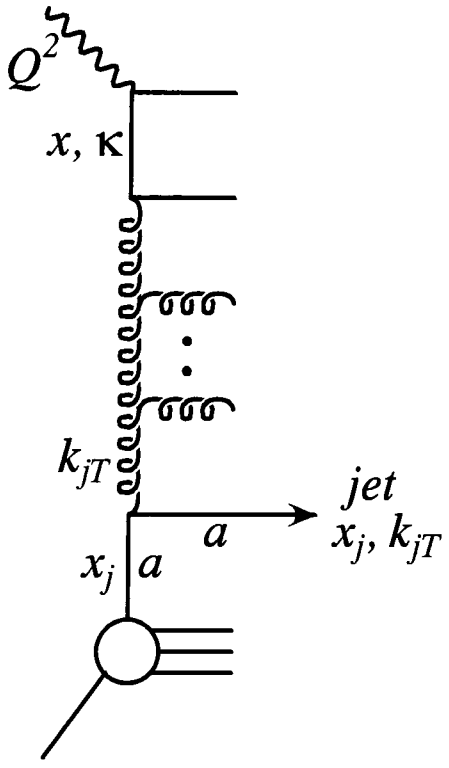

Figure 3.1: Diagrammatic representation of a deep inelastic event containing an identified jet carrying a fraction x_j of the proton's momentum and transverse momentum k_{jT}. The jet arises from a parton a which can either be a quark (as shown) or a gluon.

the BFKL description of F_2 arising from a diffusion in $\ln k_T^2$ into the infrared region which accompanies the evolution of the input gluon distribution $f(x, k_T^2)$ to smaller values of x. This leads to a significant contribution from the infrared region which is beyond the scope of perturbative QCD and has to be included phenomenologically. Because of these problems it is difficult to isolate $\ln(1/x)$ effects from measurements of F_2. We have to consider less inclusive quantities.

In 1991 Mueller [39] proposed an experiment which focusses on the small-x behaviour of QCD and does not depend on unknown input x distributions. His idea was to investigate deep-inelastic (x, Q^2) events which contain an identified energetic forward jet (x_j, k_{jT}^2) where $x_j \gg x$ and $k_{jT}^2 \simeq Q^2$. The process is illustrated in Fig. 3.1 where the jet arises from a parton a which is shown as a quark but could also be a gluon. We select events where

the jet's transverse momentum satisfies $k_{jT}^2 \simeq Q^2$ so that DGLAP evolution is neutralized and we can search for BFKL resummation effects. Q^2 also has to be sufficiently large so as to suppress diffusion into the infrared region when we solve the BFKL equation at decreasing values of x/x_j. The jet's longitudinal momentum $x_j p$ is chosen to be as large as is experimentally feasible (while x is as small as possible) so that we are able to probe the region of small x/x_j, typically $x_j > 0.05$. In this case the transverse momenta at the gluon – parton a vertex are to a good approximation strongly ordered which means that the exchanged gluon and the jet have basically the same transverse momentum, as shown in Fig. 3.1. So why is the DIS + jet measurement so special?

The requirement $k_{jT}^2 \simeq Q^2$

As we have already mentioned above, the transverse momentum of the identified jet is required to satisfy $k_{jT}^2 \simeq Q^2$. Since the evolution length for DGLAP evolution is proportional to $\alpha_S \ln(Q^2/k_{jT}^2)$, this implies that we can safely neglect the effects of DGLAP evolution and focus on BFKL effects.

The choice $k_{jT}^2 \simeq Q^2$ also has a second advantage. As described in the previous chapter, BFKL evolution is accompanied by a diffusion in $\ln k_T^2$ along the gluon ladder. When we use the BFKL equation to evolve to smaller x values this can, in principle, lead to a penetration of the infrared region where perturbative QCD is not applicable. This is the case in the calculation of the structure function F_2 as is shown schematically in Fig. 3.2(a). Here BFKL evolution was started at x_0 from an input gluon centred about transverse momentum squared $\overline{k}_{input}^2$. The transverse momentum squared at the end of the evolution, at x, is that of the quark-loop, $\overline{k}_{box}^2$, which is of the order of Q^2. We see that clearly a diffusion into the non-perturbative region (which is represented by a shaded area in Fig. 3.2) is possible. On the other hand, if, as for the DIS + jet process, we require $k_{jT}^2 \simeq Q^2$ where Q^2 is not too small, there is still a random walk in $\ln k_T^2$ but with the additional constraint that we have to reach a fixed value. Then the penetration of the non-perturbative region is suppressed. This is depicted in Fig. 3.2(b) which is often refered to as "Bartels' cigar" [43].

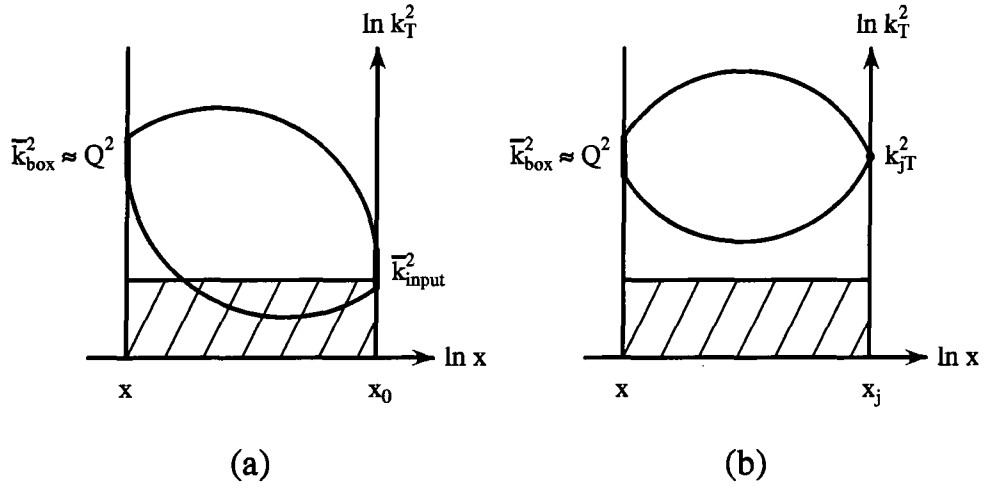

Figure 3.2: The diffusion in $\ln k_T^2$ which accompanies BFKL evolution to smaller values of x (a) in the calculation of the structure function F_2 and (b) for the DIS + jet process. The shaded area corresponds to the non-perturbative region.

The requirement $x_j \gg x$

We select events where the additional jet carries a fraction x_j of the proton's longitudinal momentum which is large while x is small. Since then x/x_j is small it should be possible to identify the $x^{-\lambda}$ behaviour, or to be precise the $(x/x_j)^{-\lambda}$ behaviour as $x/x_j \to 0$. This can be seen by looking at the differential structure function for the DIS + jet process in terms of the jet variables. We anticipate that according to BFKL dynamics the differential structure function has the leading small x/x_j behaviour [39, 44 – 48]

$$x_j\, k_{jT}^2 \frac{\partial F_2}{\partial x_j \partial k_{jT}^2} \sim \alpha_S(k_{jT}^2) \left[x_j \sum_a f_a(x_j, k_{jT}^2) \right] \left(\frac{x}{x_j} \right)^{-\lambda} \tag{3.1}$$

where, assuming t-channel pole dominance, the sum over the parton distributions is given by [39, 44, 47 – 48]

$$\sum_a f_a(x_j, k_{jT}^2) = g + \frac{4}{9} \sum_q (q + \overline{q}) \tag{3.2}$$

with the sum running over the quark flavours. The crucial point is that the parton distributions (g, q and $\overline{q}$) are to be evaluated at (x_j, k_{jT}^2) where they are *well-known* from the global parton analyses. Therefore the observation of DIS + jet events offers the opportunity to expose BFKL-type small x dynamics free from the ambiguities associated

with the choice of the non-perturbative parton input. In other words we are studying small x dynamics by deep inelastic scattering off a known *parton*, rather than off the *proton*. As a matter of fact, the small x/x_j behaviour of the differential structure function (3.1) is directly linked with the high-energy behaviour of the virtual photon - parton a cross section. To see this we express the centre-of-mass energy squared $s_{\gamma a}$ for this partonic subprocess as

$$s_{\gamma a} \simeq 2k_a \cdot q \simeq 2x_j p \cdot q. \tag{3.3}$$

Here we noted that the four-momentum of the exchanged parton a in Fig. 3.1 is $k_a \simeq x_j p$ due to the strong ordering of the longitudinal momenta which holds at the gluon – a vertex, since x_j is $O(1)$. Using (1.7) we find

$$s_{\gamma a} \simeq \left(\frac{x_j}{x}\right) Q^2. \tag{3.4}$$

Thus in the DIS + jet measurement the QCD small x behaviour is associated with the high-energy behaviour of a *partonic* cross section.

In this chapter we will first concentrate on the formalism for deep inelastic scattering containing a forward jet. That is we will show how the cross section for this measurement can be calculated from BFKL dynamics. We will find that the cross section is given by differential structure functions which indeed depend on x/x_j in the way we anticipated in (3.1). In particular we will review the approximate analytic solution of the BFKL equation for fixed coupling and then proceed to a more realistic numerical solution which allows the introduction of a running coupling. In the second part of the chapter we will study the kinematics for deep inelastic scattering in general and the DIS + jet process in particular. We will be investigating the limitations due to the detector architecture at HERA and also the cuts necessary to select DIS + jet events so that an identification of the underlying dynamics is possible.

3.2 The cross section for deep inelastic + jet events

In this section we will calculate the cross section for the process in which deep inelastic scattering is accompanied by a single identified energetic jet in the final state, i.e.

$$\gamma^{\star} + p \rightarrow \text{jet}(x_j, k_{jT}^2) + X. \tag{3.5}$$

The variables of the process are shown in Fig. 3.1. As introduced in Chapter 1 the dimensionless variables x and y are given by $x = Q^2/2p \cdot q$ and $y = p \cdot q/p_e \cdot p$ where p, p_e and q denote the four momenta of the proton, the incident electron and the virtual photon respectively, and $Q^2 \equiv -q^2$. Recall that the variables x_j and k_{jT} are the longitudinal momentum fraction and transverse momentum carried by the jet. The DIS + jet cross section which we now have to compute can be represented by the diagram displayed in Fig. 3.3. We can express the corresponding differential cross section in terms of two differential structure functions in the following way [47, 49]:

$$\frac{\partial \sigma_j}{\partial x \partial Q^2} = \int dx_j \int dk_{jT}^2 \frac{4\pi\alpha^2}{xQ^4} \left[(1-y) \frac{\partial F_2}{\partial x_j \partial k_{jT}^2} + \frac{1}{2} y^2 \frac{\partial F_T}{\partial x_j \partial k_{jT}^2} \right] \tag{3.6}$$

If we assume that the longitudinal momenta at the gluon – parton a vertex are strongly ordered so that the longitudinal momentum fraction of the struck parton is to a good approximation equal to x_j of the outgoing jet, then the differential structure functions have the leading small x/x_j form [39, 44, 47 - 48]

$$x_j \frac{\partial^2 F_i}{\partial x_j \partial k_{jT}^2} = \frac{3\alpha_S(k_{jT}^2)}{\pi k_{jT}^4} \left[x_j \sum_a f_a \left(x_j, k_{jT}^2 \right) \right] \Phi_i \left(\frac{x}{x_j}, k_{jT}^2, Q^2 \right) \tag{3.7}$$

for $i = T, L$. The transverse (T) and longitudinal (L) structure functions are related to F_1 and F_2 which we introduced in Chapter 1 in the following way:

$$F_T = 2xF_1 \tag{3.8}$$

$$F_L = F_2 - 2xF_1. \tag{3.9}$$

The factor k_{jT}^{-4} in (3.7) arises from the gluon propagators. The proton – parton a subprocess is described by the term $x_j \sum_a f_a \left(x_j, k_{jT}^2 \right)$ where the sum over the parton distributions

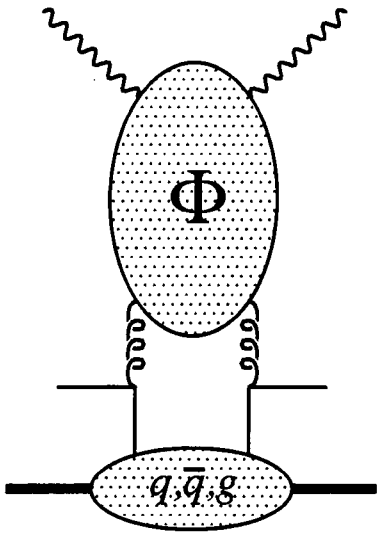

Figure 3.3: Diagrammatic representation of the cross section for deep inelastic scattering with an identified forward jet. Here the jet is represented by a quark line but it could also be a gluon.

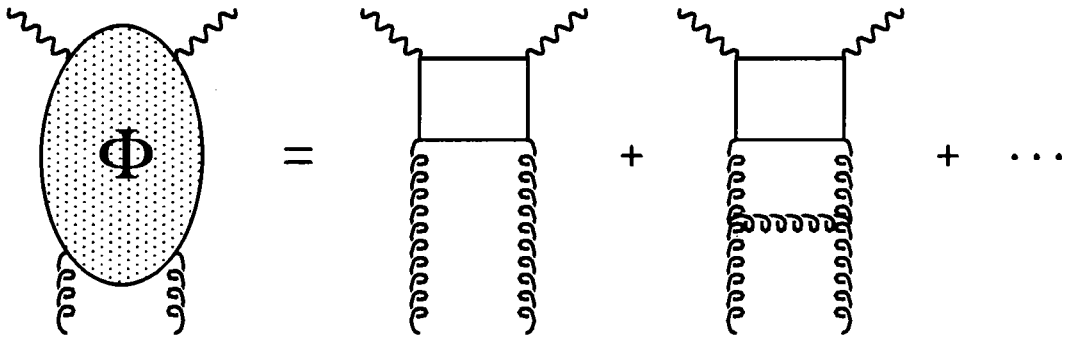

Figure 3.4: The leading $\ln(x/x_j)$ approximation of the functions Φ_i occurring in (3.7) and in the DIS + jet cross section diagram (Fig. 3.3).

is given by (3.2). Recall that these parton distributions are to be evaluated at (x_j, k_{jT}^2) and that we choose x_j to be as large as is experimentally feasible. This means that we only need the parton distributions where they are well-known from the global analyses, so there are no ambiguities arising from a non-perturbative input.

Let us for the moment omit the subscript j on k_{jT} and define

$$z \equiv \frac{x}{x_j} \tag{3.10}$$

which is small since x_j is chosen to lie in the large-x region. The functions $\Phi_i(z, k_T^2, Q^2)$ in (3.7) describe the gluon ladder which couples to the incoming virtual photon. To be precise, the factors Φ_i/k_T^2 can be identified with the virtual gluon structure functions integrated over the longitudinal momentum of the gluon. In the leading $\ln z$ approximation the Φ_i can be represented by sums of ladder diagrams as shown in Fig. 3.4 and are obtained by solving the BFKL equations [26]

$$\begin{aligned}\Phi_i(z, k_T^2, Q^2) \;=\; & \Phi_i^{(0)}(z, k_T^2, Q^2) + \frac{3\alpha_S}{\pi} k_T^2 \int_z^1 \frac{dz'}{z'} \int_0^\infty \frac{dk_T'^2}{k_T'^2} \\ & \left[\frac{\Phi_i(z', k_T'^2, Q^2) - \Phi_i(z', k_T^2, Q^2)}{|k_T'^2 - k_T^2|} + \frac{\Phi_i(z', k_T^2, Q^2)}{\sqrt{4k_T'^4 + k_T^4}} \right]\end{aligned} \tag{3.11}$$

for $i = T, L$. Here the inhomogeneous or driving terms $\Phi_i^{(0)}$ describe the virtual photon – virtual gluon fusion process. They correspond to the sum of the quark box and "crossed" box contributions shown in Fig. 3.5. For simplicity we will in the future just refer to the sum of the two diagrams as the "quark box".

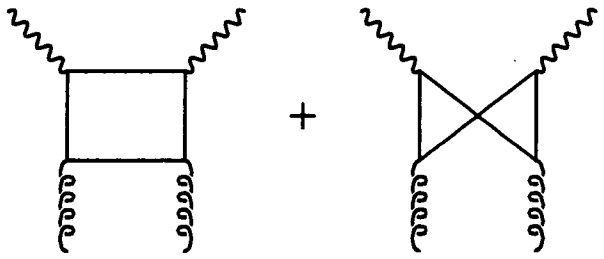

Figure 3.5: The quark box and "crossed" box contributions to the virtual γ - virtual gluon fusion process.

Since the BFKL equations (3.11) for the $\Phi_i(z, k_T^2, Q^2)$ are based on a leading $\ln(1/z)$ summation, they are not expected to be applicable in the large-z region. On the other hand, in this region the driving terms $\Phi_i^{(0)}(z, k_T^2, Q^2)$ should be a reasonable approximation to the $\Phi_i(z, k_T^2, Q^2)$ for the following reason: In the large-z region the standard DGLAP QCD evolution should be applicable, but because we choose events with $k_T^2 \simeq Q^2$ the evolution length $[\sim \alpha_S \ln(Q^2/k_T^2)]$ is very small and effects of the evolution can therefore be neglected. This implies that we can restrict our study of the BFKL equations (3.11) to the small-z region, $z < z_0$, by imposing the boundary condition [48]

$$\Phi_i(z_0, k_T^2, Q^2) \simeq \Phi_i^{(0)}(z_0, k_T^2, Q^2) \equiv \Phi_i^{(0)}(k_T^2, Q^2). \tag{3.12}$$

3.2.1 Calculation of the quark box diagram

As explained in refs. [41, 45] the $\Phi_i^{(0)}$ can be evaluated by expanding the four momenta in terms of the basic light-like four momenta p and $q' \equiv q + xp$. For example, the quark momentum κ in the box (see Fig. 3.1) has the Sudakov decomposition

$$\kappa = \alpha p - \beta q' + \boldsymbol{\kappa}_T. \tag{3.13}$$

Carrying out the integration over the box diagrams, subject to the quark mass-shell constraints, then yields [41, 45, 50]

$$\begin{aligned}\Phi_T^{(0)}(k_T^2, Q^2) &= 2\sum_q e_q^2 \frac{\alpha_S}{4\pi^2} Q^2 \int_0^1 d\beta \int d^2\kappa_T \\ &\quad \left\{ \left[\beta^2 + (1-\beta)^2\right] \left(\frac{\kappa_T^2}{D_1^2} - \frac{\boldsymbol{\kappa}_T.(\boldsymbol{\kappa}_T - \boldsymbol{k}_T)}{D_1 D_2} \right) + m_q^2 \left(\frac{1}{D_1^2} - \frac{1}{D_1 D_2} \right) \right\}\end{aligned} \tag{3.14}$$

$$\Phi_L^{(0)}(k_T^2, Q^2) = 2\sum_q e_q^2 \frac{\alpha_S}{\pi^2} Q^4 \int_0^1 d\beta \int d^2\kappa_T \, \beta^2(1-\beta)^2 \left(\frac{1}{D_1^2} - \frac{1}{D_1 D_2} \right). \tag{3.15}$$

where m_q is the quark mass and the denominators D_i are of the form

$$\begin{aligned} D_1 &= \kappa_T^2 + \beta(1-\beta)\, Q^2 + m_q^2 \\ D_2 &= (\boldsymbol{\kappa}_T - \boldsymbol{k}_T)^2 + \beta(1-\beta)\, Q^2 + m_q^2. \end{aligned} \tag{3.16}$$

Our aim is now to do the twofold $d^2\kappa_T$ integration. Let us first concentrate on the longitudinal contribution (3.15). The integration over the first term in the bracket can be done easily whereas in the second term we have to eliminate the angular dependence. The first step is to rewrite

$$\frac{1}{D_1 D_2} = \int_0^1 d\lambda \frac{1}{[\lambda D_1 + (1-\lambda)D_2]^2} \equiv \int_0^1 d\lambda \frac{1}{D^2} \tag{3.17}$$

where λ is the Feynman parameter and

$$D = \lambda\kappa_T^2 + (1-\lambda)(\boldsymbol{\kappa}_T - \boldsymbol{k}_T)^2 + \beta(1-\beta)\,Q^2 + m_q^2. \tag{3.18}$$

Since we want to only be left with terms quadratic in $\boldsymbol{\kappa}_T$ (or rather $\boldsymbol{\kappa}'_T$) we next substitute

$$\boldsymbol{\kappa}_T = \boldsymbol{\kappa}'_T + (1-\lambda)\boldsymbol{k}_T \tag{3.19}$$

and obtain

$$D = \kappa_T'^2 + \lambda(1-\lambda)\,k_T^2 + \beta(1-\beta)\,Q^2 + m_q^2. \tag{3.20}$$

Now, because we are integrating over all phase space, we have

$$\begin{aligned}\int_0^\infty \frac{d^2\kappa_T}{D_1 D_2} &= \pi \int_0^1 d\lambda \int_0^\infty \frac{d\kappa_T'^2}{[\kappa_T'^2 + \lambda(1-\lambda)\,k_T^2 + \beta(1-\beta)\,Q^2 + m_q^2]^2} \\ &= \pi \int_0^1 d\lambda \frac{1}{\lambda(1-\lambda)\,k_T^2 + \beta(1-\beta)\,Q^2 + m_q^2}.\end{aligned} \tag{3.21}$$

Treating the transverse contribution (3.15) in a similar way we then obtain

$$\begin{aligned}\Phi_T^{(0)}(k_T^2, Q^2) = \sum_q e_q^2 \frac{\alpha_S}{4\pi} Q^2 \int_0^1 d\lambda \int_0^1 d\beta \Bigg\{ & k_T^2 \frac{[\beta^2 + (1-\beta)^2]\,[\lambda^2 + (1-\lambda)^2]}{[\lambda(1-\lambda)k_T^2 + \beta(1-\beta)Q^2 + m_q^2]} \\ & + 2m_q^2 \left(\frac{1}{\beta(1-\beta)Q^2 + m_q^2} - \frac{1}{\lambda(1-\lambda)k_T^2 + \beta(1-\beta)Q^2 + m_q^2} \right) \Bigg\}\end{aligned} \tag{3.22}$$

$$\begin{aligned}\Phi_L^{(0)}(k_T^2, Q^2) = & \sum_q e_q^2 \frac{2\alpha_S}{\pi} Q^4 \int_0^1 d\lambda \int_0^1 d\beta\, \beta^2(1-\beta)^2 \\ & \left\{ \frac{1}{\beta(1-\beta)Q^2 + m_q^2} - \frac{1}{\lambda(1-\lambda)k_T^2 + \beta(1-\beta)Q^2 + m_q^2} \right\}.\end{aligned} \tag{3.23}$$

3.2.2 Analytic form of the solution Φ of the BFKL equation for fixed α_S

In practice we solve the BFKL equation (3.11) for Φ numerically, which allows the use of running α_S and the inclusion of a charm quark mass. However, it is informative to first recall the analytic solution which can be obtained if α_S is fixed and we assume that the quarks are massless. It is useful to define the functions

$$\varphi_i \equiv \frac{\Phi_i}{k_T^2} \tag{3.24}$$

which, as we mentioned before, can be identified with the virtual gluon structure functions integrated over the longitudinal momentum of the gluon. Analogously

$$\varphi_i^{(0)} \equiv \frac{\Phi_i^{(0)}}{k_T^2}. \tag{3.25}$$

Then the first step for the analytic solution of the BFKL equation is to rewrite the driving terms (3.22) and (3.23) for $m_q = 0$ in the form

$$\varphi_T^{(0)}(k_T^2, Q^2) = \sum_q e_q^2 \frac{\alpha_S}{4\pi} Q^2 \int_0^1 d\lambda \int_0^1 d\beta \frac{[\beta^2 + (1-\beta)^2]\,[\lambda^2 + (1-\lambda)^2]}{[\lambda(1-\lambda)k_T^2 + \beta(1-\beta)Q^2]} \tag{3.26}$$

$$\varphi_L^{(0)}(k_T^2, Q^2) = \sum_q e_q^2 \frac{2\alpha_S}{\pi} Q^2 \int_0^1 d\lambda \int_0^1 d\beta \frac{\lambda(1-\lambda)\beta(1-\beta)}{[\lambda(1-\lambda)k_T^2 + \beta(1-\beta)Q^2]}. \tag{3.27}$$

We see that, for fixed α_S and $m_q = 0$, the functions $\varphi_i^{(0)}$ are functions of a single dimensionless variable $r = Q^2/k_T^2$. We may therefore represent the driving terms $\varphi_i^{(0)}(Q^2/k_T^2)$ in terms of their Mellin transforms $\tilde{\varphi}_i^{(0)}(\gamma)$

$$\varphi_i^{(0)}(r) = \frac{1}{2\pi i} \int_{\frac{1}{2}-i\infty}^{\frac{1}{2}+i\infty} d\gamma\, \tilde{\varphi}_i^{(0)}(\gamma)\, r^{\gamma} \tag{3.28}$$

where $i = L, T$ and $r \equiv Q^2/k_T^2$. The functions $\tilde{\varphi}_i^{(0)}(\gamma)$ can be obtained from the inverse relation to (3.28),

$$\tilde{\varphi}_i^{(0)} = \int_0^{\infty} dr\, r^{-\gamma-1}\, \varphi_i^{(0)}(r). \tag{3.29}$$

Substituting for $\varphi_i^{(0)}(r)$ the expressions given in (3.26) and (3.27) and performing the r integration we find

$$\begin{aligned}\tilde{\varphi}_T^{(0)} &= \sum_q e_q^2 \frac{\alpha_S}{4\sin\pi\gamma} \int_0^1 d\lambda \left[\lambda(1-\lambda)\right]^{-\gamma} \left[\lambda^2+(1-\lambda)^2\right] \\ &\qquad \int_0^1 d\beta \left[\beta(1-\beta)\right]^{\gamma-1} \left[\beta^2+(1-\beta)^2\right] \\ &= \sum_q e_q^2 \frac{\alpha_S}{\sin\pi\gamma} B(\gamma+2,\gamma)\, B(3-\gamma,1-\gamma) \qquad (3.30)\end{aligned}$$

$$\begin{aligned}\tilde{\varphi}_L^{(0)} &= \sum_q e_q^2 \frac{2\alpha_S}{\sin\pi\gamma} \int_0^1 d\lambda \left[\lambda(1-\lambda)\right]^{1-\gamma} \left[\lambda^2+(1-\lambda)^2\right] \\ &\qquad \int_0^1 d\beta \left[\beta(1-\beta)\right]^{\gamma} \left[\beta^2+(1-\beta)^2\right] \\ &= \sum_q e_q^2 \frac{2\alpha_S}{\sin\pi\gamma} B(-\gamma+2,-\gamma+2)\, B(\gamma+1,\,\gamma+1). \qquad (3.31)\end{aligned}$$

The Mellin transform is useful since it diagonalizes the BFKL equations (3.11). In other words we can write the differential form of the equations as

$$\frac{\partial\tilde{\varphi}_i(\gamma)}{\partial\ln(1/z)} = \tilde{K}(\gamma)\,\tilde{\varphi}_i(\gamma) \qquad (3.32)$$

where $\tilde{K}(\gamma)$ is the Mellin transform of the BFKL kernel,

$$\tilde{K}(\gamma) = \frac{3\alpha_S}{\pi}[2\Psi(1)-\Psi(\gamma)-\Psi(1-\gamma)],$$

see (2.40), with $\Psi(\gamma)\equiv\Gamma'(\gamma)/\Gamma(\gamma)$. The solutions of (3.32) are of the form

$$\tilde{\varphi}_i(\gamma) = \tilde{\varphi}_i^{(0)}(\gamma)\,\exp\left(\tilde{K}(\gamma)\ln\frac{1}{z}\right). \qquad (3.33)$$

Performing the inverse Mellin transform we find

$$\varphi_i(z,k_T^2,Q^2) = \frac{1}{2\pi i}\int_{\frac{1}{2}-i\infty}^{\frac{1}{2}+i\infty} d\gamma \left(\frac{Q^2}{k_T^2}\right)^{\gamma} \exp\left(\tilde{K}(\gamma)\ln\frac{1}{z}\right)\tilde{\varphi}_i^{(0)}(\gamma). \qquad (3.34)$$

These are the solutions of the BFKL equations (3.11) for fixed coupling α_S and assuming massless quarks. In the $z\to 0$ limit the formulae reduce to the conventional $z^{-\lambda}$ BFKL behaviour

$$\varphi_i(z,k_T^2,Q^2) \sim z^{-\tilde{K}(\frac{1}{2})} \left(\frac{Q^2}{k_T^2}\right)^{\frac{1}{2}} \frac{\tilde{\varphi}_i^{(0)}(\gamma=\frac{1}{2})}{\left(\tilde{K}''(\frac{1}{2})\ln 1/z\right)^{\frac{1}{2}}} \qquad (3.35)$$

where $\tilde{K}''(\frac{1}{2}) = \frac{3\alpha_S}{\pi} 28\zeta(3)$. For simplicity we have omitted the Gaussian diffusion factor in $\ln(k_T^2/Q^2)$. If we evaluate the various functions at $\gamma = \frac{1}{2}$ we obtain

$$\begin{aligned} \varphi_T(z, k_T^2, Q^2) &= \frac{9\pi^2}{512} \frac{2\sum e_q^2 \, \alpha_S^{\frac{1}{2}}}{\sqrt{21\zeta(3)/2}} \left(\frac{Q^2}{k_T^2}\right)^{\frac{1}{2}} \frac{z^{-\lambda}}{\sqrt{\ln(1/z)}} \left[1 + O\left(\frac{1}{\ln(1/z)}\right)\right] \\ \varphi_L(z, k_T^2, Q^2) &= \frac{2}{9} \varphi_T(z, k_T^2, Q^2) \end{aligned} \tag{3.36}$$

where $\lambda = \tilde{K}(\frac{1}{2}) = \frac{3\alpha_S}{\pi} 4\ln 2$, see (2.45).

3.2.3 Numerical evaluation of Φ for running α_S

Above we showed how the BFKL equations for the functions Φ_i $(i = T, L)$ can be solved analytically for fixed coupling. This technique only gives a rough estimate of the value of the $\Phi_i(z, k_T^2, Q^2)$ for the following two reasons. First the integration over k_T^2 in the BFKL equations (3.11) starts from 0 which implies that the gluons emitted along the chain in Fig. 3.1 can have a very small transverse momentum. However, for perturbation theory to be applicable they should satisfy $k_T^2 \gg \Lambda^2$. Second the analytic solution is only possible for fixed coupling. Therefore, in practice, we evaluate the BFKL equations numerically imposing a lower limit cut-off k_0^2 on the transverse momentum integration and letting the coupling α_S run. To introduce the k_T^2 dependence of α_S in (3.11) we follow the prescription of ref. [48]. That is we ensure that if we assumed strong ordering $k_T^2 \ll Q^2$, we would recover the correct evolution equations in the double leading logarithm approximation with running coupling. This means we have to solve the BFKL equations for

$$H_i(z, k_T^2, Q^2) = \frac{3\alpha_S(k_T^2)}{\pi} \Phi_i(z, k_T^2, Q^2). \tag{3.37}$$

Actually, we solve the differential form of the equations

$$\begin{aligned} \frac{\partial H_i(z, k_T^2, Q^2)}{\partial \log(1/z)} &= \frac{3\alpha_S(k_T^2)}{\pi} k_T^2 \int_{k_0^2}^{\infty} \frac{dk_T'^2}{k_T'^2} \\ &\times \left[\frac{H_i(z, k_T'^2, Q^2) - H_i(z, k_T^2, Q^2)}{|k_T'^2 - k_T^2|} + \frac{H_i(z, k_T^2, Q^2)}{\sqrt{4k_T'^4 + k_T^4}}\right] \end{aligned} \tag{3.38}$$

subject to the boundary conditions

$$H_i(z = z_0, k_T^2, Q^2) = H_i^{(0)}(k_T^2, Q^2). \tag{3.39}$$

with the functions $H_i^{(0)}$ defined by an expression analogous to (3.37). For reasons given later, we choose $z_0 \simeq 0.1$ and the cut-off $k_0^2 = 1$ GeV^2. For any small z the solutions $H_i(z, k_T^2, Q^2)$ therefore only depend on the behaviour of H_i in the interval (z, z_0). We find that the slope $\lambda = \alpha_P - 1$ and the overall normalization of the solution of the BFKL equation with running coupling α_S are in general smaller than those obtained with fixed coupling $\alpha_S(Q^2)$, see for example Fig. 6 in [48].

3.2.4 Predictions for the differential structure function

Now we are in a position to predict the behaviour of the differential structure function, $\partial F_2/\partial x_j \partial k_{jT}^2$, for deep inelastic events containing an identified forward jet as a function of x_j and x for fixed values of k_{jT}^2 and Q^2. Note that F_2 is given by $F_2 = F_T + F_L$. Since we are searching for a signature of BFKL effects, we first evaluate (3.7) using the functions Φ_i obtained from the BFKL equations (3.11). Next we neglect BFKL evolution in the calculation which can easily be done by substituting for the Φ_i the quark box contributions $\Phi_i^{(0)}$ only. The results are shown in Fig. 3.6 as a function of x_j for different values of x. The solid curves are the BFKL predictions for the differential structure function, whereas the dashed curves were obtained substituting $\Phi_i = \Phi_i^{(0)}$ in (3.7), that is the difference between the solid and the dashed curves is the "Lipatov effect" which is due to the BFKL resummation of the $\alpha_S \ln(x_j/x)$ terms. Particularly for small x and large x_j ($x_j \simeq 0.1$) this difference is dramatic. Let us emphasize again here that x_j/x in fact has to be large for our BFKL formalism to be valid and that the results displayed in Fig. 3.6 are therefore only expected to be reliable for $x_j \gtrsim 0.05$. Note also that if we compare the solid curves for a fixed value of x_j, we see the rapid increase of the differential structure function with decreasing z which is characteristic for BFKL dynamics. Let us for example consider the BFKL based results for $x_j = 0.1$. We find that if x decreases from $x = 10^{-2}$ to $x = 10^{-4}$ the differential structure function rises by approximately a factor of 10, which is what we expect for an $(x/x_j)^{-\lambda}$ behaviour with $\lambda \simeq 0.5$.

It is tempting to conclude that the measurement of deep inelastic events with an identified jet can reveal the singular BFKL behaviour from observing either the shape or

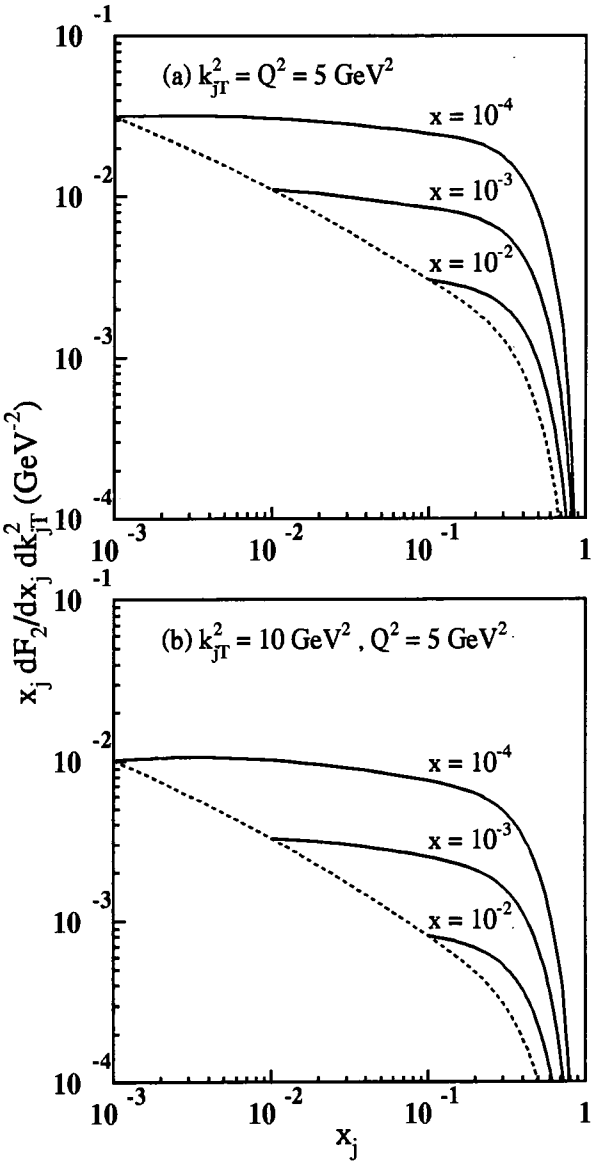

Figure 3.6: The F_2 differential structure function, (3.7), for deep-inelastic (x, Q^2) events accompanied by an identified forward jet (x_j, k_{jT}^2) as a function of x_j for different values of $x, x = 10^{-4}, 10^{-3}$ and 10^{-2}, and for $Q^2 = 5$ GeV^2. The continuous curves correspond to inputting into (3.7) the solution Φ_2 of the BFKL equation (3.11), whereas the dashed curve is calculated using for Φ_2 simply the driving term $\Phi_2^{(0)}$ of (3.22) and (3.23). Plots (a) and (b) correspond to jets with $k_{jT}^2 = 5$ and 10 GeV^2 respectively.

the magnitude of the differential structure function $\partial F_2/\partial x_j \partial k_{jT}^2$. However, it turns out that the shape in x or x_j is a more reliable discriminator than the magnitude because the normalisation of the BFKL predictions is subject to uncertainties. These uncertainties are mainly due to the choice of the cutoffs on the transverse momentum integrations, e.g. the cutoff k_0^2 in the BFKL equations (3.38). Analogously, we could have introduced a cutoff on the κ_T integrations in expressions (3.14) and (3.15) for the quark box contributions. The effect of these cutoffs on the differential structure function is shown in Figs. 8 and 9 of ref. [48].

3.3 Cuts for the DIS + jet process

Obtaining the differential structure functions from BFKL dynamics in the way we explained above and substituting them into (3.6) yields the differential cross section for the DIS + jet process. When we do the x_j and k_{jT}^2 integrations in (3.6) and when we integrate over x and Q^2 to obtain the total cross section we have to impose various cuts due to technical limitations of the detectors at HERA and because of the way in which we select DIS + jet events. In the following we will discuss what cuts we have to use and why.

3.3.1 The HERA electron acceptance region

We will now study the accessible region in x and Q^2 for deep inelastic scattering $e^{\pm}p \to e^{\pm}X$ at HERA. The kinematic variables are defined in Fig. 3.7. At HERA the nominal electron energy $E_e = 30$ GeV and the proton energy $E_p = 820$ GeV resulting in a centre-of-mass energy $\sqrt{s} = \sqrt{4E_eE_p} \simeq 300$ GeV. In the previous sections we already used the variables x, y and Q^2. As a reminder $x = Q^2/2p \cdot q$, $y = p \cdot q/p_e \cdot p$ and $Q^2 = -q^2 = xys$ where p, p_e and q are the four momenta pf the proton, the incoming electron (or positron) and the virtual photon respectively. We can express Q^2 and y in terms of the energies of the incoming and outgoing electron (or positron) and the angle θ'_{ep} of the scattered electron with respect to the proton beam direction in the HERA laboratory frame [51]:

$$Q^2 = 4E_eE'_e \cos^2 \frac{\theta'_{ep}}{2} \tag{3.40}$$

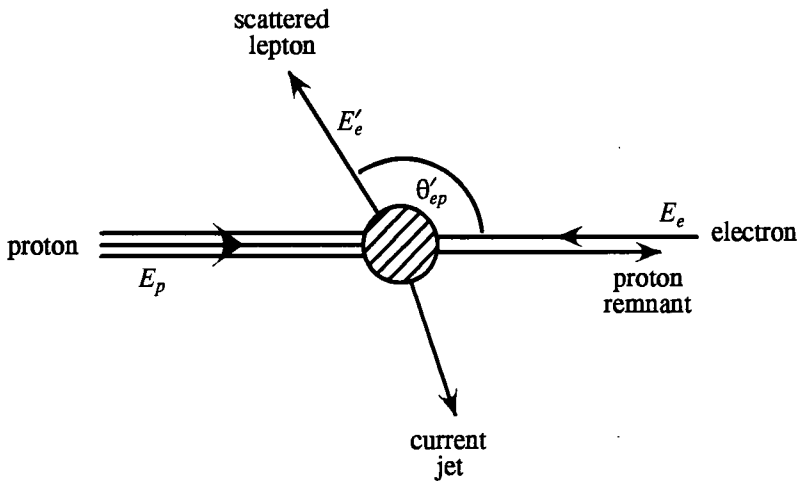

Figure 3.7: Kinematics of a deep inelastic event.

$$y = 1 - \frac{E'_e}{E_e} \sin^2 \frac{\theta'_{ep}}{2}. \tag{3.41}$$

We will be using these relations to find expressions for the limits on the (x, Q^2) range accessible at HERA.

The most severe limitation on the accessible kinematic region at HERA is due to particle losses in the beam pipe. For the outgoing electron to be detectable we have to require that it is scattered by an angle

$$8° < \theta'_{ep} < 172°. \tag{3.42}$$

For fixed values of θ'_{ep} we can calculate the resulting limit on the (x, Q^2) plane from

$$Q^2 = \frac{sx}{1 + xE_p \tan^2(\theta'_{ep}/2)/E_e} \tag{3.43}$$

which follows from (3.40) and (3.41). Fig. 3.8 shows the relevant part of the lower boundary for $\theta'_{ep} < 172°$ obtained in this way.

Another problem is that the quality of the measurement becomes poor for high y for the following two reasons. First, at high y there are backgrounds due to electrons originating in charm decays with small energies and $\pi\gamma$ overlap from photoproduction

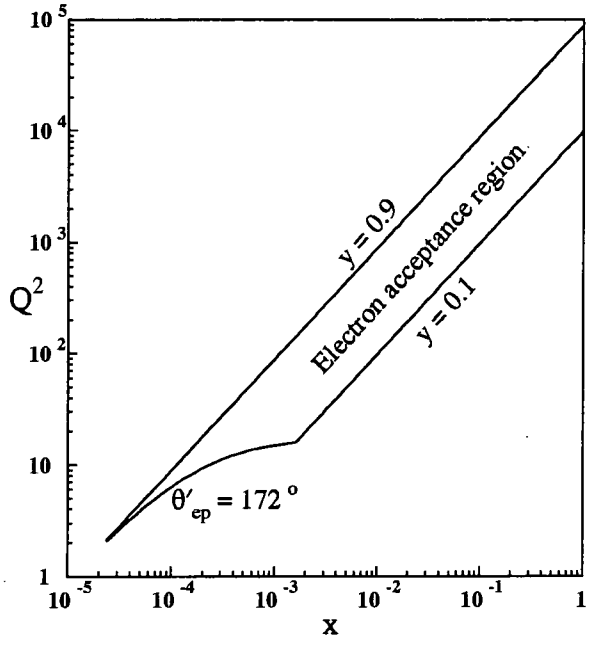

Figure 3.8: The acceptance region in the (x, Q^2) plane for deep inelastic events defined by $8° < \theta'_{ep} < 172°$ and $0.1 < y < 0.9$.

events [51]. These electrons can easily be mistaken for deep inelastic electrons. Second, radiative corrections are expected to be large for high y which means that the momentum of the incoming electron is smaller than the beam value. We therefore impose an upper limit on the accessible y range,

$$y < 0.9. \tag{3.44}$$

We will also have to introduce a lower cut on y due to errors occurring in the reconstruction of x and Q^2. From (3.40) and (3.41) we find that the resolutions for these variables are of the form

$$\frac{\Delta Q^2}{Q^2} = \frac{\Delta E'_e}{E'_e} + \tan\left(\frac{\theta'_{ep}}{2}\right)\Delta\theta'_{ep} \tag{3.45}$$

$$\frac{\Delta x}{x} = \frac{1}{y}\frac{\Delta E'_e}{E'_e} + \frac{1}{y}\left[\frac{1-y}{\sin^2(\theta'_{ep}/2)} - 1\right]\tan\left(\frac{\theta'_{ep}}{2}\right)\Delta\theta'_{ep}. \tag{3.46}$$

Both x and Q^2 should be determined with a reasonable resolution for the measurement to be reliable. However, from (3.46) we see that if only information on the scattered electron is used, the low y region has to be excluded because the x resolution is singular for $y \to 0$.

A reasonable cut is

$$y > 0.1. \tag{3.47}$$

Using

$$y = \frac{Q^2}{xs} \tag{3.48}$$

the limits on y can be easily converted into boundaries on the (x, Q^2) range which are shown in Fig. 3.8. The HERA electron acceptance region is obtained by combining the cuts on y and θ'_{ep}.

So far we have not considered any cuts on the energy E'_e of the scattered electron. We have to, however, take into account that the calorimeter resolution degrades for small values of E'_e. Therefore we impose the constraint

$$E'_e > 5 \text{ GeV}. \tag{3.49}$$

To calculate E'_e we use the equality

$$E'_e = E_e \left(1 - y + \frac{Q^2}{4E_e^2}\right) \tag{3.50}$$

which easily follows from (3.40) and (3.41). Since the resolution of the hadronic calorimeter also becomes poor for small jet energies we would in principle have to introduce a similar cut on the energy of the additional jet in a DIS + jet event. But this will not be necessary because, as we will see in the following subsection, we require this jet to be energetic for a different reason.

3.3.2 DIS + jet event kinematics

Fig. 3.9 displays the kinematics of a DIS + jet event. To be able to identify BFKL dynamics with the DIS + jet measurement we have to select events where the transverse momentum of the extra jet $k_{jT}^2 \simeq Q^2$ so that DGLAP evolution along the gluon ladder is suppressed and take k_{jT}^2 sufficiently large so that the diffusion in $\ln k_T^2$ does not lead to a penetration of the infrared region. We therefore require

$$\frac{1}{2}Q^2 < k_{jT}^2 < 2Q^2. \tag{3.51}$$

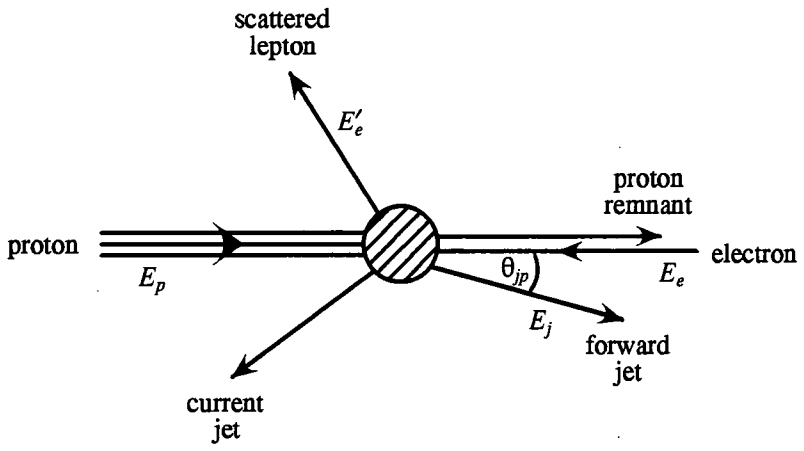

Figure 3.9: Kinematics of the DIS + jet process.

From the theoretical point of view we want x_j to be large so that we only need to input the parton distributions where they are well-known from the global analyses. Large x_j also means that x/x_j is small allowing us to study the $(x/x_j)^{-\lambda}$ behaviour as $x/x_j \to 0$. However, as we will see now, large x_j means that for fixed k_{jT}^2 the jet is emitted at a small angle θ_{jp} with respect to the proton beam direction in the HERA laboratory frame.

It is convenient to translate the variables x_j, k_{jT}^2, which are given in the virtual photon – proton centre-of-mass frame, into the HERA variables θ_{jp}, E_j for fixed x, Q^2. As a first step we express the four momentum p_j of the jet in terms of the light-like four momenta p and $q' \equiv q + xp$. We then have

$$p_j = xp + \frac{k_{jT}^2}{xs'}q' + k_{jT} \tag{3.52}$$

where $s' = 2p \cdot q$ and find the following relations [52]:

$$2p \cdot p_j = \frac{k_{jT}^2}{x_j} = 2E_j E_p(1 - \cos\theta_{jp}) \tag{3.53}$$

$$2q \cdot p_j = x_j s' - \frac{x}{x_j}k_{jT}^2 = 2E_j(E_e - E'_e + \tilde{E}). \tag{3.54}$$

If we now write the four momentum of the outgoing lepton (in our case an electron or positron) as

$$p'_e = (E'_e, x'_e, y'_e, z'_e) \tag{3.55}$$

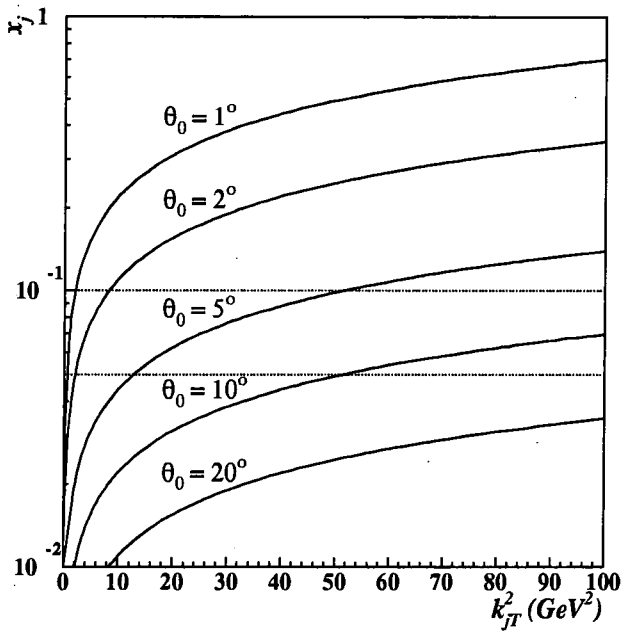

Figure 3.10: The relation between the jet kinematic variables for DIS + jet events with $x = 6 \times 10^{-4}$ and $Q^2 = 20$ GeV^2 for various choices of the angle θ_0. In the HERA (30×820 GeV) laboratory frame the jet angle θ_{jp} to the proton direction is not uniquely specified by $(x, Q^2; x_j, k_{jT}^2)$. Varying the remaining azimuthal angle transforms the lines of constant θ_{jp} into narrow bands in the x_j, k_{jT}^2 plane. Here we averaged over the azimuthal degree of freedom. The plot is insensitive to variations of x, Q^2 over their relevant intervals. The continuous lines are the *upper* boundary on the allowed kinematic region for different choices of θ_0. The dotted lines represent the *lower* boundary for the choices $x_j > 0.1$ and $x_j > 0.05$.

then we have [53]

$$\tilde{E} = E_e \cos\theta_{jp} - x'_e \sin\theta_{jp} \cos\phi_{jp} - y'_e \sin\theta_{jp} \sin\phi_{jp} - z'_e \cos\theta_{jp}. \tag{3.56}$$

The azimuthal angle ϕ_{jp} of the jet is not uniquely specified by $(x, Q^2; x_j, k_{jT}^2)$. We will therefore average over all possible azimuthal angles. Using (3.53) and (3.54) we can derive a relationship between the jet momenta and the jet angle θ_{jp},

$$x_j^2 = \frac{x}{Q^2}\left[\frac{k_{jT}^2 (E_e - E'_e + \tilde{E})}{E_p (1 - \cos\theta_{jp})} + x k_{jT}^2\right]. \tag{3.57}$$

Fig. 3.10 shows the dependence of x_j on k_{jT}^2 for fixed values of θ_{jp}. As anticipated, we see that for fixed k_{jT}^2 large x_j jets are only emitted at small angles θ_{jp} (which is why the additional jet is often referred to as the "forward jet"). In order to avoid that the jet

is lost in the proton beam pipe or that it mingles with the proton remnants we have to impose a cut $\theta_{jp} > \theta_0$. Then the solid lines in Fig. 3.10 represent the upper boundary on the allowed kinematic region for different choices of θ_0. For the jet to be measurable in the HERA detectors we require

$$\theta_{jp} > \theta_0 = 5^\circ. \tag{3.58}$$

At the same time we need x_j to be as large as possible. From Fig. 3.10 we see that for a given θ_{jp} we can reach larger values of x_j by observing jets with larger k_{jT}^2 but then the event rate is depleted. If we were to take $x_j > 0.1$ as would be theoretically favourable we would only be left with a very small allowed kinematic region at large k_{jT}^2. We therefore impose the cut

$$x_j > 0.05. \tag{3.59}$$

The corresponding lower boundary on the allowed kinematic region is shown as the lower dotted line in Fig. 3.10.

Lastly, we impose the theoretical cut

$$z = \frac{x}{x_j} < 0.1 \tag{3.60}$$

so that z is small and the BFKL formalism is appropriate for the calculation of the DIS + jet cross section.

3.4 Summary and outlook

We studied deep inelastic events containing an identified energetic jet in the final state as a way of exposing BFKL dynamics at HERA. As we saw this measurement has several advantages. Since we choose events where the transverse momentum of the jet satisfies $k_{jT}^2 \simeq Q^2$, conventional DGLAP evolution along the gluon chain is neutralized. This allows us to search for BFKL effects. Another consequence of the requirement $k_{jT}^2 \simeq Q^2$ is that for not too small values of Q^2 we avoid a penetration of the infrared region which can originate from the diffusion in $\ln k_T^2$ which accompanies BFKL evolution to smaller values of x/x_j. To study the $(x/x_j)^{-\lambda}$ behaviour as $x/x_j \to 0$ we of course concentrate on

the region where x is as small as experimentally feasible while demanding that x_j is large, typically $x_j > 0.05$. This on the other hand means that when we calculate the differential structure functions from (3.7) we only have to input parton distributions at values of x_j where they are well-known from the global analyses. So effectively we are studying deep inelastic scattering off a known parton rather than off the proton.

After explaining the idea behind the DIS + forward jet measurement we outlined the calculation of the cross section for this process from BFKL dynamics. We also discussed the experimental cuts due to the detector geometry and the event selection. As we saw, the most severe restriction comes from the cut on the angle between the jet and the proton, $\theta_{jp} > 5°$, which is necessary in order to avoid the jet being lost in the beam pipe or mingling with the proton remnants. From Fig. 3.10 it became obvious that if the jet carries a large fraction x_j of the proton's longitudinal momentum it is emitted at small angles θ_{jp} with respect to the proton beam in the HERA frame. For a given θ_{jp} larger values of x_j can be reached by observing jets with larger k_{jT}^2 but at a depleted event rate.

So from the theoretical point of view the deep inelastic + jet measurement is an excellent way of studying BFKL dynamics. Unfortunately it turns out that in the experiment it is very difficult to identify a jet which is, as we found, very close to the proton remnant and to accurately determine its kinematic variables. Nevertheless there are encouraging results [54 – 57] as we will see in Chapter 6.

Chapter 4

Deep inelastic events containing a forward photon as a probe of small x dynamics

4.1 An alternative to the DIS + forward jet measurement

In Chapter 3 we introduced the idea of studying deep inelastic events which contain an identified forward jet as a way of identifying the underlying dynamics in small x deep inelastic scattering at HERA. The process is illustrated again in Fig. 4.1(a). We pointed out the advantages of this process from the theoretical point of view. However, we also found that the clean identification and kinematic measurement of the forward jet poses a severe experimental challenge, particularly for jets at the smaller values of k_{jT}^2 where the DIS + jet events are more numerous.

Because of the experimental difficulties with the DIS + forward jet process we now want to find out if there is a measurement which from the theoretical point of view is equally suitable for investigating the underlying dynamics at HERA but experimentally less problematic. Therefore, in this chapter we will study a related, but alternative process, namely deep-inelastic events containing an identified forward photon, see Fig. 4.1(b). As a probe of small x dynamics, the process DIS + γ has both advantages and disadvantages

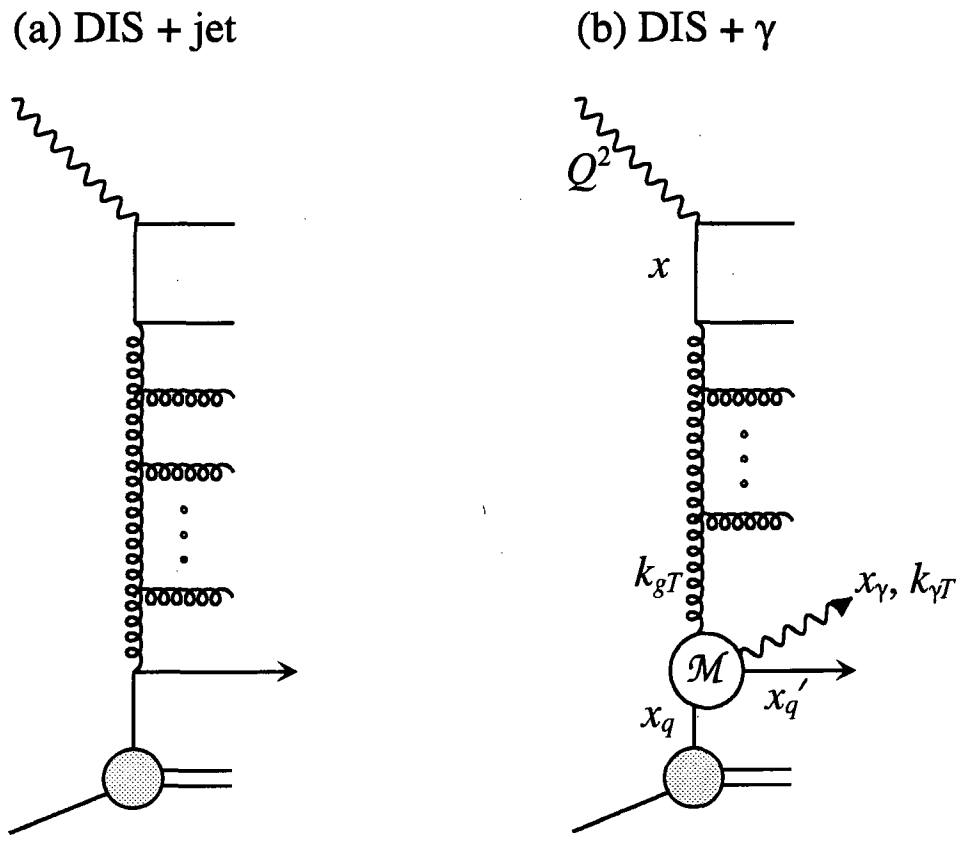

Figure 4.1: Diagrammatic representation of (a) a deep-inelastic + forward jet event, and (b) a deep-inelastic (x, Q^2) + forward identified photon $(x_\gamma, k_{\gamma T})$ event.

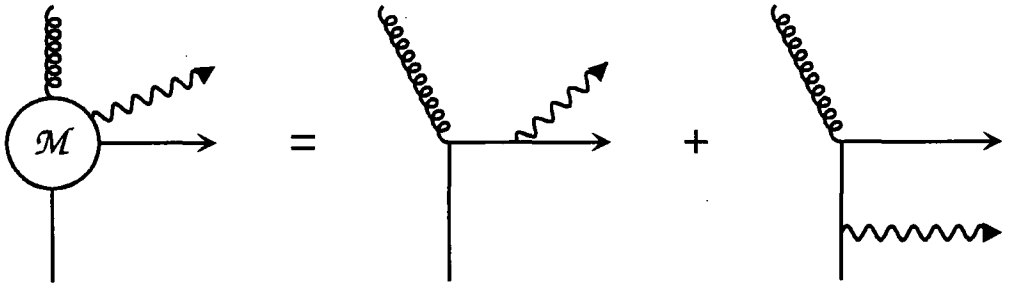

Figure 4.2: The Feynman diagrams describing the $gq \rightarrow \gamma q$ subprocess embodied in the DIS + γ diagram shown in Fig. 4.1(b).

as compared to DIS + jet. A major advantage is that the measurement of a photon should be cleaner than that of a jet, and less ambiguous, particularly at the lower values of k_T. Moreover since the q or $\overline{q}$ jet (denoted x'_q in Fig. 4.1(b)) is not identified we can enlarge the data sample by including events in which its constituents mingle with the proton remnants. On the other hand we expect the DIS + γ rate to be suppressed by a factor of order $\alpha/2\pi$ relative to DIS + jet, though this is offset since the photon is easier to measure than the jet and the recoiling quark jet is not identified. A second disadvantage is that we require isolation of the photon so as to avoid events where it arises from the decay of a parent π^0 as we will see later.

Let us now first introduce the QCD formalism for the DIS + photon process. After that we will discuss the cuts for the DIS + γ event selection and then proceed to give some predictions for the cross section.

4.2 Basic QCD formula for the DIS + photon process

We now study prompt photon production in deep-inelastic scattering at small x. That is the process

$$\text{“}\gamma\text{”} + p \rightarrow \gamma(x_\gamma, k_{\gamma T}) + X, \tag{4.1}$$

sketched in Fig. 4.1(b), in which the photon which carries a fraction x_γ of the proton's longitudinal momentum and transverse momentum $k_{\gamma T}$ is identified in the final state. We select deep inelastic events with small x and large x_γ. These events offer an opportunity to identify the effects of the BFKL resummation of the $\alpha_S \ln(x_q/x)$ contributions, which arise from the sum over the real and virtual gluon emissions, such as the one depicted in Fig. 4.1(b). In analogy to the DIS + jet process, the advantage of process (4.1) is that the outgoing photon acts as a trigger to select events in which the deep inelastic scattering occurs off a quark in a kinematic region where its distribution, $q(x_q, k^2_{\gamma T})$, is known.

4.2.1 Calculation of the matrix element for the subprocess

Let us first concentrate on the subprocess $q(k_q) + g^*(k_g) \rightarrow q(k'_q) + \gamma(k_\gamma)$ (and also $\overline{q}g^* \rightarrow \overline{q}\gamma$) which is described by the two Feynman diagrams shown in Fig. 4.2. When calculating the matrix element squared for this process we have to take into account that the incoming gluon is virtual. To ensure that we get the correct polarisation for the virtual gluon we assume that it couples to a scalar particle. The Feynman rules then imply that we have to contract the matrix element for the process $q(k_q) + g(k_g) \rightarrow q(k'_q) + \gamma(k_\gamma)$ with the four momentum r of the scalar particle. Next we keep the leading term in the high energy limit, that is the term proportional to $(k_q + r)^2$. The coefficient corresponds to the matrix element for our subprocess. Proceeding in this way we find the spin averaged matrix element squared

$$|\mathcal{M}|^2 \sim \frac{\alpha_S(k^2_{\gamma T})}{2\pi} \frac{\alpha}{2\pi} \frac{k^2_{gT}[1 + (1 - z_\gamma)^2]}{\hat{s}(-\hat{u})} \tag{4.2}$$

where the invariants $\hat{s}$ and $\hat{u}$ are

$$\hat{s} = (k_\gamma + k'_q)^2, \quad \hat{u} = (k_q - k_\gamma)^2, \tag{4.3}$$

and the variable z_γ is given by

$$z_\gamma = \frac{x_\gamma}{x_q}. \tag{4.4}$$

The fractional momenta x_i are defined by the Sudakov decomposition of the particle 4-momenta

$$k_i = x_i p' + \beta_i q' + \boldsymbol{k}_{iT} \tag{4.5}$$

for $i = \gamma$ or the outgoing quark q'. At high energies p' and q' are to a good approximation the light-like 4-momenta associated with the incoming proton and virtual photon respectively,

$$p' \equiv p - \frac{M_P^2}{2p.q} q, \quad q' \equiv q + xp, \tag{4.6}$$

where M_P is the mass of the proton. We fix the normalisation of the matrix element squared (4.2) by comparing with Altarelli-Parisi evolution and find

$$|\mathcal{M}|^2 = 2\, C_2(F) \frac{\alpha_S(k^2_{\gamma T})}{2\pi} \frac{\alpha}{2\pi} \frac{k^2_{gT}[1 + (1 - z_\gamma)^2]}{\hat{s}(-\hat{u})} \tag{4.7}$$

where the colour factor $C_2(F) = 4/3$. Note that $|\mathcal{M}|^2$ is singular for $\hat{s} \to 0$. We will deal with this problem later.

4.2.2 The differential structure function for the DIS + γ process

Having calculated the matrix element $\mathcal{M}$ for the $q(k_q) + g(k_g) \to q(k'_q) + \gamma(k_\gamma)$ subprocess we can now write down an expression for the differential structure function for deep inelastic scattering accompanied by a forward photon:

$$\frac{\partial^2 F_i}{\partial x_\gamma \partial k^2_{\gamma T}} = \int \frac{d^2 k_{gT}}{\pi k^4_{gT}} \int \frac{dx_q}{x_q} \Phi_i \left(\frac{x}{x_q}, k^2_{gT}, Q^2 \right) \sum_q e_q^2 \left[q(x_q, k^2_{\gamma T}) + \overline{q}(x_q, k^2_{\gamma T}) \right] \frac{|\mathcal{M}|^2}{z_\gamma z'_q} \tag{4.8}$$

for $i = T, L$. The variables are indicated in Fig. 4.1(b). We will specify the region of integration in (4.8) later. Recall that the matrix element squared $|\mathcal{M}|^2$ is given by (4.7). The fractional momenta x_i were defined in (4.5) and z_γ in (4.4), in general

$$z_i = \frac{x_i}{x_q}. \tag{4.9}$$

The factors z_γ and z'_q in (4.8) arise from requiring that the final state particles, i.e. the photon and the quark q' are on their mass shell. Note that the quark and antiquark distributions in (4.8) are to be evaluated at x_q which is large because we select events with large x_γ. This means that, as for the DIS + jet measurement, we only have to input parton distributions where they are well-known.

The functions $\Phi_i(z, k_T^2, Q^2)$ $(i = T, L)$ in (4.8) describe the gluon ladder which couples to the incoming virtual photon. They are the same functions Φ_i which we already introduced in Section 3.2 for the DIS + forward jet process. Recall that they correspond to the sum of ladder diagrams shown in Fig. 3.4. The Φ_i can be obtained by solving the BFKL equations (3.11). Again we impose the boundary condition that at some starting value $z = z_0$ we only have the quark box (and "crossed box") $\Phi_i^{(0)}$ and no gluon radiation. Then we apply the BFKL equations (3.11) to evolve down to smaller values of z. We use the functions $\Phi_i^{(0)}$ as given in (3.22) and (3.23) assuming three flavours of massless quarks, that is we set $m_q = 0$. As for the DIS + jet process we follow the procedure outlined in

Section 3.2.3, that is we solve the BFKL equations (3.38) numerically for the functions H_i defined in (3.37) subject to the boundary condition (3.39) and allowing the coupling α_S to run. Here we set the cut-off $k_0^2 = 1$ GeV^2 in (3.38). The "starting point" of BFKL evolution $z_0 = 0.1$ in (3.39) and correspondingly we require

$$\frac{x}{x_q} < 0.1 \tag{4.10}$$

in the x_q integration in (4.8). Of course, the integration is also subject to the kinematic constraint $x_q > x_\gamma$.

We are now in a position to calculate the differential structure function $\partial F_2/\partial x_\gamma \partial k_{\gamma T}^2$ from (4.8) where $F_2 = F_T + F_L$. Our aim is to find a signature of the BFKL resummation of the leading $\ln(x_q/x)$ terms. Therefore we do the following: we compute the differential structure function first using $\Phi_2 = \Phi_T + \Phi_L$ obtained from solving the BFKL equations (3.11). Then we repeat the calculation using for Φ_2 just the driving (quark box) term $\Phi_2^{(0)}$ which means we neglect BFKL evolution. Therefore, the difference between the two calculations is a measure of the effect of the BFKL resummation of soft gluon emissions. Let us for the moment regulate the matrix element squared $|\mathcal{M}|^2$ by simply requiring that $\hat{s} > 1$ GeV^2. Furthermore, the lower limit on the k_{gT}^2 integration in (4.8) is $k_{gT}^2 > 1$ GeV^2. The result for the F_2 differential structure function is shown in Fig. 4.3 as a function of x_γ for three different values of x. We see that the difference between the BFKL and quark box results is dramatic once x is sufficiently small ($x \lesssim 10^{-3}$) and provided $x_\gamma \sim 0.1$. Indeed we require x/x_γ to be small for the formalism to be valid. Fig. 4.3 also shows the strong increase of $\partial F_2/\partial x_\gamma \partial k_{\gamma T}^2$ with decreasing x for fixed x_γ which we expect from BFKL dynamics. In fact, as we already explained for the DIS + jet process in Section 3.2.4, it is this shape in x which we should study as a signature of BFKL effects. The shape of $\partial F_i/\partial x_\gamma \partial k_{\gamma T}^2$ is the more reliable discriminator of the underlying dynamics at small x than the magnitude, since the normalization of the QCD predictions is subject to uncertainties arising mainly from the regions of low transverse momenta (see also ref. [48]).

Fig. 4.3 for the differential structure function for DIS + γ events should be compared with Fig. 3.6 for DIS + jet events. We see that the differential structure function and therefore also the cross section is about a factor of 1000 lower for the photon process, as

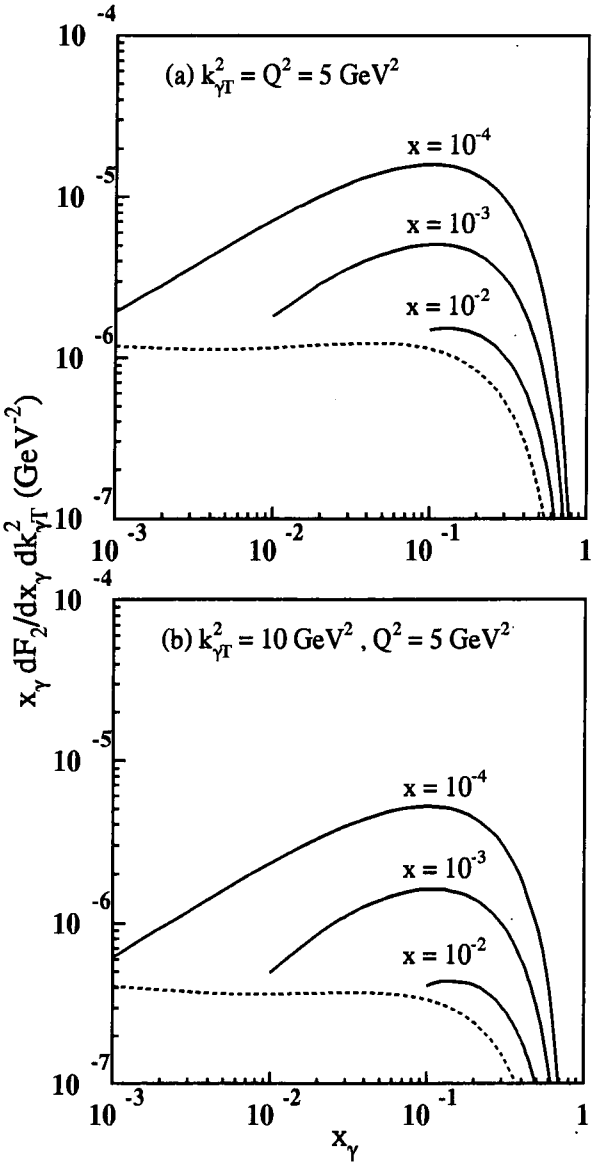

Figure 4.3: The F_2 differential structure function, (4.8), for deep-inelastic (x, Q^2) events accompanied by a measured forward photon $(x_\gamma, k^2_{\gamma T})$ as a function of x_γ for different values of x, $x = 10^{-4}, 10^{-3}$ and 10^{-2}, and for $Q^2 = 5$ GeV^2. The continuous curves correspond to inputting into (4.8) the solution Φ_2 of the BFKL equation (3.11), whereas the dashed curve is calculated using for Φ_2 simply the driving term $\Phi_2^{(0)}$ of (3.22) and (3.23). Here $|\mathcal{M}|^2$ is regulated by requiring $\hat{s} > 1$ GeV^2. Plots (a) and (b) correspond to photons with $k^2_{\gamma T} = 5$ and 10 GeV^2 respectively.

could be anticipated from the presence of the extra $\alpha/2\pi$ coupling of the photon. Note also that the DIS + γ differential structure function calculated using $\Phi_2 = \Phi_2^{(0)}$ is independent of x (until we reach the kinematic limit $\beta_\gamma = 1$), and its shape in x_γ reflects the quark and antiquark distributions in the proton after integration over x_q. In contrast, for DIS + jet the x_j shape of the box contribution is dominated by the gluon distribution $x_j g(x_j, k_{jT}^2)$, that is the gluon is sampled "locally".

In the next section we will impose reasonable experimental cuts on the outgoing photon, and then we will quantify the event rate which may be observed at HERA.

4.3 Cuts to select the DIS + forward photon events

When calculating the cross section for the DIS + forward photon process which we expect at HERA we have to impose several cuts. First of all there are the cuts defining the HERA electron acceptance region which we have already introduced and explained in detail in Section 3.3.1. As for the DIS + jet measurement we will be using

$$\begin{aligned} 0.1 < y < 0.9 \\ 8^\circ < \theta'_{ep} < 172^\circ \\ E'_e > 5 \text{ GeV} \end{aligned} \tag{4.11}$$

where y is the rapidity and E'_e the energy of the outgoing electron (or positron). θ'_{ep} is the angle of this electron with respect to the proton direction in the HERA laboratory frame where we take the energies of the incoming electron and the proton to be $E_e = 30$ GeV and $E_p = 820$ GeV respectively. In addition to the HERA requirements (4.11) on the outgoing electron there are cuts specific to the DIS + γ measurement as we will see in the following. The variables which we will be using are defined in Fig. 4.4.

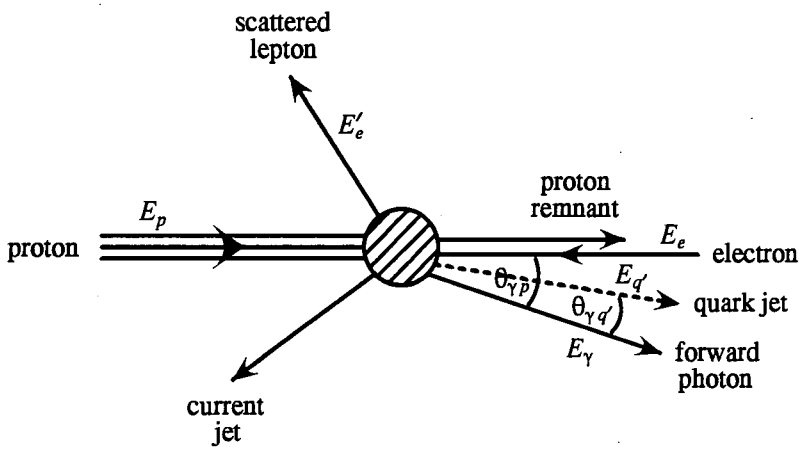

Figure 4.4: Kinematics of the deep inelastic + forward photon process.

4.3.1 The isolation cut

We are interested in semi-inclusive deep inelastic events in which only the photon is measured in the final state, besides the scattered electron. On the other hand the integrals defining the differential structure functions, (4.8), contain a potential singularity at $\hat{s} = 0$ which has to be regularized by a suitably chosen cut-off. In the calculation of the differential structure function shown in Fig. 4.3 we simply required $\hat{s} > 1$ GeV^2. However, a straightforward limitation of the region of integration to $\hat{s} > s_0$, where s_0 is some arbitrarily chosen value, does not allow for making a direct comparison of (4.8) with experiment. The reason for that is that $\hat{s}$ is only determined if the recoil quark jet q' is detected as well as the photon, whereas the idea behind the DIS + photon measurement was that the quark jet does not have to be identified.

There is a straightforward solution of this problem. If we express the four-momenta of the recoil quark jet and the photon in the HERA laboratory frame by

$$p'_q = (E'_q, \boldsymbol{p}'_q), \quad p_\gamma = (E_\gamma, \boldsymbol{p}_\gamma) \tag{4.12}$$

respectively, we can rewrite $\hat{s}$ in the following way:

$$\begin{aligned} \hat{s} &= (p_\gamma + p'_q)^2 \\ &= 2\,(E_\gamma E'_q - \boldsymbol{p}_\gamma \boldsymbol{p}'_q). \end{aligned} \tag{4.13}$$

Since the photon and the jet are on-shell we have

$$\hat{s} = 2E_\gamma E'_q\,(1 - \cos\theta_{\gamma q'}) \tag{4.14}$$

where $\theta_{\gamma q'}$ is the angle between the photon and the quark jet in the HERA laboratory frame, see Fig. 4.4. So if we were to impose a cut on $\theta_{\gamma q'}$ we would automatically regularize the singularity for $\hat{s} = 0$. Now we have to require isolation of the outgoing photon anyway to distinguish it from background photons which arise from the decay of π^0's ($\pi^0 \to \gamma\gamma$) produced either from the proton remnants or the outgoing quark jet q'. Suppose we impose an isolation angle θ_0 (where θ_0 is chosen to be around, say, 3°–10°) defining a cone around the photon, then at the parton level we have

$$\theta_{\gamma q'} > \theta_0 \tag{4.15}$$

and hence a corresponding lower limit on $\hat{s}$ from (4.14).

4.3.2 The hemisphere cut

A second requirement is that our photon should be emitted in the proton hemisphere in the virtual photon – proton centre-of-mass frame to avoid contamination from photons radiated from the quark-antiquark pair which forms the quark box (and fragments into the current jet shown in Fig. 4.4). Thus we require

$$x_\gamma > \beta_\gamma. \tag{4.16}$$

Since the four-momentum k_γ of the photon defined in (4.5) satisfies the on-mass-shell condition $k_\gamma^2 = 0$ we have

$$\beta_\gamma = \frac{x}{x_\gamma}\,\frac{k_{\gamma T}^2}{Q^2} \tag{4.17}$$

giving

$$x_\gamma > \sqrt{x k_{\gamma T}^2 / Q^2}. \tag{4.18}$$

The hemisphere cut, when combined with the kinematic constraint $x_q > x_\gamma$, imposes an implicit lower limit of the x_q integration in (4.8)

$$x_q > x_\gamma > \sqrt{x k_{\gamma T}^2 / Q^2}. \tag{4.19}$$

We see that this limit is generally stronger than our BFKL requirement (4.10) that $x_q > 10x$.

4.3.3 The beam pipe cut

Finally there is the practical limitation that photons can only be measured if they are emitted at sufficiently large angles to the proton beam direction in the HERA laboratory frame, say

$$\theta_{\gamma p} > \overline{\theta}_0. \tag{4.20}$$

(For the definition of $\theta_{\gamma p}$ see Fig. 4.4.) This cut is analogous to the beam pipe cut for the DIS + forward jet process which we introduced in Section 3.3.2. It ensures that the photon does not mingle with the proton remnants and that it is not lost in the proton beam pipe. Of course, $\overline{\theta}_0$ also depends on the detector architecture at HERA.

In Section 3.3.2 we derived a relation between the jet kinematic variables for the forward jet, eq. (3.57). If we proceed in the same way, replacing the jet variables by the photon variables, we obtain a relation between the kinematic variables of the photon,

$$x_\gamma^2 = \frac{x}{Q^2}\left[\frac{k_{\gamma T}^2 \left(E_e - E_e' + \tilde{E}\right)}{E_p \left(1 - \cos\theta_{\gamma p}\right)} + x k_{\gamma T}^2\right] \tag{4.21}$$

where the energies are defined in Fig. 4.4 and

$$\tilde{E} = E_e \cos\theta_{\gamma p} - x_e' \sin\theta_{\gamma p} \cos\phi_{\gamma p} - y_e' \sin\theta_{\gamma p} \sin\phi_{\gamma p} - z_e' \cos\theta_{\gamma p} \tag{4.22}$$

in analogy to (3.56). We can now use (4.21) to compute the *upper* boundary of the allowed regions in the kinematic variables $(x_\gamma, k_{\gamma T}^2)$ for various choices of $\overline{\theta}_0$. The azimuthal angle

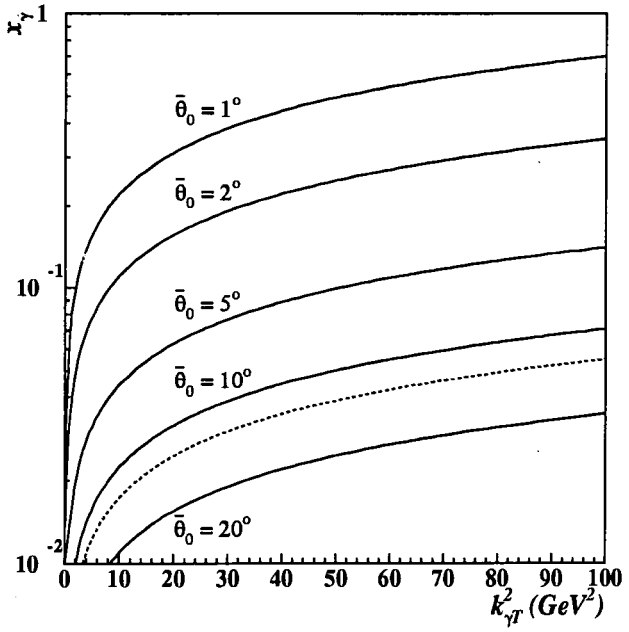

Figure 4.5: The curves give the *upper* boundary of the allowed regions of the photon kinematic variables $(x_\gamma, k^2_{\gamma T})$ for deep-inelastic + photon events with $x = 6 \times 10^{-4}$ and $Q^2 = 20$ GeV^2 for various choices of the acceptance angle $\overline{\theta}_0$ of (4.20). The photon angle $\theta_{\gamma p}$ to the proton direction in the HERA (30 x 820 GeV) laboratory frame is not uniquely specified by $(x, Q^2; x_\gamma, k^2_{\gamma T})$. Varying the remaining azimuthal angle transforms the lines of constant $\theta_{\gamma p}$ into narrow bands in the $x_\gamma, k^2_{\gamma T}$ plane. The continuous lines that are shown are obtained by averaging over the azimuthal degree of freedom. The lines are insensitive to reasonable variations of x and Q^2. Also shown (by a dashed line) is the *lower* boundary given by the hemisphere cut (4.18) for $x = 6 \times 10^{-4}$ and $Q^2 = 20$ GeV^2.

$\phi_{\gamma p}$ in (4.22) is not fixed by $(x, Q^2; x_\gamma, k^2_{\gamma T})$ which means we have to average over all possible azimuthal angles. The result is displayed in Fig. 4.5 for $x = 6 \times 10^{-4}$ and $Q^2 = 20\text{GeV}^2$. Actually the boundaries are insensitive to reasonable variations of x and Q^2. From Fig. 4.5 it becomes clear that large x_γ photons are only emitted at small angles $\theta_{\gamma p}$ between the photon and the proton. For a given $\theta_{\gamma p}$ we can reach larger x_γ by observing photons with large $k^2_{\gamma T}$, but then the event rate is depleted. We also indicate in Fig. 4.5 the "forward hemisphere" *lower* boundary, (4.18), for $x = 6 \times 10^{-4}$ and $Q^2 = 20$ GeV^2.

4.4 Predictions for DIS + photon production

We will now present numerical predictions for the cross section for the production of an energetic photon in deep inelastic ep scattering at HERA taking into account the various cuts discussed in the previous section. The relevant cross section is given by the formula

$$\frac{d\sigma}{dx_\gamma dk_{\gamma T}^2 dx dQ^2} = \frac{4\pi\alpha^2}{xQ^4}\left[(1-y)\frac{dF_2}{dx_\gamma dk_{\gamma T}^2} + \frac{y^2}{2}\frac{dF_T}{dx_\gamma dk_{\gamma T}^2}\right] \tag{4.23}$$

where $y = Q^2/xs$ with s the centre of mass energy squared. For $dF_{2,T}/dx_\gamma dk_{\gamma T}^2$ we substitute the differential structure functions (4.8) using the relation $F_2 = F_T + F_L$.

4.4.1 Dependence of the DIS + photon cross section on the cuts

In Section 4.3 we discussed several cuts which have to be imposed in the calculation of the DIS + photon cross section. Now it is time to decide on reasonable values for these cuts.

To obtain the total cross section in some bin in x and Q^2 we have to integrate the differential cross section (4.8) over x_γ, $k_{\gamma T}^2$, x and Q^2. The limits on the x and Q^2 integrations of course depend on the given bin subject to the requirements (4.11) on the outgoing electron. The "forward hemisphere" boundary acts as a lower limit on the x_γ integration which we will from now on always impose. As we will see we have to also introduce a minimum transverse momentum squared k_{th}^2 of the photon in the $k_{\gamma T}^2$ integration.

Limiting the integrations in this way we can investigate the dependence of the total cross section for DIS + photon events on the angle θ_0 which defines the isolation cone around the forward photon, see eq. (4.15). In Fig. 4.6(a) we show the effect of varying θ_0 on the total cross section in the (x, Q^2) bin defined by $6 \times 10^{-4} < x < 8 \times 10^{-4}$ and $20 < Q^2 < 30$ GeV^2. Here we required that $k_{\gamma T}^2 > 5$ GeV^2 and that the photon is emitted at an angle $\theta_{\gamma p} > 5°$ with respect to the proton beam direction. As in Fig. 4.3 we display the results when including BFKL evolution in the calculation and when using only the

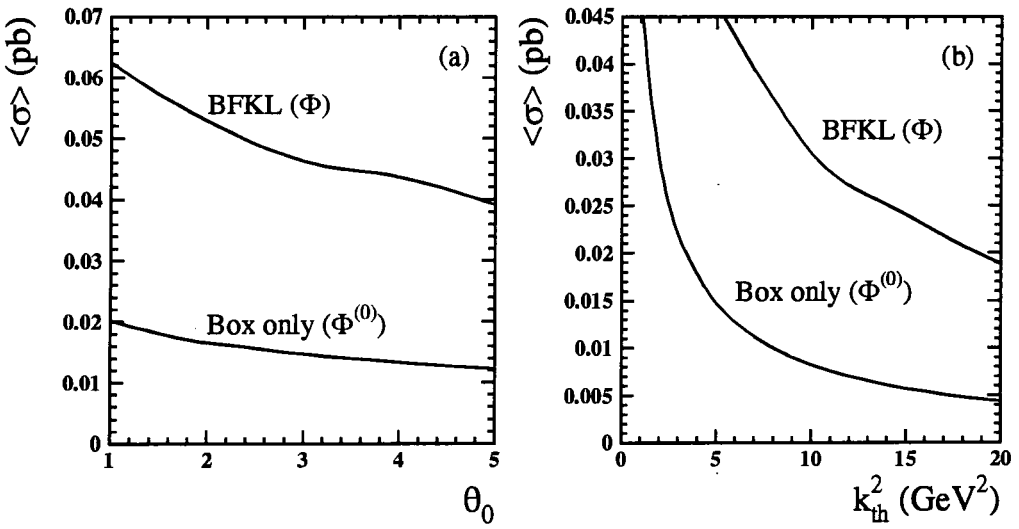

Figure 4.6: The dependence of the DIS + γ cross section integrated over the photon variables to variation of (a) the angle θ_0 defining the isolation cone around the photon ($\theta_{\gamma j} > \theta_0$) and (b) the threshold for photon detection ($k^2_{\gamma T} > k^2_{th}$). The results are for the x, Q^2 bin defined by $6 \times 10^{-4} < x < 8 \times 10^{-4}$ and $20 < Q^2 < 30$ GeV^2. We impose the hemisphere cut (4.19) and take $\overline{\theta}_0 = 5°$ in (4.20). (The lack of smoothness of the curves simply reflects the errors on the six-fold numerical integration).

driving term $\Phi^{(0)}$. We see that in both cases the dependence on the isolation cone angle is relatively weak. This is of advantage because it means that we can choose a reasonably large θ_0 without losing many events. Let us next fix $\theta_0 = 3°$ and study the dependence of the cross section on k^2_{th} in the same kinematic region. While acting as a lower limit on the $k^2_{\gamma T}$ integration of (4.23), k^2_{th} is also important physically because it is the minimum transverse momentum squared which allows the identification of the forward photon in the HERA detectors. Fig. 4.6(b) shows the variation of the DIS + photon cross section with k^2_{th} again when including BFKL resummation in the calculation and when neglecting it ("box only"). We notice that it would be useful if photons with very small $k^2_{\gamma T}$ could be identified in the experiment. For the predictions which will be given in the next subsection we will choose $k^2_{\gamma T} > 5$ GeV^2.

In Table 4.1 we show the effect on the DIS + γ cross section in the $6 \times 10^{-4} < x < 8 \times 10^{-4}$ and $20 < Q^2 < 30$ GeV^2 bin of varying $\overline{\theta}_0$ (the minimum angle to the proton beam) and θ_0 (the half-angle of the isolation cone). The remaining cuts are the same as for Fig. 4.6(a). We see that the event rate is less sensitive to the cone angle θ_0 than to

Table 4.1: The DIS + γ cross section in the bin $6 \times 10^{-4} < x < 8 \times 10^{-4}$, $20 < Q^2 < 30$ GeV^2 as calculated for Fig. 4.6(a), but for different choices of $\overline{\theta}_0$ and θ_0.

$\overline{\theta}_0$	θ_0	$\Delta\sigma$ (fb)
5°	3°	46.2
7°	3°	29.1
7°	5°	26.2

the minimum angle $\overline{\theta}_0$ to the beam. For the predictions shown in the following section we will use $\theta_0 = 3°$ and $\overline{\theta}_0 = 5°$.

4.4.2 The DIS + photon cross section

Having discussed in detail the cuts on the DIS + γ events we can now proceed to presenting some predictions for the cross section for these events. Let us summarise which cuts we imposed in the cross section calculation:

- the electron acceptance region specified in (4.11)
- the hemisphere cut (4.18)
- $\theta_{\gamma j} > \theta_0 = 3°$
- $\theta_{\gamma p} > \overline{\theta}_0 = 5°$
- $k^2_{\gamma T} > k^2_{th} = 5$ GeV^2.

In Fig. 4.7 we show the integrated cross section for prompt forward photon production as a function of x for three different Q^2 bins: 20-30, 30-40 and 40-50 GeV^2 respectively. We compare the predictions for the case where the BFKL small x resummation is incorporated with those where the gluon radiation is neglected. The x dependence of the cross section is driven by the small z behaviour of the Φ_i. The results show a strong enhanced increase with decreasing x which is characteristic of the effect of soft gluon resummation. At $x \approx 10^{-4}$ the cross section is about a factor of 3.5 larger than that in which the BFKL

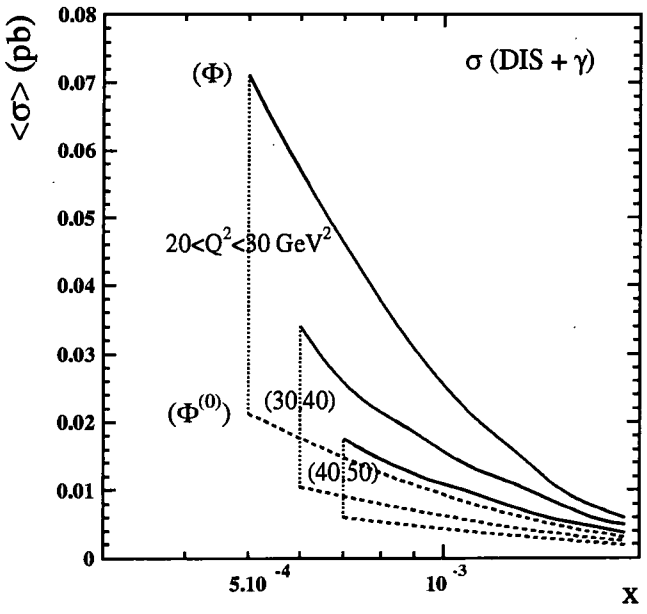

Figure 4.7: The cross section, $\langle\sigma\rangle$ in pb, for deep inelastic + photon events integrated over $\Delta x = 2\times10^{-4}$, $\Delta Q^2 = 10$ GeV^2 bins which are accessible at HERA, and integrated over the region $\theta_{\gamma p} > 5°, k^2_{\gamma T} > 5$ GeV^2, but subject to (4.19) and an isolation cut of $\theta_0 = 3°$. The x dependence is shown for three different ΔQ^2 bins, namely (20,30), (30,40) and (40,50) GeV^2. The $\langle\sigma\rangle$ values are plotted at the central x value in each Δx bin and joined by straight lines. The continuous curves show $\langle\sigma\rangle$ calculated with Φ_i determined from the BFKL equation, whereas the dashed curves are obtained just from the driving terms $\Phi_i^{(0)}$, i.e. from the quark box. For clarity a vertical line links the pair of curves belonging to the same ΔQ^2 bin.

effects are neglected. Since the impact factors, $\Phi_i^{(0)}$, are independent of x, the weak x dependence in the latter case arises mainly from acceptance. Let us emphasize here that it is in fact the shape in x of the cross section which we should focus on when searching for BFKL effects. As we explained in Section 3.2.4 the x-dependence is less affected by the lower limit cutoffs on the transverse momentum integrations than the normalisation. Finally, in Fig. 4.8, we show the cross section in the various deep inelastic (x, Q^2) bins. The values are shown in fb and so would correspond to the number of events for an eventual integrated luminosity of 1 fb^{-1}.

The DIS + γ cross sections presented in Figs. 4.7 and 4.8 may be compared directly with the values for the DIS + jet process shown in Fig. 4 of ref. [47] and Fig. 8 of ref. [49] respectively. We see that there is a suppression of about a factor of 400 in going from the DIS + jet to the DIS + γ process. Of course the ratio depends on the precise cuts that

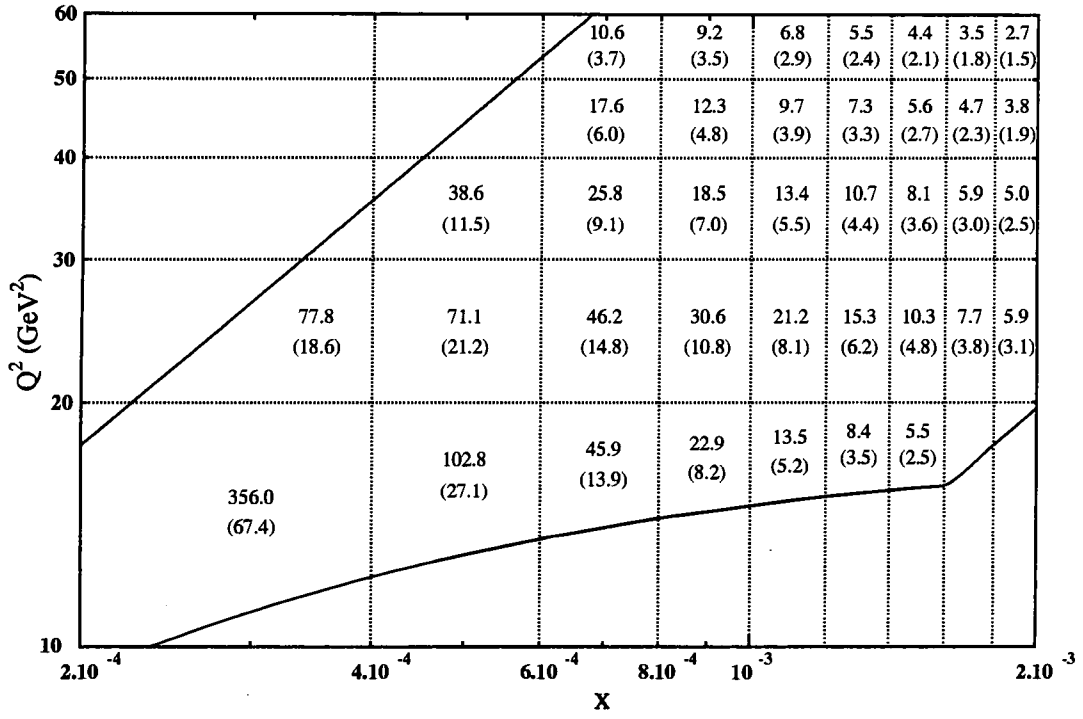

Figure 4.8: The cross section $\langle\sigma\rangle$ in fb for deep inelastic + photon events in various $(\Delta x, \Delta Q^2)$ bins which are accessible at HERA, and integrated over the region $\theta_{\gamma p} > 5°, k^2_{\gamma T} > 5$ GeV^2, but subject to (4.19) and an isolation cut of $\theta_0 = 3°$. The number in brackets is the cross section calculated with just the quark box approximation ($\Phi_i = \Phi_i^{(0)}$). The difference between the two numbers is therefore the enhancement due to the BFKL soft gluon resummation. The solid curves represent the electron acceptance region defined by (4.11).

are imposed in each case, see for example Table 4.1.

4.5 Discussion

As explained in Chapter 3 the DIS + jet process is, in principle, an ideal way to probe small x dynamics, *provided* sufficiently forward jets can be measured. In practice to separate cleanly such forward jets from the proton remnants is a formidable challenge. In this chapter we studied the analogous DIS + γ process which has the advantage that forward photons can be more reliably measured than forward jets, but for which the event rate is considerably suppressed. In Section 4.4.2 we quantified the suppression. There we

predicted the DIS + γ cross section using BFKL dynamics and found a characteristic rise with decreasing x, which becomes steeper the more forward the detected photons are.

Our study should be regarded as an exploratory investigation of the potential usefulness of the process. The DIS + γ rates which we presented in Figs. 4.7 and 4.8 correspond to photons produced (i) at more than 5° to the proton beam direction ($\theta_{\gamma p} > \overline{\theta}_0 = 5°$) in the HERA frame, (ii) in the centre of an isolation cone of half-angle 3° ($\theta_{\gamma q'} > \theta_0 = 3°$) in the HERA frame, (iii) in the proton hemisphere in the $\gamma^* p$ centre-of-mass frame (to avoid contamination with photons radiated from the quark box), and (iv) with $k^2_{\gamma T} > 5$ GeV^2. Our work is at the parton level and so in practice the isolation criteria will need further study. In particular simulations of the fragmentation of the outgoing (q') jet should be performed so as to be able to choose the optimum isolation criteria for the photon. Recall that isolation is required to suppress background photons from π^0 decays. Since the DIS + forward cross section will in any case be quite small, in the following chapter we study another alternative to the original DIS + forward jet measurement.

Chapter 5

Forward π^0 trigger of the deep inelastic + jet probe of BFKL dynamics

In this chapter we investigate the feasibility of using the DIS + π^0 process to identify the underlying dynamics in the HERA small x region. After calculating the DIS + jet cross section in Chapter 6 we will then, in Chapter 7, return to the DIS + π^0 process. There we will explain how the normalisation of the BFKL functions Φ_i can be fixed by comparing with the H1 DIS + jet data. Then we will calculate the DIS + π^0 cross section imposing the cuts that were used by the H1 collaboration in a very recent forward π^0 measurement which was motivated by the study presented in this chapter and compare with their data.

5.1 Proposal of the DIS + forward π^0 measurement

In Chapter 3 we studied deep inelastic (x, Q^2) events containing an identified forward jet (x_j, k_{jT}^2) as a probe of the small x behaviour of QCD, see Fig. 5.1(a). We pointed out that the observation of DIS + jet events offers the opportunity to expose BFKL-type small x dynamics free from the ambiguities associated with the choice of the non-perturbative parton input. Experimentally, however, the clean identification and kinematic measurement of a forward jet proves to be difficult since we require it to be as close to the proton

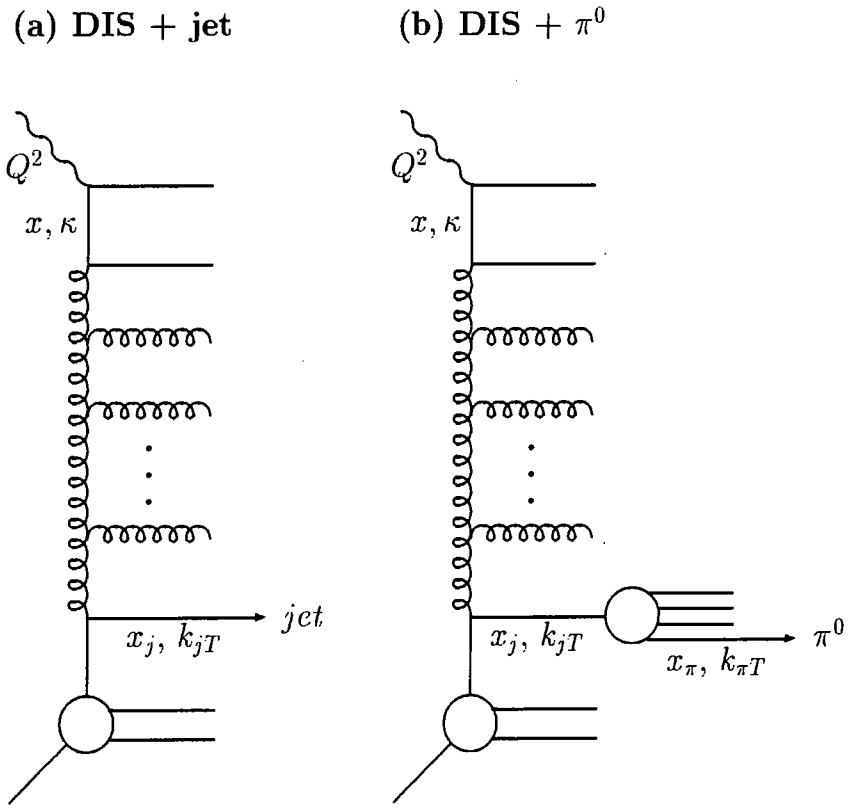

Figure 5.1: Diagrammatic representation of (a) a deep inelastic + forward jet event, and (b) a deep inelastic (x, Q^2) + identified forward π^0 $(x_\pi, k_{\pi T})$ event.

remnants as possible, that is x_j as large as possible.

Here we will use the improved knowledge of the fragmentation functions to propose that the forward jet is identified through the measurement of a single energetic decay product. As it turns out the π^0 is the hadron which can be identified in the most forward direction in the detectors at HERA. We use the BFKL formalism to predict the DIS + forward π^0 rate. The rate will, of course, be suppressed in comparison with the DIS + forward jet rate and it is an experimental issue to see if the advantages of single particle detection as compared to identification of the (parent) jet can compensate for the loss of signal. (See, however, the updated discussion in Chapter 7.)

Before displaying the formalism for the calculation of the DIS + π^0 cross section in Section 5.3 we will, in the following section, outline the fragmentation functions approach

to hadronisation. Then in Section 5.4 we introduce the experimental cuts which we impose and give our numerical predictions for the DIS + π^0 process in Section 5.5. The final section of the chapter contains a discussion.

5.2 Fragmentation functions

So far, in this thesis we have only presented calculations which were on the *parton* level. In the DIS + π^0 measurement, however, we are triggering on a *hadron*, the π^0, in the final state. Therefore, we need a formalism for describing how partons turn into hadrons. However, when we try to establish a QCD description of the hadronisation process we encounter the following problem: Whereas the partons produced in the scattering process are emitted at short distances, hadronisation takes place at larger distances. This means that the coupling α_S may be large and perturbation theory not applicable. The solution is provided by the factorization theorem which enables us to express cross sections as products of factors which each involve phenomena appearing at different energy scales. In particular we can write the cross section for a hadronic collision with inclusive production of one hadron as the convolution of the partonic hard cross section and the distribution and fragmentation functions which represent the parton density inside the hadrons and the hadron density inside the partons respectively. The fragmentation functions contain all the information on the hadronisation process. In this section we will discuss the simple parton model description of these functions and then include scaling violations. We will also outline how the fragmentation functions can be modelled phenomenologically and obtained from fits to experimental data.

5.2.1 Parton Model

Let us consider the process $AB \to hX$ which is depicted in Fig. 5.2. h is a hadron with large transverse momentum $|\boldsymbol{p}_T|$ and X represents all other particles in the final state. The incoming hadrons A and B contain amongst others the partons a and b respectively. These partons scatter and produce the partons c and d which carry a large transverse

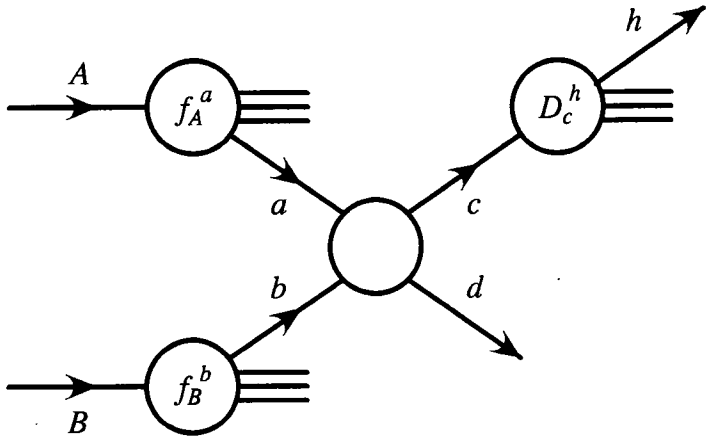

Figure 5.2: The hadronic scattering process $AB \to hX$ at large p_T in terms of the underlying partonic process $ab \to cd$, the structure functions f_A^a and f_B^b, and the fragmentation function D_c^h [58].

momentum q_T. Due to the confinement mechanism hadron h is then produced from parton c.

Now we try to estimate the cross section for the inclusive process $AB \to hX$. We define x_a as the fraction of the momentum of hadron A which parton a carries,

$$x_a = \frac{q_a}{p_A} \tag{5.1}$$

with $0 \leq x_a \leq 1$. For simplicity we neglect any components of the momentum of a that are transverse to the z-axis which we choose to lie in the beam direction. We also assume that the masses of the hadrons and partons are small compared to the momenta we are dealing with, which allows us to write

$$p_a^\mu \simeq (p_a, 0, 0, p_a) \tag{5.2}$$

and

$$q_a^\mu \simeq (q_a, 0, 0, q_a) = x_a\,(p_a, 0, 0, p_a). \tag{5.3}$$

Next we introduce the variable z_h which is the fraction of the momentum of parton c which hadron h acquires,

$$z_h = \frac{p_h}{q_c}, \tag{5.4}$$

where $0 \leq z_h \leq 1$. Then the invariant $\hat{t}$ for the partonic subprocess $ab \to cd$ is

$$\hat{t} = (q_a^\mu - q_c^\mu)^2 \simeq -2q_a \cdot q_c = -2\frac{x_a}{z_h} p_A \cdot p_h \tag{5.5}$$

If we know the differential cross sections, $d\sigma/d\hat{t}$, for all the parton subprocesses, we can calculate the parton model cross section for $AB \to hX$ from [58]

$$\begin{aligned} E_h \frac{d\sigma}{d^3p_h}(AB \to hX) &= \sum_{abcd} \int_0^1 dx_a \int_0^1 dx_b \, f_A^a(x_a) \, f_B^b(x_b) \\ &\quad \times \frac{1}{\pi z_h} \frac{d\sigma}{d\hat{t}}(ab \to cd) \, D_c^h(z_h). \end{aligned} \tag{5.6}$$

Here the parton distributions f_A^a give the probability for finding a parton a inside hadron A which carries a fraction x_a of its momentum. The functions D_c^h are the so-called *fragmentation functions* which represent the probability that a hadron h with momentum fraction z_h is found in the debris of the outgoing parton c. We assume that the hadron h is produced collinearly with c. In addition, we take the fragmentation to only be dependent on z_h and not on the nature of the initial state. This then allows us to determine the fragmentation functions from one process and use them in the calculation of the cross section of another.

Sum rules

The form of the fragmentation functions is partially determined by sum rules. To see this let us consider a process where the outgoing partons c and d in Fig. 5.2 are a quark and an antiquark (or vise versa). We notice that, first of all, the energy of all the hadrons which are fragments of a given quark must equal the initial energy of that quark, i.e.

$$\sum_h \int_0^1 dz \, z D_q^h(z) = 1. \tag{5.7}$$

Secondly, charge conservation requires that

$$\sum_h e_h \int_0^1 dz \, [D_q^h(z) - D_{\bar{q}}^h(z)] = e_q, \tag{5.8}$$

and finally probability conservation implies that the average multiplicity of hadrons of type h is given by

$$\langle n_h \rangle = \sum_{q,\bar{q}} \int_{z_{min}}^1 dz \, D_q^h(z) \tag{5.9}$$

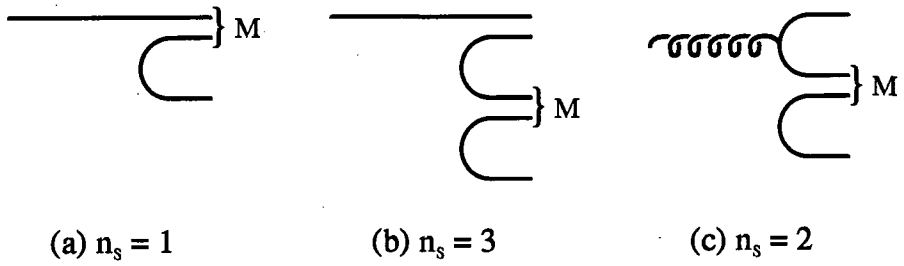

Figure 5.3: The minimum number of spectators, n_s, for fragmentation into a meson M for three different cases: fragmention of a quark or antiquark which (a) is and (b) is not a constituent of M, and (c) fragmentation of a gluon [58].

where z_{min} is the lowest possible value of z for a hadron of mass m_h.

Limiting behaviour as $z \to 0$ or 1

The fragmentation functions are not only constrained by sum rules but also by the behaviour we expect in the limits $z \to 0$ and 1. As z approaches 1 the hadron carries almost all of the parent parton's momentum. This means that any other partons which are left behind in the hadronisation can only have negligible momentum. In this case dimensional counting implies that [58]

$$D_q^h(z) \sim (1-z)^{2n_s-1} \tag{5.10}$$

for $z \to 1$. Here n_s is the minimum number of spectator partons present during the hadronisation process. In Fig. 5.3 we show schematically the fragmentation of a parton into a meson M and the corresponding value of n_s. So, for example, for the fragmentation of a gluon into a meson M we would expect that

$$D_g^M(z) \sim (1-z)^3 \tag{5.11}$$

in the limit $z \to 1$. Regge theory, on the other hand, provides a constraint on the fragmentation functions as $z \to 0$. In this case the nearly massless hadrons carry essentially none of the parton's momentum. Therefore, in analogy to what we saw for the small-x behaviour of the parton distributions in Chapter 1, Regge theory leads us to expect that

$$D_q^h(z) \sim z^{-1} \tag{5.12}$$

in the limit $z \to 0$. Expectations (5.10) and (5.12) suggest a parametrisation of the fragmentation functions of the form

$$D_q^h(z) \;=\; N_q^h \, z^{-1} \, (1-z)^{2n_s-1} \tag{5.13}$$

where the normalisation N_q^h is constained by the sum rules (5.7) and (5.8) which we discussed above. As we will see, parametrisations of a similar form are indeed used for the determination of fragmentation functions from experimental data.

5.2.2 Scaling violations

The parton model predicts a scale-independent behaviour of the fragmentation functions. However, as we also saw for the parton distributions in Section 1.4 this scaling is violated when we include QCD corrections. In the framework of the *QCD-improved* parton model the fragmentation functions not only depend on z but also on some scale μ^2, i.e. $D(z) \to D(z,\mu^2)$. Imagine this scale is increased from μ^2 to $\mu^2 + d\mu^2$. Then the resulting change in the fragmentation function D_i^h is entirely due to the splitting of a parton of type i in this scale interval. Therefore, the evolution of the fragmentation functions with μ^2 is described by DGLAP equations [18, 19],

$$\frac{\partial}{\partial \ln \mu^2} D_i^h(z,\mu^2) \;=\; \frac{\alpha_S}{2\pi} \sum_j \int_z^1 \frac{dy}{y} \, P_{ji}(y,\alpha_S) \, D_j^h\left(\frac{z}{y},\mu^2\right), \tag{5.14}$$

where the indices i and j run over all active quark and antiquark flavours and the gluon. These evolution equations look like the DGLAP equations for the parton distributions, c.f. (1.60) and (1.61), but with the splitting functions P_{ji} instead of P_{ij}. The reason is that D_j^h represents the fragmentation of the *final* parton, whereas f_j is the distribution of the *initial* parton. Note also that in fragmentation the branching is timelike rather than spacelike as in deep inelastic scattering. Only the lowest order functions $P_{ji}^{(0)}(y)$ in the perturbative expansion

$$P_{ji}(y,\alpha_S) \;=\; P_{ji}^{(0)}(y) \;+\; \frac{\alpha_S}{2\pi} P_{ji}^{(1)}(y) \;+\; \ldots \tag{5.15}$$

are the same in both cases, see Chapter 1. A summary of the functions $P_{ji}^{(1)}(y)$ can be found in ref. [17].

How do the scaling violations enter the calculation of the cross section for the process $AB \to hX$ which we above discussed in the parton model? Recall that in case of the parton distributions it was possible to sum, factor off and absorb the collinear singularities into universal running parton distributions. Similarly, here the factorisation approach enables us to absorb the collinear singularities into the fragmentation functions. Therefore we can, to leading order, include the scale dependence in the cross section formula (5.6) for the scattering $AB \to hX$ in a straightforward way. We replace the parton model parton distributions and fragmentation functions by the μ^2 dependent ones and write

$$E_h \frac{d\sigma}{d^3p_h}(AB \to hX) = \sum_{abcd} \int_0^1 dx_a \int_0^1 dx_b \, f_A^a(x_a,\mu^2)\, f_B^b(x_b,\mu^2) \times \frac{1}{\pi z_h} \frac{d\sigma}{d\hat{t}}(ab \to cd)\, D_c^h(z_h,\mu^2). \tag{5.16}$$

To obtain the cross section $d\sigma/d\hat{t}$ for the partonic subprocess $ab \to cd$ we still only have to compute the Born diagrams but replacing α_S by $\alpha_S(\mu^2)$. Later we will use an expression which has the general form of (5.16) to calculate the cross section for DIS + π^0 production from the DIS + jet cross section.

5.2.3 Determination of fragmentation functions from experiment

The DGLAP evolution equations only describe the scale dependence of the fragmentation functions. It is not possible to calculate the z-dependence from perturbative QCD. Therefore the fragmentation functions have to be obtained from experiment. The standard procedure is to parametrize the z-dependence of the fragmentation functions as

$$D(z,\mu_0^2) = N\, z^\alpha\, (1-z)^\beta \tag{5.17}$$

at some low scale μ_0^2. (Note that this form is similar to our parton model parametrisation (5.13).) The next step is to use the DGLAP equations (5.14) to evolve these "starting" z-distributions to scale μ^2. The parameters α, β and N are fixed by demanding that the evolved distributions describe the data at scale μ^2. It is therefore necessary to solve the system of integro-differential equations given by the DGLAP equations (5.14). This can

be done by applying the Mellin transform technique [20] which renders the convolutions to products. As a check, one can see if the fragmentation functions obtained in this way fulfil the sum rules (5.7), (5.8) and (5.9) (with $D(z)$ replaced by $D(z,\mu^2)$) for an arbitrary scale.

Fragmentation functions $D_i^h(z,\mu^2)$ are mainly obtained from data on the inclusive production of a hadron h in e^+e^- annihilation, i.e. from the process

$$e^+e^- \to (\gamma, Z) \to h + X. \tag{5.18}$$

Here z is defined as the energy fraction of the outgoing hadron h,

$$z = \frac{2E_h}{\sqrt{s}} \tag{5.19}$$

where $\sqrt{s}$ is the centre-of-mass energy of the collision. Determining the fragmentation functions from e^+e^- scattering has the advantage that additional uncertainties due to the parton distributions which are also derived from fits to data are avoided. In the framework of the QCD-improved parton model which we discussed above the z-dependence of the cross section of the process $e^+e^- \to h + X$ emerges from the z-dependence of the cross section of the partonic subprocess $e^+e^- \to i + X$ through convolution with the fragmentation functions $D_i^h(z,\mu^2)$. Therefore the fitting parameters in (5.17) can be fixed by requiring that after evolution the $D_i^h(z,\mu^2)$ give a differential cross section $d\sigma(e^+e^- \to i + X)/dz$ which agrees with the data. The more recent sets of fragmentation functions were determined in next-to-leading order analyses of real and Monte Carlo simulated data. Fragmentation functions for neutral and charged pions were for example derived in refs. [59] and [60, 61], respectively. An overview of various sets can be found in [62].

The fragmentation functions determined from data on e^+e^- annihilations provide an opportunity for non-trivial tests of the factorisation theorem. If factorisation holds then these fragmentation functions are universal and can be applied in the computation of cross sections for other processes. The results can then be compared with experiment. In this thesis we rely on the validity of the factorisation theorem: we will use the set of leading order fragmentation functions for charged pions given in [61] to calculate the cross

section for the DIS + π^0 process. We choose this particular set because in their analysis the authors treated the light, s, c and b quarks independently for the first time.

5.2.4 Relation between fragmentation functions for charged and neutral pions

The set of fragmentation functions provided in ref. [61] is valid for charged pions. In this chapter, however, we will be dealing with the fragmentation of a parton jet into a π^0. We therefore note that SU(2) symmetry implies that

$$D_i^{\pi^0}(z,\mu^2) \;=\; \frac{1}{2}\left[D_i^{\pi^+}(z,\mu^2) \;+\; D_i^{\pi^-}(z,\mu^2)\right] \tag{5.20}$$

for all partons $i = q, \overline{q}, g$. To see this we express the fragmentation functions in terms of contributions corresponding to the possible values of the total isospin I. In our notation I_i is the isospin and m_i the third component of the isospin for $i = q, \pi$ [7]. Since a quark or antiquark has isospin $I_q = 1/2$ and a pion $I_\pi = 1$ the total isospin can assume the values $I = 1/2, 3/2$. Then we have

$$D^{\pi(I_\pi=1,m_\pi)}_{q(I_q=\frac{1}{2},m_q)} \;=\; \sum_{I=\frac{1}{2},\frac{3}{2}} \langle I_\pi I_q m_\pi m_q | I_\pi I_q I M\rangle^2 \, D^I \tag{5.21}$$

where $M = m_\pi + m_q$ is the third component of the total isospin. The $\langle I_\pi I_q m_\pi m_q | I_\pi I_q I M\rangle$ are the so-called Clebsch-Gordon coefficients which can be found in [63]. Let us now consider the fragmentation of a u-quark into a π^0, π^+ or π^-. The corresponding fragmentation functions can be written as

$$\begin{aligned}
D_u^{\pi^0} &= \left\langle 1\,\frac{1}{2}\,0\,\frac{1}{2}\,\middle|\, 1\,\frac{1}{2}\,\frac{1}{2}\,\frac{1}{2}\right\rangle^2 D^{\frac{1}{2}} + \left\langle 1\,\frac{1}{2}\,0\,\frac{1}{2}\,\middle|\, 1\,\frac{1}{2}\,\frac{3}{2}\,\frac{1}{2}\right\rangle^2 D^{\frac{3}{2}} \\
D_u^{\pi^+} &= \left\langle 1\,\frac{1}{2}\,-1\,\frac{1}{2}\,\middle|\, 1\,\frac{1}{2}\,\frac{1}{2}\,-\frac{1}{2}\right\rangle^2 D^{\frac{1}{2}} + \left\langle 1\,\frac{1}{2}\,-1\,\frac{1}{2}\,\middle|\, 1\,\frac{1}{2}\,\frac{3}{2}\,-\frac{1}{2}\right\rangle^2 D^{\frac{3}{2}} \\
D_u^{\pi^-} &= \left\langle 1\,\frac{1}{2}\,1\,\frac{1}{2}\,\middle|\, 1\,\frac{1}{2}\,\frac{1}{2}\,\frac{3}{2}\right\rangle^2 D^{\frac{1}{2}} + \left\langle 1\,\frac{1}{2}\,1\,\frac{1}{2}\,\middle|\, 1\,\frac{1}{2}\,\frac{3}{2}\,\frac{3}{2}\right\rangle^2 D^{\frac{3}{2}}.
\end{aligned} \tag{5.22}$$

[7] Actually we consider $\overline{\pi}$ rather than π here. The reason is that we square the amplitude for the fragmentation process $q \to \pi + X$ and cross the π-meson line onto the quark side. Then we apply isospin conservation to the two-body process $\overline{\pi} + q \to \overline{\pi} + q$.

Substituting the numbers for the Clebsch-Gordon coefficients we obtain

$$\begin{aligned} D_u^{\pi^0} &= \left(-\sqrt{\frac{1}{3}}\right)^2 D^{\frac{1}{2}} + \left(\sqrt{\frac{2}{3}}\right)^2 D^{\frac{3}{2}} = \frac{1}{3} D^{\frac{1}{2}} + \frac{2}{3} D^{\frac{3}{2}} \\ D_u^{\pi^+} &= \left(-\sqrt{\frac{2}{3}}\right)^2 D^{\frac{1}{2}} + \left(\sqrt{\frac{1}{3}}\right)^2 D^{\frac{3}{2}} = \frac{2}{3} D^{\frac{1}{2}} + \frac{1}{3} D^{\frac{3}{2}} \\ D_u^{\pi^-} &= 0\, D^{\frac{1}{2}} + 1\, D^{\frac{3}{2}} = D^{\frac{3}{2}}. \end{aligned} \tag{5.23}$$

Addition yields

$$D_u^{\pi^+} + D_u^{\pi^-} = \frac{2}{3} D^{\frac{1}{2}} + \frac{4}{3} D^{\frac{3}{2}} = 2\, D_u^{\pi^0}. \tag{5.24}$$

If we take into account that

$$\begin{aligned} D_u^{\pi^0} &= D_d^{\pi^0} \\ D_u^{\pi^+} &= D_d^{\pi^-} \\ D_u^{\pi^-} &= D_d^{\pi^+} \end{aligned} \tag{5.25}$$

we find that a relation analogous to (5.24) also holds for d-quarks. Treating the remaining quarks similarly shows that (5.20) is valid. Of course, (5.20) is trivially true for gluons.

5.3 QCD formalism for the DIS + forward π^0 process

In the previous section we outlined the fragmentation functions approach to the description of the fragmentation of a jet into a hadron. Now we will use this formalism to obtain the cross section for the DIS + forward π^0 process from the DIS + jet cross section.

5.3.1 The DIS + forward jet cross section – a reminder

First we recall the derivation of the cross section for the deep inelastic + jet process depicted in Fig. 5.1(a), which also shows the variables used. The differential cross section $\partial\sigma_j/\partial x\partial Q^2$ is given by (3.6) where we substitute the differential structure functions (3.7).

When calculating these differential structure functions we have to evaluate the parton distributions at (x_j, k_{jT}^2) as we did for the DIS + jet process. Since we require the forward π^0 to carry a large fraction of the proton's longitudinal momentum ($x_\pi \gtrsim 0.05$) and since $x_j > x_\pi$, x_j is also large. Therefore we again only have to supply the parton distributions where they are well-known, i.e. we avoid the uncertainties arising from the freedom to choose the input parton distributions. In fact, since only the π^0 has to be measured in the final state we can include events where part of the jet is lost in the beam pipe. This allows us to reach higher values of x_j than for the DIS + jet process as can be seen from Fig. 3.10. On the other hand, for a fixed value of x higher x_j means smaller $z = x/x_j$ and therefore a longer lever for the BFKL evolution. As explained in Chapter 3 we impose the boundary condition that at some starting value z_0 of z we only have the "quark box" (see Fig. 3.5) and no gluon radiation. To be precise we utilize expressions (3.22) and (3.23) assuming three flavours of massless quarks ($m_q = 0$). Then we use the BFKL equations (3.11) to evolve to smaller values of z. In this way we obtain the functions Φ which we have to substitute in the differential structure functions (3.7). Recall that the Φ_i describe the virtual γ – virtual gluon fusion process including the ladder formed from the gluon chain of Fig. 5.1(a). In practice we follow the approach outlined in Section 3.2.3 and solve the BFKL equations (3.38) numerically for the functions H_i defined in (3.37) where we allow the coupling α_S to run. For the lower limit on the transverse momentum integration in (3.38) we choose $k_0^2 = 1$ GeV^2. We impose the boundary conditions (3.39) with $z_0 = 0.1$.

5.3.2 The DIS + forward π^0 cross section

Next let us consider the process where the forward jet fragments into π^0's as shown schematically in Fig. 5.1(b). We are looking at the case where the π^0 is collinear with the parent quark jet. This means that if the π^0 carries a fraction x_π of the proton's longitudinal momentum, then it carries a fraction $z = x_\pi/x_j$ ($0 \leq z \leq 1$) of the parent jet's longitudinal momentum and its transverse momentum $k_{\pi T} = z k_{jT}$. In order to calculate the cross section for DIS + π^0 production we have to convolute the DIS + jet cross section with the π^0 fragmentation functions which we discussed in Section 5.2. We

obtain

$$\frac{\partial\sigma_\pi}{\partial x_\pi \partial k_{\pi T}} = \int_{x_\pi}^1 dz \int dx_j \int dk_{jT}^2 \left[\frac{\partial\sigma_g}{\partial x_j \partial k_{jT}^2} D_g^{\pi^0}\left(z, k_{\pi T}^2\right) + \sum_q \left(\frac{\partial\sigma_q}{\partial x_j \partial k_{jT}^2} D_q^{\pi^0}\left(z, k_{\pi T}^2\right) \right) \right] \times \times \delta\left(x_\pi - z x_j\right) \delta\left(k_{\pi T} - z k_{jT}\right) \tag{5.26}$$

where the sum over q runs over all quark and antiquark flavours. The partonic differential cross sections can be obtained from (3.6) and (3.7) by substituting for the sum over the parton distributions $\sum_a f_a$ either the gluon distribution g or the quark or antiquark distribution $\frac{4}{9}q$ or $\frac{4}{9}\bar{q}$ respectively. In analogy to choosing $z_0 = 0.1$ in (3.39) we impose the constraint $x/x_\pi < 0.1$, i.e. $x/x_j < 0.1$ since $x_\pi < x_j$, on the x_j integration here. Recall that the functions $D_g^{\pi^0}(z, k_{\pi T}^2)$ and $D_q^{\pi^0}(z, k_{\pi T}^2)$ in (5.26) give the probability that a gluon or quark jet fragments into a π^0 carrying a fraction z of the parent jet's momentum. We choose the fragmentation scale $\mu^2 = k_{\pi T}^2$ here but we will also try varying it later. Because of relation (5.20) which followed from SU(2) symmetry, eq. (5.26) describes the average of the cross sections for π^+ and π^- production.

5.4 Cuts for the DIS + π^0 process

We use (5.26) to calculate the event rate for deep inelastic scattering in which, in addition to the scattered electron, the π^0 is measured in the final state. Of course, to obtain the total cross section we will have to introduce limits on the x_π and $k_{\pi T}$ integrations which we will specify later. As for the DIS + forward photon measurement we require the outgoing lepton to lie in the kinematic region defined by (4.11). Here we take the energies of the colliding particles to be $E_e = 27.6$ GeV and $E_p = 820$ GeV. Let us now investigate what other cuts we have to impose. For a definition of the variables which we will use see Fig. 5.4.

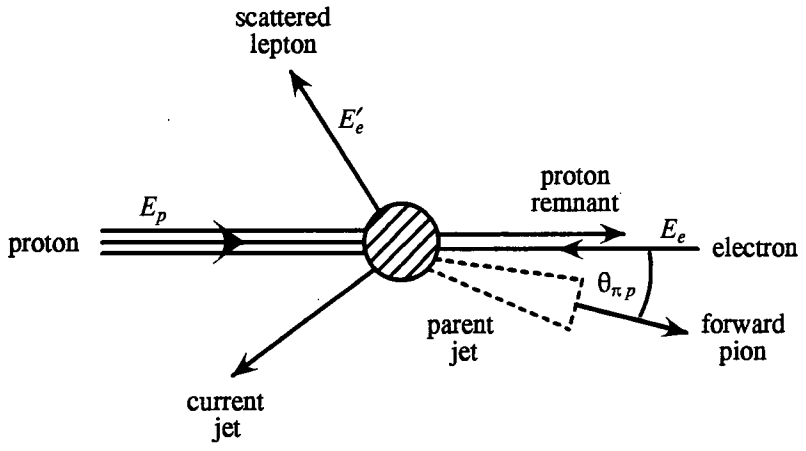

Figure 5.4: Kinematics of the deep inelastic + forward π^0 process.

5.4.1 The hemisphere cut

To ensure that the π^0 is really a fragment of the forward jet (and does not come from the quark-antiquark pair which form the quark box) we require the π^0 to be emitted in the forward hemisphere in the virtual photon – proton centre-of-mass frame. If we express the pion four momentum in terms of Sudakov variables

$$k_\pi = x_\pi p + \beta_\pi q' + \boldsymbol{k}_{\pi T} \tag{5.27}$$

then the forward hemisphere requirement is

$$x_\pi > \beta_\pi. \tag{5.28}$$

Since the outgoing pion satisfies the on-mass-shell condition $k_\pi^2 = m_\pi^2 \approx 0$ we have

$$\beta_\pi = \frac{x}{x_\pi}\frac{k_{\pi T}^2}{Q^2}. \tag{5.29}$$

Then (5.28) gives

$$x_j > x_\pi > \sqrt{x k_{\pi T}^2/Q^2}. \tag{5.30}$$

We thus have an implicit lower limit on the x_j integration in (5.26), which is generally stronger than the condition $x_j > 10x$ imposed on the solution of the BFKL equation.

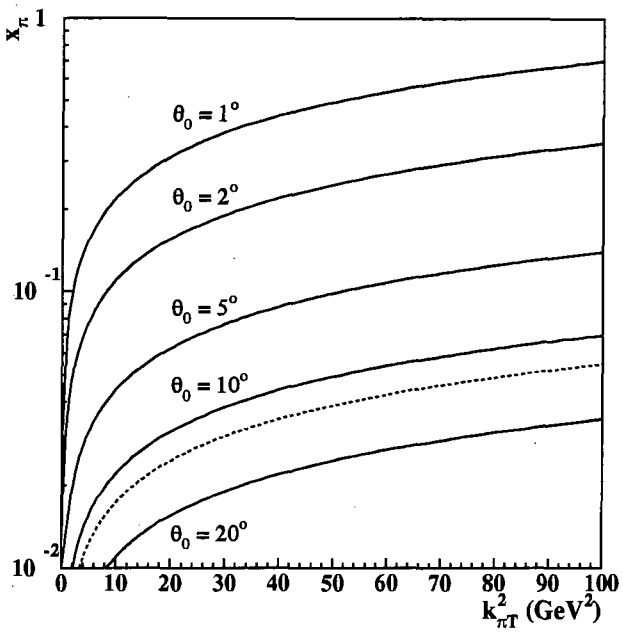

Figure 5.5: The relation between the π^0 kinematic variables for DIS + π^0 events with $x = 6 \times 10^{-4}$ and $Q^2 = 20$ GeV^2 for various choices of the angle θ_0 in (5.31). In the HERA (27.6 × 820 GeV) laboratory frame the pion angle $\theta_{\pi p}$ to the proton direction is not uniquely specified by $(x, Q^2; x_\pi, k^2_{\pi T})$. Varying the remaining azimuthal angle transforms the lines of constant $\theta_{\pi p}$ into narrow bands in the x_π, $k^2_{\pi T}$ plane. Here we averaged over the azimuthal degree of freedom. The plot is insensitive to variations of x, Q^2 over their relevant intervals. The continuous lines are the *upper* boundary on the allowed kinematic region for different choices of θ_0. The dashed line represents the *lower* boundary given by the hemisphere cut, (5.28), for $x = 6 \times 10^{-4}$ and $Q^2 = 20$ GeV^2.

5.4.2 The beam pipe cut

Another problem to be taken into account is that at HERA pions can only be detected if they are emitted at a large enough angle to the proton beam. This also ensures that there is no contamination from pions produced in the proton remnant. We require

$$\theta_{\pi p} > \theta_0. \tag{5.31}$$

This cut is analogous to the beam pipe cut we imposed for the forward photon, c.f. Section 4.3.3. Proceeding in the same way as for the forward photon we can derive a relation between x_π and $k^2_{\pi T}$ analogous to (4.21). In Fig. 5.5 we show this relation between the pion kinematic variables for different choices of the minimum angle θ_0 defined in the

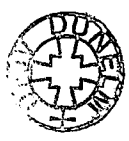

HERA frame. We find that pions with large longitudinal momentum fraction x_π are only emitted at small angles $\theta_{\pi p}$. To reach larger x_π for a given $\theta_{\pi p}$ we can measure pions with larger $k_{\pi T}^2$ but at a depleted event rate. In the same figure we also plot the boundary given by the hemisphere cut, (5.28), for $x = 6 \times 10^{-4}$ and $Q^2 = 20$ GeV^2, which acts as a *lower* limit on the allowed kinematic region. We will use $\theta_0 = 5°$ for the main presentation of our results (although later we compare the predictions with those obtained with $\theta_0 = 7°$).

5.5 Predictions for the DIS + π^0 cross section

Now we are in the position to give numerical predictions for the cross section for DIS + π^0 production using (5.26) and implementing the cuts that we discussed above. Let us just summarize the cuts and limits we impose in the cross section calculation:

- the electron acceptance region given in (4.11)
- the hemisphere cut (5.28)
- $\theta_{\pi p} > \theta_0 = 5°$
- $3 < k_{\pi T} < 10$ GeV
- $x_\pi > 0.05$.

Recall that it follows from (5.20) that the cross section for π^0 production equals the average of the cross sections for π^+ and π^- production. Therefore the results we will show in the following multiplied by a factor of 2 will be valid for charged pion production. Throughout the analysis we assumed three flavours of massless quarks.

In Fig. 5.6 we plot the x dependence of the DIS + π^0 cross section integrated over bins of size $\Delta x = 2.10^{-4}$ and $\Delta Q^2 = 10$ GeV^2 for three different Q^2 bins, namely 20-30, 30-40, 40-50 GeV^2. Here we imposed the cuts listed above and used the fragmentation functions [61] at scale $\mu^2 = k_{\pi T}^2$. We compare the results obtained when BFKL small x resummation is included with the case when gluon radiation is neglected ($\Phi_i = \Phi_i^{(0)}$ in

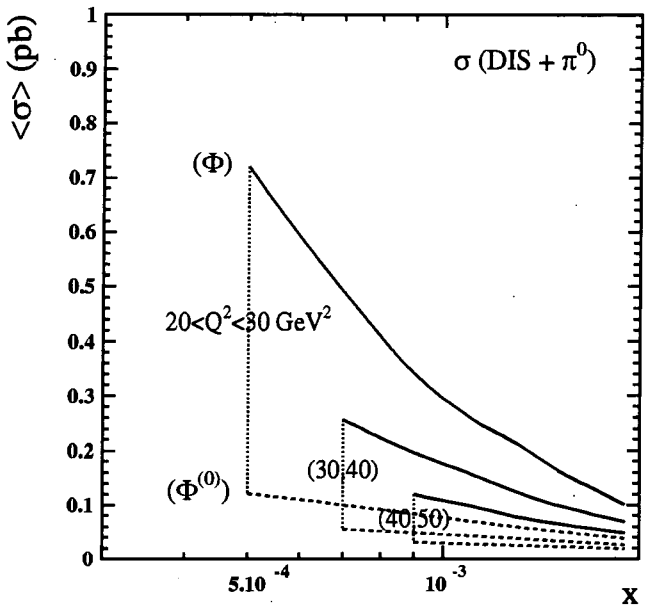

Figure 5.6: The cross section, $\langle\sigma\rangle$ in pb, for deep inelastic + π^0 events integrated over bins of size $\Delta x = 2 \times 10^{-4}$, $\Delta Q^2 = 10$ GeV^2 which are accessible at HERA for π^0's with transverse momentum $3 < k_{\pi T} < 10$ GeV where the constaints $x_\pi > 0.05$, $\theta_{\pi p} > 5°$, and the hemisphere cut, (5.28), were imposed. The fragmentation functions were evaluated at scale $k^2_{\pi T}$. The $\langle\sigma\rangle$ values are plotted at the central x value in each Δx bin and joined by straight lines. The x dependence is plotted for three different ΔQ^2 bins, namely (20,30), (30,40) and (40,50) GeV^2. The continuous curves show $\langle\sigma\rangle$ calculated with Φ_i obtained from the BFKL equation. The corresponding $\langle\sigma\rangle$ values calculated neglecting soft gluon resummation and just using the quark box approximation $\Phi_i = \Phi_i^{(0)}$ are plotted as dashed curves. For clarity a dotted vertical line joins each pair of curves belonging to the same ΔQ^2 bin.

(3.7)). In the first case the strong x dependence of the cross section is driven by the small z behaviour of the Φ_i and therefore there is a strong enhanced increase with decreasing x. For example, if we compare the cross section for $x \approx 5 \times 10^{-4}$ in the two cases, we find that the results are about a factor 7 larger when BKFL evolution is included than when it is neglected. This enhancement is the signature of BFKL soft gluon resummation. In fact the BFKL behaviour should be identified via the shape in x rather than the value of the cross section, since the latter is subject to normalisation uncertainties (see Section 3.2.4 and ref. [48]). In Fig. 5.7 we show the cross section (in fb), for the same cuts as in Fig. 5.6, in various bins in x and Q^2 which are accessible at HERA. We find that the cross section drops off very rapidly with Q^2 which means that we can reach the highest values for the bins with $10 < Q^2 < 20$ GeV^2 and x very small.

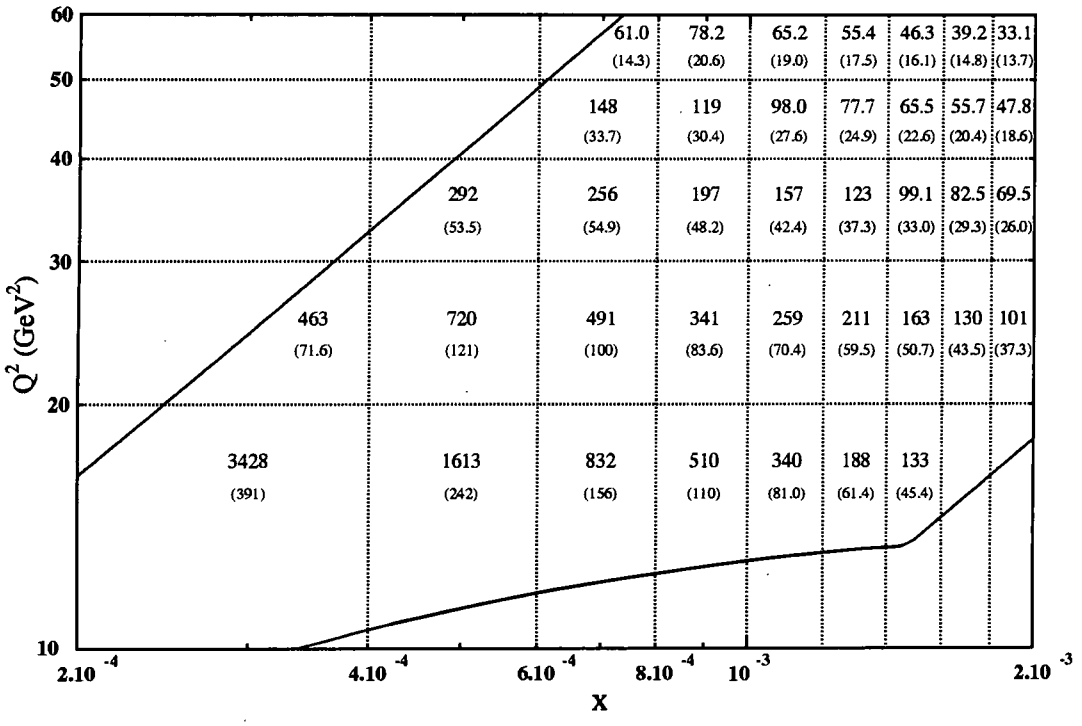

Figure 5.7: The cross section, $\langle\sigma\rangle$ in fb, for deep inelastic + π^0 events in various $(\Delta x, \Delta Q^2)$ bins which are accessible at HERA, and integrated over the region $3 < k_{\pi T} < 10$ GeV, $\theta_{\pi p} > 5°$, $x_\pi > 0.05$, and subject to the hemisphere cut, (5.28). The fragmentation functions were evaluated at scale $\mu^2 = k_{\pi T}^2$. The values in brackets are the cross sections obtained when using only the quark box approximation $\Phi_i = \Phi_i^{(0)}$. Therefore the difference between the two numbers shown in one bin is the enhancement due to BFKL soft gluon resummation. Recall that (5.20) implies that the results shown for the DIS + π^0 cross section here equal the average of the cross sections for π^+ and π^- production. The curves are the boundaries of the acceptance regions at HERA given by $8° < \theta'_{ep} < 172°$ and $0.1 < y < 0.9$.

5.5.1 Dependence of the DIS + π^0 cross section on the k_π integration region and on the fragmentation scale

Of course, the DIS + π^0 cross section depends on the values chosen for the cuts. In Table 5.1 we show the effect of changing the limits on the $k_{\pi T}$ integration. All other cuts are the same as for Fig. 5.7. Since the cross section decreases with increasing $k_{\pi T}$ it is more sensitive to the lower limit on the $k_{\pi T}$ integration than to the upper limit.

The DIS + π^0 cross section does not only depend on the cuts but also on the fragmentation scale used in the calculation. To obtain the results shown in Figs. 5.6 and

Table 5.1: The DIS + π^0 cross section in the bin $10^{-3} < x < 1.2 \times 10^{-3}$, $20 < Q^2 < 30$ GeV^2 as calculated in Fig. 5.7, but for different choices of the limits of the integration over the transverse momentum of the π^0.

$k_{\pi T,min}$ [GeV]	$k_{\pi T,max}$ [GeV]	σ [pb]
3	8	0.23
3	10	0.26
5	10	0.18

Table 5.2: The DIS + π^0 cross section in the bin $10^{-3} < x < 1.2 \times 10^{-3}$, $20 < Q^2 < 30$ GeV^2 calculated imposing the same cuts as for Fig. 5.7, but evaluating the fragmentation functions at the three different scales $\frac{1}{2}k^2_{\pi T}$, $k^2_{\pi T}$ and $2k^2_{\pi T}$.

fragmentation scale	σ [pb]
$\frac{1}{2}k^2_{\pi T}$	0.31
$k^2_{\pi T}$	0.26
$2k^2_{\pi T}$	0.23

5.7 we used the pion fragmentation functions at scale $\mu^2 = k^2_{\pi T}$. In Table 5.2 we show the cross section for the deep inelastic + π^0 process in the bin $10^{-3} < x < 1.2 \times 10^{-3}$, $20 < Q^2 < 30$ GeV^2 calculated imposing the same constraints and including BFKL soft gluon resummation but evaluating the pion fragmentation functions at the scales $\frac{1}{2}k^2_{\pi T}$, $k^2_{\pi T}$ and $2k^2_{\pi T}$. The values demonstrate the scale ambiguity in the prediction of the cross section.

5.5.2 Background from photons which are fragments of the forward jet

Since π^0's are measured through their decay into two photons ($\pi^0 \to \gamma\gamma$) there is a background from events in which the parent jet fragments into a photon which is emitted collinearly, see Fig. 5.8.

The fragmentation of a parton jet into a photon can be treated analogously to the fragmentation into a hadron. Again we define a fragmentation function $D_i^\gamma(z, \mu^2)$ which

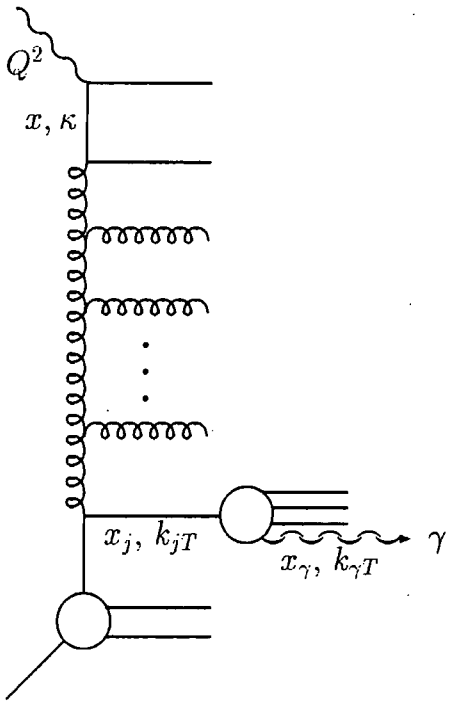

Figure 5.8: Diagrammatic representation of the background to deep-inelastic + forward π^0 events arising from photons which are fragments of the forward jet.

gives the probability that a parton i ($i = q, \overline{q}, g$) fragments into a photon which carries a fraction z of its momentum. As before, μ^2 is the fragmentation scale. The μ^2 evolution of the fragmentation functions D_i^γ is described by DGLAP equations similar to (5.14). In analogy to (5.26) the cross section for the background from photons which are fragments of the forward jet is given by

$$\begin{aligned}\frac{\partial \sigma_\gamma}{\partial x_\gamma \partial k_{\gamma T}} &= \int_{x_\gamma}^1 dz \int dx_j \int dk_{jT}^2 \left[\frac{\partial \sigma_g}{\partial x_j \partial k_{jT}^2} D_g^\gamma \left(z, k_{\gamma T}^2\right) \right. \\ &\left. + \sum_q \left(\frac{\partial \sigma_q}{\partial x_j \partial k_{jT}^2} D_q^\gamma \left(z, k_{\gamma T}^2\right) \right) \right] \times \\ &\times \delta\left(x_\gamma - z x_j\right) \delta\left(k_{\gamma T} - z k_{jT}\right) \end{aligned} \tag{5.32}$$

where we assumed collinear fragmentation. We estimated this background using the fragmentation functions of Owens [64] and found that it is 1-2 % of the cross section for π^0 production.

Considering the smallness of the background from photons which are fragments of the forward jet, a comment on the errors on the calculation of the cross section for pion production is due here. From the numerical point of view there is an error from the Monte-Carlo integration used to evaluate (5.26) which is of the order of 5 %. To our knowledge the errors on the pion fragmentation functions are of the order of a few percent for quarks and 30 - 40 % for gluons [65]. Since the dominant contribution to the cross section for pion production comes from the fragmentation of gluons we expect these errors on the fragmentation functions to result in an error of at most 25 % on the cross section. The parametrisations of the fragmentation functions describe the DGLAP evolution correctly up to 10 % [61]. We found that our results are more sensitive to the normalisation of the fragmentation functions than to their shape.

5.5.3 Comparison with the DIS + forward jet measurement

Finally let us compare our predictions for DIS + forward π^0 production as shown in Fig. 5.7, with the corresponding cross sections for the DIS + forward jet events, the process originally proposed by Mueller [39] as the probe of small x dynamics which we discussed in Chapter 3. In order to quantify the suppression due to the fragmentation of the jet into the π^0 we integrate the DIS + jet differential structure functions given in (3.7) over the same domains of x_j and k_{jT}^2 that we used for x_π and $k_{\pi T}^2$ for the DIS + π^0 predictions. To be precise we integrate over the region $3 < k_{jT} < 10$ GeV and $\theta_{jp} > 5°$ with a hemisphere cut for the jet in analogy to (5.28), that is $x_j > \beta_j$. The upper and lower numbers in Fig. 5.9 compare the DIS + π^0 with the DIS + jet cross section in the various bins of x and Q^2. We see that the fragmentation of the forward jet into a π^0 meson costs a factor of about 40 in the suppression in event rate. Whether this loss of event rate is compensated by the advantage of identifying a forward π^0 as compared to a jet (adjacent to the proton remnants) is an experimental question. Table 5.3 offers a guide to the possible gain using the π^0 signal. For instance, if we were able to identify π^0 mesons down to 5° in angle and 5 GeV in k_T with the same accuracy as jets down to 7° in angle and 7 GeV in k_T then we would gain back a factor of 4. Moreover, if we were to add in the DIS + forward $\pi^\pm$ signal then we gain an extra factor of 3. Table 5.3 also shows

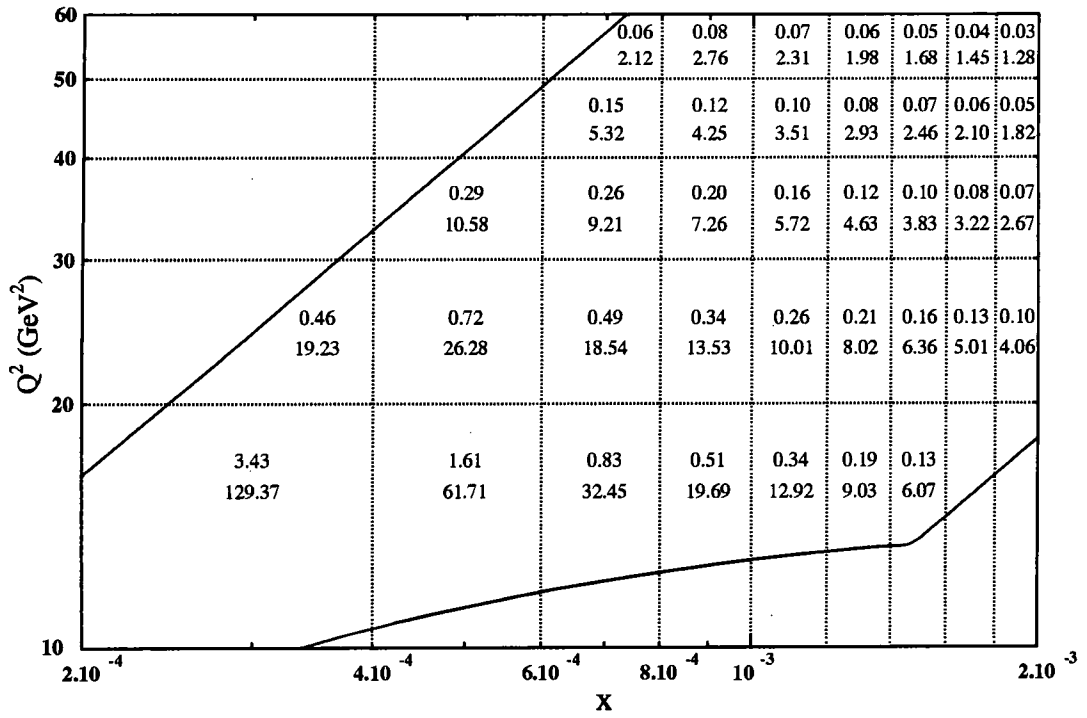

Figure 5.9: The upper and lower numbers are respectively the DIS + π^0 and DIS + jet cross sections (in pb) in various bins of x and Q^2. For the pion the cuts are those given in Fig. 5.7, and exactly the same cuts are used for the forward jet.

Table 5.3: The DIS + π^0 and DIS + jet cross sections in the bin $10^{-3} < x < 1.2 \times 10^{-3}$, $20 < Q^2 < 30$ GeV^2 as calculated for Fig. 5.9, but integrated over domains with different choices of the minimum angle θ_0 between the proton and the π^0 or the jet, and of the minimum transverse momentum $k_{T,min}$ of the π^0 or the jet.

$k_{T,min}$ [GeV]	θ_0	σ_{π^0} [pb]	σ_j [pb]
3	5°	0.26	10.3
3.5	5°	0.26	10.3
5	5°	0.18	8.0
7	5°	0.07	3.7
3.5	7°	0.08	3.4
5	7°	0.08	3.4
7	7°	0.04	2.0

that in the HERA regime, where we need to take x_j sufficiently large (say $x_j > 0.05$) to make x/x_j small, the low k_T events are kinematically forbidden by the cuts. For example, for $\theta_0 = 7°$ we find that $k_T > 5.0$ GeV, while for $\theta_0 = 5°$ we have $k_T > 3.6$ GeV.

5.6 Discussion

In principle, the DIS + jet measurement should be an excellent way of identifying the BFKL soft gluon resummation effects at HERA as we saw in Chapter 3. It turns out, however, that it is experimentally quite difficult to measure a forward jet so close to the proton remnants. We therefore suggested studying the fragmentation of this forward jet into a single energetic decay product, the π^0. This should be easier to measure. (The DIS + π^0 signal can, of course, be supplemented by also observing jet fragmentation into $\pi^\pm$ mesons). We found that when we include BFKL dynamics in the calculation of the cross section it leads to the characteristic steep rise with decreasing x. The disadvantage of using the DIS + π process is that the event rate is lower than for DIS + forward jet. We quantified the suppression which arises from this jet $\to \pi$ fragmentation. It is an experimental question as to whether the loss of event rate can be compensated by the more forward domain accessible for π detection and the more accurate measurement of the kinematic variables possible for pions as opposed to jets. We presented sample results for different acceptance cuts to help provide an answer. In fact, our choice of cuts was rather conservative. In Chapter 7 we will return to the DIS + forward π^0 measurement and update our prediction for the cross section imposing more realistic cuts which give an enhanced event rate.

Since π^0's are measured via the two photon decay, there is a background to the deep-inelastic + π^0 measurement from events in which the parent jet fragments into a photon which is being emitted collinearly to the jet. We found that this background is about 1-2 %. We conclude that deep-inelastic + pion events should be a good way of probing small x dynamics at HERA.

Chapter 6

Deep inelastic + jet — comparison with the data

6.1 Motivation

In Chapter 3 we proposed the study of deep inelastic events which contain an identified forward jet as a way of investigating the underlying dynamics at small x at HERA. The process is shown is Fig. 3.1 where we defined the variables we use. We explained that we select events where the forward jet carries a fraction x_j of the proton's longitudinal momentum which is large. Since we focus on the small-x region x/x_j is then small and we can investigate the $(x/x_j)^{-\lambda}$ behaviour. Large x_j also has the advantage that we only have to evaluate the parton densities in a region where the uncertainties are very small. In addition we require the transverse momentum of the jet to obey $k_{jT}^2 \simeq Q^2$. This implies that DGLAP evolution is neutralized and the diffusion into the infrared region is avoided. We saw how the cross section for DIS + jet events can be calculated from BFKL dynamics and what kind of cuts have to be imposed. In Section 3.4 we concluded that from the point of view of a theorist the DIS + jet process provides an excellent, clear way of studying BFKL dynamics at HERA. However, as we pointed out, the measurement of the forward jet is not easy since a jet with large x_j is emitted very close to the proton beam and can mix with the proton remnants. Nevertheless, experimental studies have been undertaken by the H1 collaboration [54, 55]. The ZEUS collaboration is currently

also investigating DIS + jet events and first results have been presented recently [56]. In this chapter we will concentrate on a study by H1 [55]. The cuts which this collaboration applied in the measurement differ slightly from the ones described in Section 3.3. We will now calculate the DIS + jet cross section imposing the same cuts which will allow us to compare our BFKL prediction with their data.

The outline of the chapter is as follows: first we will briefly explain how we calculate the deep inelastic + forward jet cross section and then we will list the requirements of the H1 collaboration on the forward jet and on the outgoing lepton. In the final part of the section we will comment on the uncertainties accompaning the BFKL prediction of the forward jet rate. In Section 6.3 we will show some results for the DIS + jet cross section when including BFKL evolution in the calculation. Finally we will present our conclusions.

6.2 Description of the DIS + forward jet data

In the following we will summarize the formalism used to calculate the cross section for deep inelastic events containing an identified jet and list the cuts imposed by the H1 collaboration in the experiment. Then we will explain how we proceed to describe the H1 data.

6.2.1 Calculation of the DIS + jet cross section

We calculate the DIS + jet cross section applying again the formalism displayed in Section 3.2. That is we use expression (3.6) for the DIS + jet cross section where we substitute the differential structure functions (3.7). As before we obtain the functions Φ_i by numerically solving the BFKL equations allowing the coupling α_S to run. However, we now explicitly include the $m_c \neq 0$ charm contribution. To be precise we solve the BFKL equation (3.11) rewritten in terms of the modified function $H_i = (3\alpha_S(k_T^2)/\pi)\Phi_i(z, k_T^2, Q^2)$ following the prescription that was outlined in Section 3.2.3. This choice of scale for α_S is consistent with the double logarithm limit and with the NLO $\ln(1/x)$ analysis of ref. [33].

We determine the functions Φ_i for $z < z_0$ by solving the BFKL equation as described in Section 3.2.3 starting from the boundary condition (3.12),

$$\Phi_i(z_0, k_T^2, Q^2) \;=\; \Phi_i^{(0)}(z_0, k_T^2, Q^2),$$

where $\Phi_i^{(0)}(k_T^2, Q^2)$ are the contributions of the quark box (and crossed box) given in (3.22) and (3.23). We take u, d, s to be massless ($m_u = m_d = m_s = 0$) and the charm quark to have mass $m_c = 1.4$ GeV in the summation over the quarks. Our choice for z_0 and the cut-off k_0^2 in (3.38) will be specified later.

6.2.2 Cuts imposed by the H1 collaboration

The H1 collaboration collected the data for the forward jet analysis under consideration during the 1994 running period in which 27.5 GeV positrons were collided with 820 GeV protons. The data sample evaluated corresponds to an integrated luminosity of 2.8 pb^{-1}. The following cuts were introduced: H1 require the outgoing lepton to lie in the domain

$$\begin{aligned} y &> 0.1 \\ 160^\circ < \theta'_{ep} &< 173^\circ \\ E'_e &> 11 \text{ GeV}. \end{aligned} \tag{6.1}$$

in the HERA frame. The variables were defined in Fig. 3.7. In Fig. 6.1 we show the limits on the accessible (x, Q^2) range at HERA defined by the constaints on y and θ'_{ep}. This figure can be compared with Fig. 3.8 in which we plotted the "electron" acceptance region corresponding to the cuts on y and θ'_{ep} specified in (4.11) which we applied in the computation of the DIS + γ and the DIS + π^0 cross sections. We see that the H1 choice is far more restrictive.

Let us now consider the limits on the forward jet variables defined in Fig. 3.9. In the H1 analysis the transverse momentum of the jet is required to fulfil $\frac{1}{2}Q^2 < k_{jT}^2 < 2Q^2$. Furthermore, the forward jet is constrained to the region

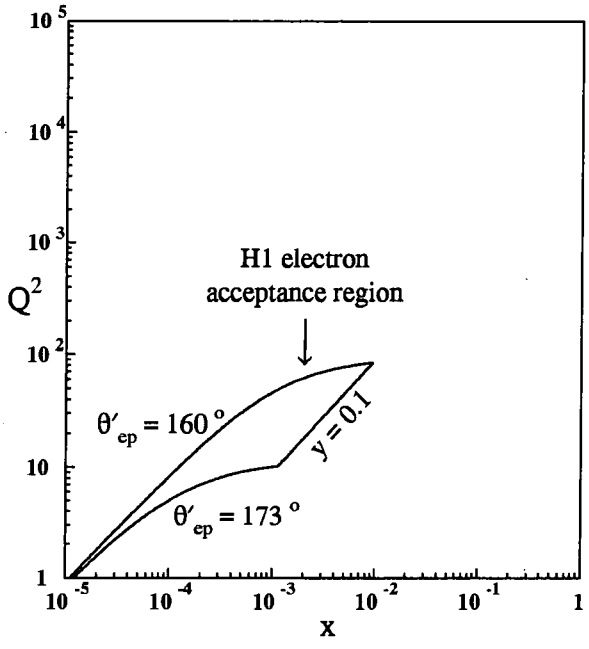

Figure 6.1: The acceptance region in the (x, Q^2) plane for deep inelastic events defined by $160° < \theta'_{ep} < 173°$ and $0.1 < y < 1$ in the HERA (27.5 x 820 GeV) laboratory frame.

$$\begin{aligned} 7° < \theta_{jp} < 20° \\ E_j > 28.7 \text{ GeV} \\ k_{jT} > 3.5 \text{ GeV}. \end{aligned} \tag{6.2}$$

Note that $E_j > 28.7$ GeV corresponds to $x_j > 0.035$. Clearly, with exception of the upper limit on θ_{jp}, these cuts are weaker than the ones we suggested in Section 3.3.2. This is a consequence of the difficulty of the forward jet measurement. Jets can only be measured using the H1 detector if their angle with respect to the proton beam direction $\theta_{jp} > 7°$ in the HERA frame. As we can see from Fig. 3.10 this implies that it is only possible to reach values of $x_j < 0.1$. The lower limit $x_j > 0.035$ on the other hand is smaller than theoretically favourable because it does not allow for a very long BFKL evolution in x/x_j. It is, however, necessary from the experimental point of view in order to have a large enough rate for the DIS + jet events. The additional requirement $\theta_{jp} < 20°$ was introduced to avoid that the forward jet mingles with the current jet. To be able to compare with the H1 data we will impose all the cuts listed above in the calculation of

the DIS + forward jet cross section.

6.2.3 Normalisation of the BFKL prediction

As we explained in Section 3.2.4 the BFKL prediction for the DIS + jet cross section is subject to uncertainties which arise from the freedom to choose the cutoffs on the transverse momentum integrations. In ref. [48] it was found that the shape in x and x_j of the differential structure function $\partial F_2/\partial x_j \partial k_{jT}^2$ – and therefore the cross section – is much less affected by these uncertainties than the normalisation. We will now test if we can describe the H1 data with the values for the cutoffs which we used in the calculation of the DIS + γ and DIS + π^0 cross sections. There we set the lower limit $k_{min}^2 \equiv k_0^2 = 1$ GeV^2 in the BFKL equation (3.38). For practical reasons we also tacitly introduced an upper limit $k_{max}^2 = 10^4$ GeV^2 rather than integrating up to ∞.

So far we have not pointed out that we also have the freedom to choose another parameter, namely the "starting point" z_0 of BFKL evolution. Recall that we solve the BFKL equation for $z = x/x_j$ subject to the boundary condition that at $z = z_0$ we only have the quark box (and crossed box) contributions and no gluon radiation. z_0 should be small enough for the BFKL equation to be valid. For previous predictions [47, 49] of the DIS + jet cross section $z_0 = 0.1$ was used. Here we will vary z_0 and see if we can correctly describe the normalisation of the H1 data.

6.3 Predictions for the cross section for DIS + jet events

We now calculate the cross section for deep inelastic events containing an identified forward jet imposing the cuts used in the H1 measurement and solving the BFKL equations for the H_i (or Φ_i) with the limits $k_{min}^2 = 1$ GeV^2 and $k_{max}^2 = 10^4$ GeV^2. A charm quark mass of 1.4 GeV is assumed here but we will also examine the dependence of the rate on the choice of m_c later. The MRS(R2) [21] set of parton distributions is utilized to obtain $\sum_a f_a$ in (3.7). The cross section should, however, not depend on which set is used

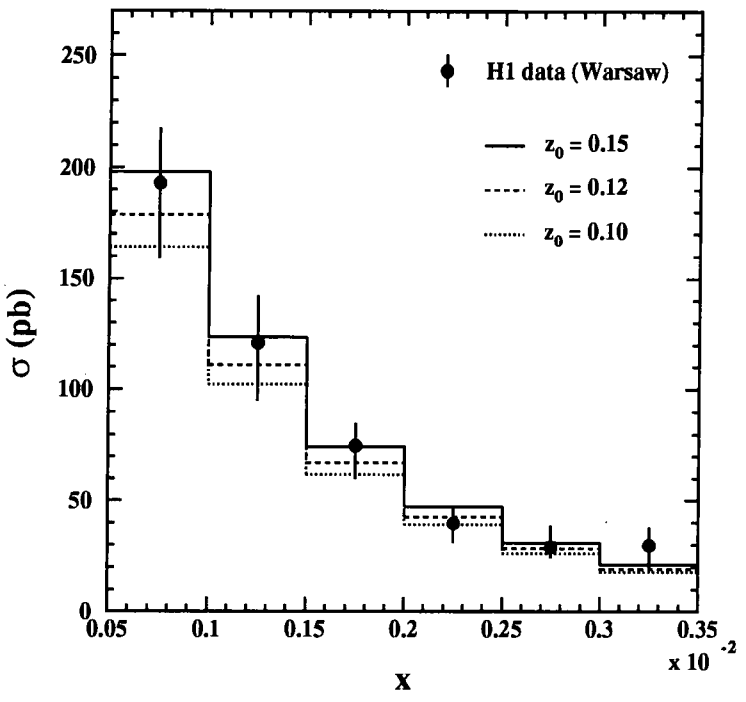

Figure 6.2: The deep inelastic + forward jet cross section in pb integrated over bins of size 5×10^{-4} in x compared to the H1 data presented at the Warsaw conference [55]. As in the H1 measurement the forward jet was required to fulfil $7° < \theta_j < 20°$, $E_j > 28.7$ GeV, and $k_{jT} > 3.5$ GeV. The electron acceptance region is limited by $160° < \theta'_{ep} < 173°$, $E'_e > 11$ GeV, and $y > 0.1$ in the HERA frame. The solid, dashed and dotted lines represent the predictions for the cross section obtained for $z_0 = 0.15$, 0.12 and 0.10 respectively.

because the parton distributions are to be evaluated at x_j which is large. We integrate the cross section over bins of size 5×10^{-4} in x and over the corresponding Q^2 range bounded by the acceptance cuts (6.1). Fig. 6.2 shows the effect on the DIS + jet cross section of varying z_0. The forward jet data [55] presented by the H1 collaboration at the Warsaw conference in 1996 are also displayed. A dotted line represents the result for $z_0 = 0.1$ which especially in the smaller x bins is somewhat low compared to the data. Increasing z_0 gives the dashed and solid curves which correspond to $z_0 = 0.12$ and 0.15 respectively. We find that for $z_0 = 0.15$ the BFKL prediction is in good agreement with the H1 data. Therefore in the remaining part of this chapter and in the following chapters we will always solve the BFKL equation with the boundary condition (3.12) imposed at $z_0 = 0.15$.

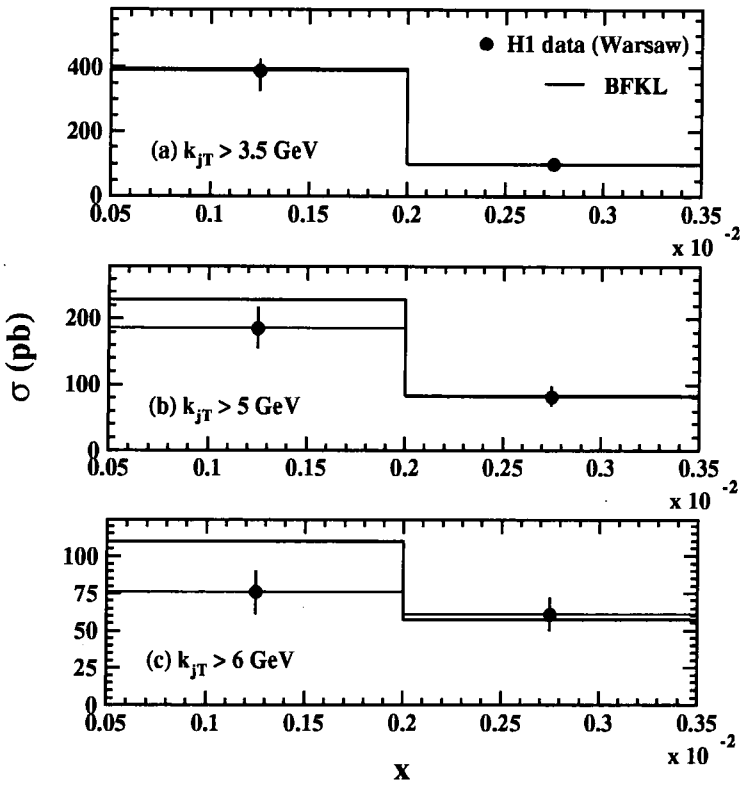

Figure 6.3: The deep inelastic + forward jet cross section in pb integrated over bins of size 1.5×10^{-3} in x compared to the H1 data. Here $z_0 = 0.15$ and the cuts are the same as for Fig. 6.2 with exception of the minimum transverse momentum of the jet. The solid lines correspond to (a) $k_{jT} > 3.5$ GeV, (b) $k_{jT} > 5$ GeV and (c) $k_{jT} > 6$ GeV.

6.3.1 Comparison with the data for different cuts on k_{jT}

The H1 data shown in Fig. 6.2 was obtained requiring the forward jet to have a transverse momentum $k_{jT} > 3.5$ GeV. The collaboration also performed analyses for higher values of the lower limits $k_{jT,min}$ on k_{jT}. Therefore we can investigate if the BFKL prediction for $z_0 = 0.15$ as displayed in Fig. 6.2 but for different choices of $k_{jT,min}$ describes the corresponding data equally well. In Fig. 6.3 we plot the DIS + forward jet cross section in bins of size 1.5×10^{-3} in x where we imposed the same cuts as in the calculation for Fig. 6.2 but varied the mimimum transverse momentum k_{jT} of the jet. The BFKL prediction for the cross section obtained with $z_0 = 0.15$ is compared with the H1 data for (a) $k_{jT} > 3.5$ GeV (as in Fig. 6.2), (b) $k_{jT} > 5$ GeV and (c) $k_{jT} > 6$ GeV. We see

that for the higher values of $k_{jT,min}$ the BFKL result somewhat overestimates the data. This may indicate that $k_{jT,min} = 3.5$ GeV is in fact a bit too low and still allows for non-perturbative effects.

6.3.2 Dependence on the cuts on the transverse momentum integration in the BFKL equation

As explained above the normalisation of the BFKL prediction for the DIS + jet cross section depends on the cutoffs which we impose on the k'^2 integration in the BFKL equations (3.38). Let us consider the upper limit first. In principle we should integrate up to ∞. To be able to do the integration numerically, however, we introduce an upper limit k^2_{max}. Of course we would like the value which we choose for k^2_{max} to be large enough that the result for the functions H_i – and therefore the DIS + jet cross section – is not affected. In the calculation of the BFKL prediction shown in Fig. 6.2 we used $k^2_{max} = 10^4$. Now we re-do the computation of the DIS + jet rate with $z_0 = 0.15$ and for the same cuts but for different values of k^2_{max}. In Fig. 6.4(a) we plot the resulting cross section in the bin defined by $5 \times 10^{-4} < x < 10^{-3}$ versus k^2_{max}. We find that the cutoff $k^2_{max} = 10^4$ is indeed large enough to have no influence on the magnitude of the DIS + forward jet cross section. The effect of varying the lower limit k^2_{min} on the rate in the same x bin is shown in Fig. 6.4(b) where we set $k^2_{max} = 10^4$. We see that, as expected, the dependence on the lower limit on the k'^2 integration in the BFKL equations (3.38) is stronger than on the upper limit.

6.3.3 Effect on the DIS + jet cross section of varying the charm quark mass

In the 1996 Review of Particle Physics [63] it is stated that the charm quark has a mass m_c between 1.0 GeV and 1.6 GeV. So far in the calculation of the cross section for deep inelastic events containing an identified forward jet we assumed that $m_c = 1.4$ GeV. In this section we will investigate the effect on the cross section of varying the charm quark mass within the interval quoted by the Particle Data Group. We once again compute

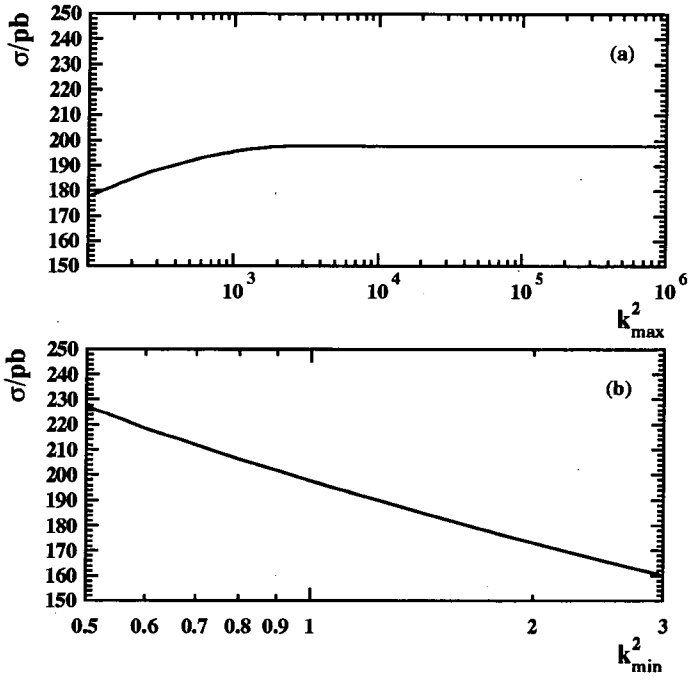

Figure 6.4: The dependence of the deep inelastic + forward jet cross section in pb in the bin $5 \times 10^{-4} < x < 10^{-3}$ on (a) the upper limit k^2_{max} and (b) the lower limit k^2_{min} on the transverse momentum integration in the BFKL equations. The cuts are the same as for Fig. 6.2 and $z_0 = 0.15$.

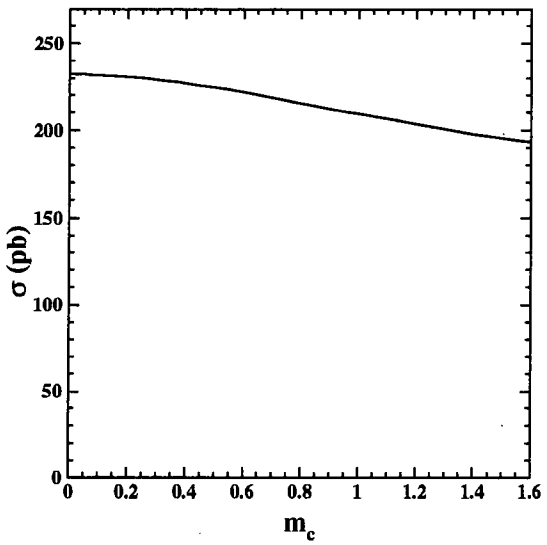

Figure 6.5: Dependence of the deep inelastic + forward jet cross section in pb in the bin $5 \times 10^{-4} < x < 10^{-3}$ on the charm quark mass m_c. The cuts are the same as for Fig. 6.2 and $z_0 = 0.15$.

the DIS + jet rate for $z_0 = 0.15$ subject to the same cuts as for Fig. 6.2 but for various choices of m_c. Fig. 6.5 displays the resulting rate in the bin $5 \times 10^{-4} < x < 10^{-3}$. We find that using a different charm mass (in the interval $1.0 < m_c < 1.6$) in the calculation would change the BFKL prediction given in Fig. 6.2 by maximally 5 %. Also shown is the value of the DIS + jet rate when setting $m_c = 0$. In this case, since the individual quarks contribute to the quark box expressions (3.22) and (3.23) weighted by their charge squared e_q^2, 40 % of the cross section is due to charm quarks in the box. This implies that the light quark contribution to the rate is about 139 pb. Therefore, for $m_c = 1.4$ GeV approximately 30 % of the DIS + jet cross section in the given bin is due to charm quarks in the quark box.

6.4 Summary and conclusion

In this chapter we studied deep inelastic events containing an identified forward jet as a way of identifying the underlying dynamics at HERA and pointed out the advantages of this process. We calculated the DIS + jet cross section imposing the cuts which the H1 collaboration applied in the measurement and compared with their data. We found that the BFKL prediction describes the x-dependence of the data well. On the other hand, as was shown in ref. [66], DGLAP based Monte Carlo event generators clearly underestimate the data. So does the result of a calculation in which BFKL evolution is neglected (Born level prediction) [57]. When comparing with the DIS + jet data we have to bare in mind that the experimentalists measure a hadron jet whereas the BFKL based prediction which we presented is on the parton level. However, since hadronisation effects are expected to be small [66], we think it is fair to conclude that the data support the validity of BFKL dynamics in the small-x region at HERA.

In the remaining part of Section 6.3 we investigated the dependence of the DIS + forward jet cross section on various parameters. We found that for higher values of the minimum allowed transverse momentum $k_{jT,min}$ the BFKL prediction overestimates the data in the smallest x bin. We interpreted this as a sign that $k_{jT,min} = 3.5$ GeV is too low as a cut and that a higher value should be chosen. Of course, this would reduce the

rate and therefore the statistics. Next we studied the dependence of the DIS + jet cross section on the cutoffs on the transverse momentum integration in the BFKL equation. We verified that the cross section is indeed not affected by the upper limit cutoff $k^2_{max} = 10^4$ GeV^2. As was shown in ref. [48] varying the lower limit k_0^2 in (3.38) mainly changes the normalisation of the BFKL prediction. Finally we calculated the DIS + jet rate for different values of the charm quark mass and found that the dependence on m_c is relatively weak.

In summary we conclude that the data presented by the H1 collaboration show signs of BFKL soft gluon resummation. We suggest that further studies are undertaken imposing a higher cut on the transverse momentum of the forward jet. Of course, it would also be useful if jets could be detected at smaller values of the angle θ_{jp} of the jet with respect to the proton direction since this would allow for higher values of x_j and therefore a longer BFKL evolution.

Chapter 7

An update of the DIS + π^0 prediction

7.1 Motivation

In Chapter 5 we proposed a modification of the deep inelastic + forward jet measurement. There we suggested that the forward jet is identified through the measurement of a single energetic decay product. We pointed out that the π^0 is most suitable since it is the hadron which can be detected in the most forward direction in the detectors at HERA. The advantage of the DIS + π^0 measurement compared to the DIS + jet process is that π^0's are easier to measure than a jet close to the proton remnant. On the other hand, of course, we expect the event rate to be suppressed due to the fragmentation. In Chapter 5 we computed the DIS + π^0 cross section by convoluting the parton-level DIS + jet cross section as obtained from BFKL dynamics with the fragmentation functions. We found that we lose about a factor 40 in going from the DIS + jet process to DIS + π^0 for the selection cuts which we suggested. However, we also mentioned that our choice of cuts may be too conservative [67]. Therefore, in this chapter our aim is to investigate how a relaxation of the cuts would affect the DIS + π^0 cross section. In particular, we will predict the rate expected for the requirements which are currently being imposed by the H1 collaboration in a first DIS + π^0 measurement. We will also discuss if their choice of cuts is theoretically favourable. In Section 7.4 we will then show a comparison of the

BFKL prediction with the first preliminary data on forward π^0 production very recently presented by the H1 collaboration [68].

In addition to imposing less strict cuts we also improve our calculation of the DIS + π^0 cross section. As we will see we can take advantage of the H1 DIS + jet data [55] and use them to fix the normalisation of the BFKL prediction. Whereas in Chapter 5 we only included three active flavours in the computation of the rate we will here explicitly allow for charm quarks in the quark box.

The outline of the chapter is as follows. First we will explain how we calculate the DIS + π^0 cross section focussing in particular on the normalisation of the prediction. Then we will summarize the cuts which we impose in the calculation and which are being used by the H1 collaboration in the measurement. In Section 7.3 we will show predictions for the new set of cuts and compare with the corresponding results obtained when neglecting BFKL evolution. After that we will comment on whether these cuts are acceptable from a theorist's point of view and also compare with the cross section for the original DIS + forward jet process. Then, in Section 7.4, we will show a comparison of the BFKL prediction for forward π^0 production with the preliminary H1 data. In the final section we will give our conclusions.

7.2 Calculation of the DIS + π^0 cross section

We compute the DIS + π^0 differential cross section from (5.26) as described in Section 5.3.2 using the next-to-leading order fragmentation functions given in ref. [61]. To obtain the partonic differential cross sections $\partial\sigma_i/\partial x_j \partial k_{jT}^2$ $(i = q, \overline{q}, g)$ we proceed as explained for the deep inelastic + jet process in Section 6.2.1 allowing for charm quarks in the quark box. We assume a charm quark mass $m_c = 1.4$ GeV and utilize the MRS(R2) [21] set of parton distributions.

7.2.1 Normalizing the solution Φ of the BFKL equation

The calculation of the DIS + π^0 cross section presented in this chapter differs from the one in Chapter 5 in the following key point. In Section 6.2.3 we pointed out that the normalisation of the DIS + jet cross section is subject to uncertainties arising mainly from the cutoffs which have to be imposed on the transverse momentum integrations when obtaining the functions Φ_i $(i = T, L)$ from the BFKL equations. We also noted that the rate somewhat depends on the value which is chosen for the "starting point" z_0 of the BFKL evolution. Recall that we solve the BFKL equations subject to the boundary condition that for $z = z_0$ the Φ_i are given by the quark box contributions. When we calculated the DIS + π^0 cross section in Chapter 5 we used $z_0 = 0.1$ and chose the cutoff $k_0^2 = 1$ GeV^2 in the BFKL equations (3.38). In this chapter, however, we will make use of the availability of the DIS + forward jet data to fix the normalisation of the BFKL functions Φ_i. The idea is that we vary z_0, and in principle also k_0^2, until we find values which allow a description of the H1 DIS + jet data [55]. Then we use the Φ_i obtained with this choice of parameters to calculate the DIS + π^0 cross section. This should enable us to make an *absolute* BFKL prediction for the first time.

Let us return to Section 6.3. There we fixed $k_{min}^2 \equiv k_0^2 = 1$ GeV^2 and varied z_0, see Fig. 6.2. We found that the BFKL prediction for $z_0 = 0.15$ is in good agreement with the data. In Fig. 7.1 we show again the DIS + jet cross section in pb integrated over bins of size 5×10^{-4} in x as obtained from BFKL dynamics starting the evolution at $z_0 = 0.15$. The same cuts where imposed as for Fig. 6.2, i.e. the ones applied by the H1 collaboration, (6.1) and (6.2). We will use the functions Φ_i which led to this prediction in the calculation of the DIS + π^0 cross section.

7.2.2 Cuts imposed in the calculation of the cross section

Very recently the H1 collaboration has performed the first deep inelastic + forward π^0 measurement [68]. Therefore, in our calculation of the cross section we will impose the

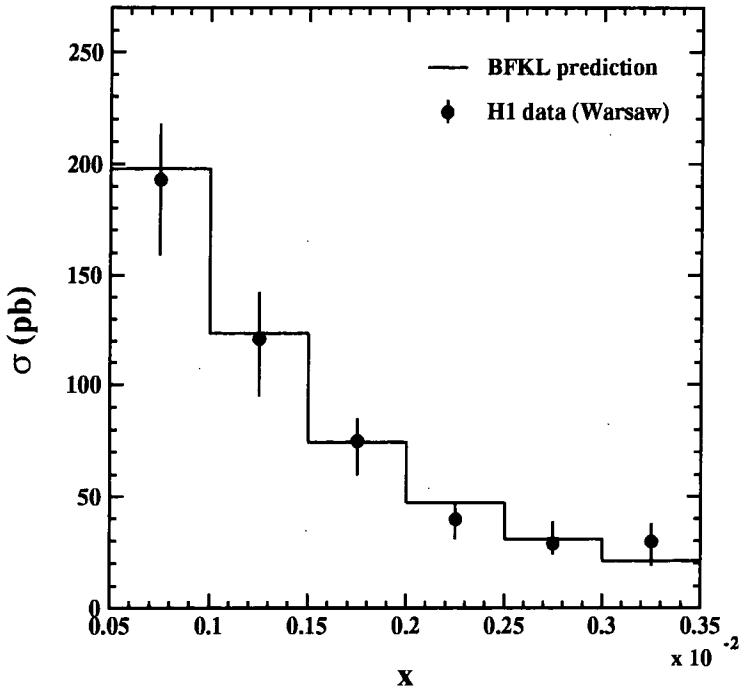

Figure 7.1: The deep inelastic + forward jet cross section in pb integrated over bins of size 5×10^{-4} in x compared to the H1 data [55]. The cuts for the forward jet are as imposed in the H1 measurement, that is $7° < \theta_j < 20°$, $E_j > 28.7$ GeV, and $k_{jT} > 3.5$ GeV. The electron acceptance region is defined by $160° < \theta'_{ep} < 173°$, $E'_e > 11$ GeV, and $y > 0.1$ in the HERA frame.

cuts which have been applied in the experiment. H1 require the outgoing lepton to obey

$$\begin{aligned} y &> 0.1 \\ 156° < \theta'_{ep} &< 173° \\ E'_e &> 12 \text{ GeV}. \end{aligned} \tag{7.1}$$

in the HERA (27.5×820 GeV) laboratory frame. The accessible (x, Q^2) range at HERA which corresponds to the cuts on y and θ'_{ep} is depicted in Fig. 7.2. This electron acceptance region can be compared with Fig. 3.8 in which we showed the (x, Q^2) range resulting from the cuts which we imposed in the computation of the DIS + π^0 rate in Chapter 5. The stronger limit on the energy E'_e of the outgoing electron, that is $E'_e > 12$ GeV rather than $E'_e > 5$ GeV, has the effect of reducing the small x and high Q^2 reach.

The kinematics of the DIS + π^0 process where displayed in Fig. 5.4. H1 select events

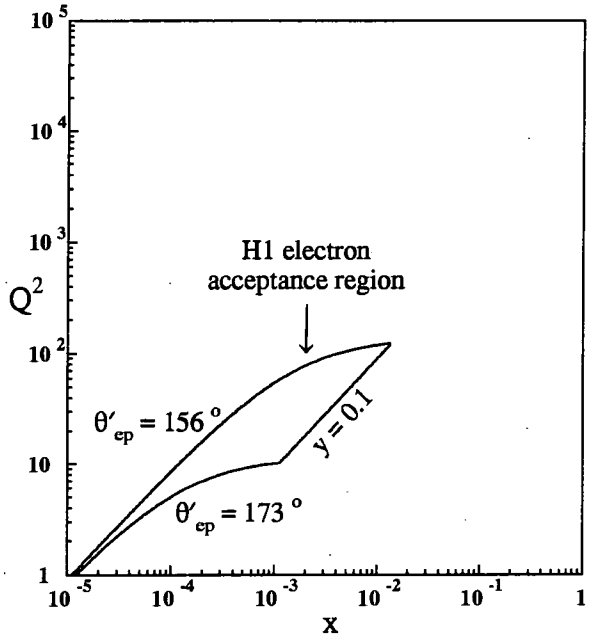

Figure 7.2: The acceptance region for the outgoing lepton defined by $0.1 < y < 1$ and $156° < \theta'_{ep} < 173°$ in the HERA (27.5 x 820 GeV) laboratory frame.

in which the π^0 fulfils the requirements

$$k_{\pi T} > 1 \text{ GeV} \tag{7.2}$$

$$5° < \theta_{\pi p} < 25° \tag{7.3}$$

$$E_\pi > 8 \text{ GeV}. \tag{7.4}$$

It should be noted here that the cut on the energy E_π of the π^0 corresponds approximately to $x_\pi > 0.0098$ whereas in Chapter 5 we required $x_\pi > 0.05$. H1 also presented data for $x_\pi > 0.012$, 0.015 and 0.017. The lower limit cut on the angle $\theta_{\pi p}$ of the π^0 with respect to the proton direction in the HERA frame is the beam pipe cut which we introduced in Section 5.4.2 in order to make the detection of the π^0's at HERA possible. In Chapter 5 we did not specify an explicit upper limit on $\theta_{\pi p}$, however, as explained in Section 5.4.1, we demanded that the π^0 is emitted in the proton hemisphere in the virtual photon - proton centre-of-mass frame. Looking at Fig. 5.5 we see that the hemisphere cut (5.28) corresponds approximately to $\theta_{\pi p} < 13°$ and therefore is more restrictive than the H1 angular cut. On the other hand, the H1 collaboration relaxes the cut on the transverse

momentum $k_{\pi T}$ of the jet compared to our requirement $k_{\pi T} > 3$ GeV in Chapter 5. Since the set of fragmentation functions [61] which we utilize in the computation of the DIS + π^0 cross section is only valid for scales greater than 2 GeV^2 most of the predictions shown in the remainder of this chapter were obtained for

$$k_{\pi T} > 1.5 \text{ GeV} \tag{7.5}$$

rather than 1 GeV (c.f. (7.2)) [8]. In Fig. 7.3 we show the accessible $(x_\pi, k^2_{\pi T})$ range which corresponds to the cuts listed in (7.3) – (7.5). The upper limit on $\theta_{\pi p}$ and the lower limit on E_π act as lower boundaries, whereas the lower limit on $\theta_{\pi p}$ describes the upper boundary. We already mentioned that the new set of cuts, (7.2) – (7.4), is less restrictive than the requirements we used in Chapter 5. From the experimental point of view this has the advantage that the rate is increased. Whether the H1 choice for the forward π^0 selection cuts is theoretically acceptable will be discussed later in this chapter.

As we explained in Section 5.3.2 we also impose the theoretical cut

$$x_\pi > 10x. \tag{7.6}$$

in addition to the requirements listed above. This cut insures that $z = x/x_j < 0.1$ since $x_j > x_\pi$. Recall that we require $z < 0.1$ for the BFKL formalism to be valid for the calculation of the DIS + forward jet cross section.

7.3 New predictions for the DIS + π^0 cross section

In this section our aim is to make absolute predictions for the DIS + π^0 cross section imposing the cuts given in (7.1) and (7.3) – (7.6) in the calculation. To obtain the rate we proceed as explained in Section 7.2. In particular we fix the normalisation of the BFKL functions Φ_i by requiring that the DIS + jet cross section computed with these Φ_i agrees

[8] We here rely on the validity of the collinear fragmentation approach for these small transverse momenta. This approach is based on the assumption that the intrinsic transverse momentum, i.e. the transverse momentum of the pion in a frame in which the fragmenting parton moves along the z direction, is very small. It is given by soft physics and its square is of the order of $k_T^2 \simeq 0.1$ GeV^2 which is still rather small compared to our smallest scale 1 GeV^2.

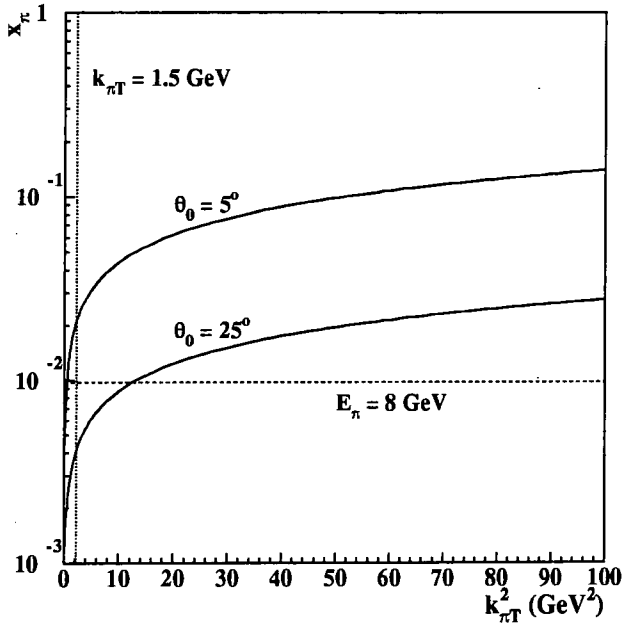

Figure 7.3: The accessible $(x_\pi, k^2_{\pi T})$ region defined by the cuts given in (7.3) - (7.5). The curves corresponding to $\theta_{\pi p} = \theta_0 = 25°$ (solid line) and $E_\pi = 8$ GeV (dashed line) represent the lower boundaries, whereas the solid curve for $\theta_0 = 5°$ describes the upper boundary. Also shown, as a dotted line, is the boundary defined by $k_{\pi T} > 1.5$ GeV. Note that the solid lines were calculated as for Fig. 5.5.

with the H1 data. This allows us to make an absolute prediction for the DIS + π^0 cross section.

7.3.1 Comparison of the DIS + π^0 cross sections obtained including and neglecting BFKL evolution

As in Chapter 5 we compare two types of predictions for the cross section for deep inelastic events containing an identified π^0. First we calculate this cross section including BFKL soft gluon resummation where we follow the procedure described above, then we neglect BFKL evolution and set $\Phi_i = \Phi_i^{(0)}$. In Fig. 7.4 we show the x dependence of the DIS + π^0 rate integrated over bins of size $\Delta x = 2 \times 10^{-4}$, $\Delta Q^2 = 10$ GeV^2 which are accessible at HERA. The π^0 was required to fulfil the constraints listed in (7.3) - (7.6), and the fragmentation functions were evaluated at scale $\mu^2 = k^2_{\pi T}$. Solid lines represent the predictions for the cross section obtained when including BFKL evolution in the computation

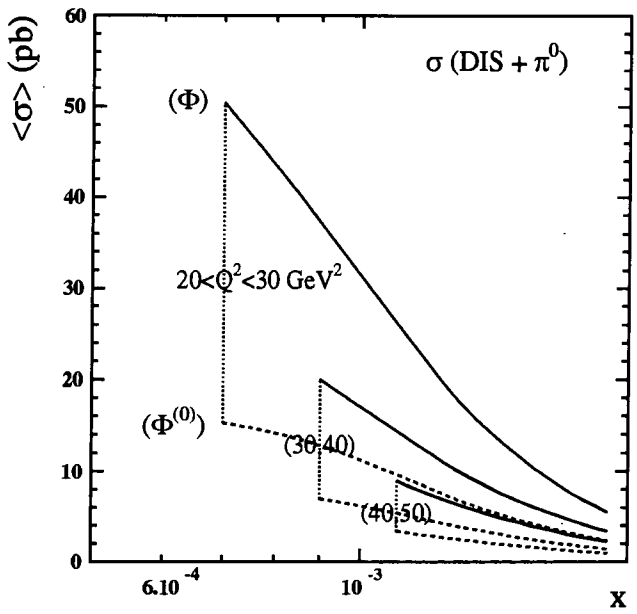

Figure 7.4: The cross section (in pb) for DIS + π^0 events integrated over bins of size $\Delta x = 2 \times 10^{-4}$, $\Delta Q^2 = 10$ GeV^2 which are accessible at HERA. The cuts listed in (7.1) and (7.3) – (7.6) were imposed in the calculation and the fragmentation functions were evaluated at scale $\mu^2 = k_{\pi T}^2$. The x dependence is plotted in the ΔQ^2 bins (20,30), (30,40) and (40,50) GeV^2 using the values of $\langle\sigma\rangle$ at the central x values in each Δx bin and joining them by straight lines. The solid curves show $\langle\sigma\rangle$ computed using Φ obtained from the BFKL equation whereas for the dashed curves BFKL soft gluon resummation was neglected and the quark box approximation $\Phi_i = \Phi_i^{(0)}$ utilized. Curves corresponding to the same ΔQ^2 bin are joined by a dotted vertical line.

for three different ΔQ^2 bins (20-30, 30-40 and 40-50 GeV^2). The corresponding results for $\Phi_i = \Phi_i^{(0)}$ are displayed as dashed lines. As we also saw in Fig. 5.6 BFKL resummation leads to a strong enhanced increase of the DIS + π^0 cross section. There we pointed out that it is this shape in x which should be used to identify BFKL effects. Here we fixed the normalisation of the BFKL functions Φ_i – and therefore the normalisation of the DIS + π^0 cross section – by comparing with the H1 DIS + forward jet data. This should allow us to not only focus on the x dependence but also on the absolute value of the rate. In Fig. 7.5 we show the DIS + π^0 cross section $\langle\sigma\rangle$ in pb calculated as for Fig. 7.4 in bins in x and Q^2 which are accessible at HERA when requiring the outgoing electron to lie in the region defined by (7.1). The numbers in the top row in each bin give $\langle\sigma\rangle$ calculated allowing for BFKL evolution, the numbers in brackets, on the other hand, were obtained neglecting BFKL resummation. This means that the difference between the two values in

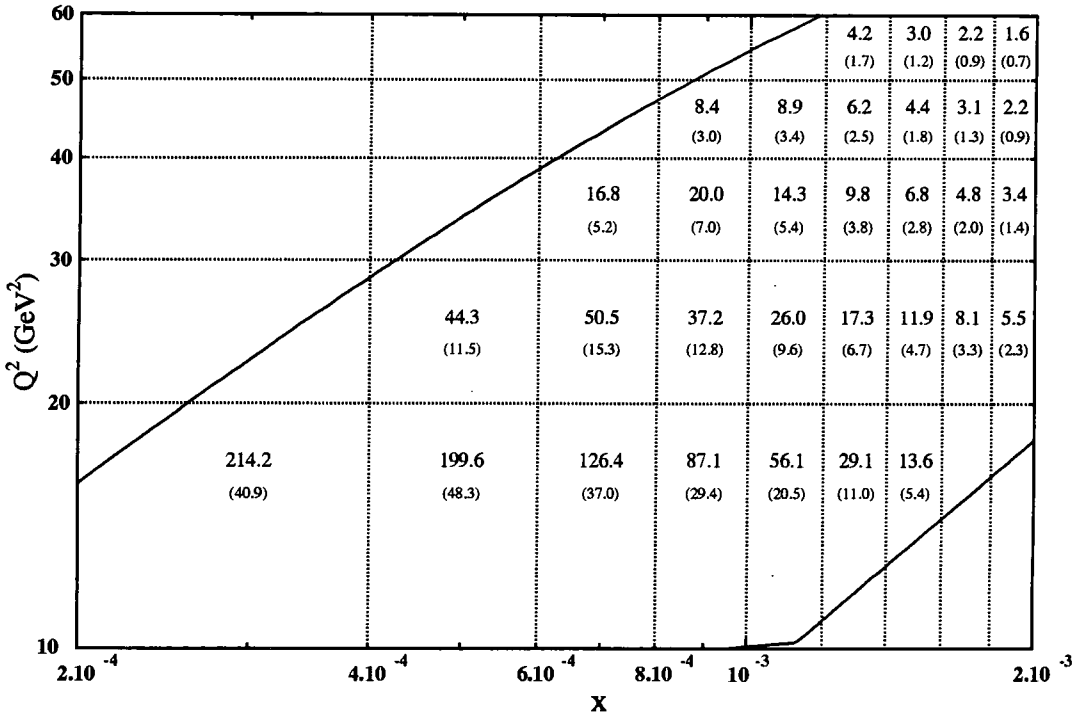

Figure 7.5: The DIS + π^0 cross section $\langle\sigma\rangle$ in pb in bins in x and Q^2 which are accessible at HERA. As for Fig. 7.4 the outgoing lepton was required to fulfil (7.1) and the π^0 (7.3) – (7.6). Again the fragmentation functions were evaluated at scale $\mu^2 = k_{\pi T}^2$. The values in brackets correspond to $\langle\sigma\rangle$ computed using the quark box approximation $\Phi_i = \Phi_i^{(0)}$. Shown as continuous lines are the boundaries on the acceptance region at HERA defined by $156° < \theta'_{ep} < 173°$ and $y > 0.1$.

one bin is a measure for the BFKL effect. Recall that because of equality (5.20) for the pion fragmentation functions the values given for the DIS + π^0 cross section correspond to the average of the cross sections for π^+ and π^- production.

7.3.2 A comment on the new cuts

As anticipated we will study the effect of the new cuts (7.3) – (7.5) on the DIS + π^0 cross section and investigate whether they are desirable from the theoretical point of view. Again we require that $k_{\pi T} > 1.5$ GeV rather than 1 GeV to ensure that the fragmentation functions are applicable.

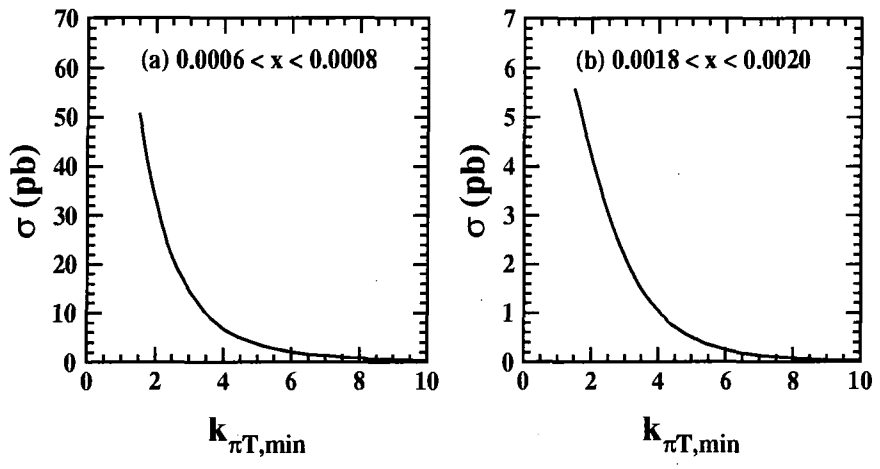

Figure 7.6: The DIS + π^0 cross section in the bins $20 < Q^2 < 30$ GeV^2 and (a) $6 \times 10^{-4} < x < 8 \times 10^{-4}$ and (b) $1.8 \times 10^{-3} < x < 2 \times 10^{-3}$. The fragmentation scale and cuts are as for Fig. 7.4 but we vary the lower limit $k_{\pi T,min}$ on the transverse momentum of the π^0.

The cut on the transverse momentum of the π^0

The results for the DIS + π^0 cross section which we presented in Figs. 7.4 and 7.5 were obtained requiring the transverse momentum of the π^0 to obey $k_{\pi T} > 1.5$ GeV whereas in Chapter 5 we demanded $k_{\pi T} > 3$ GeV. In Fig. 7.6 we show the effect on the DIS + π^0 cross section of varying the minimum allowed transverse momentum $k_{\pi T,min}$. We plot the $k_{\pi T,min}$ dependence of the cross section in bins with $20 < Q^2 < 30$ GeV^2 and (a) $6 \times 10^{-4} < x < 8 \times 10^{-4}$ and (b) $1.8 \times 10^{-3} < x < 2 \times 10^{-3}$. Comparing the values for $k_{\pi T,min} = 1.5$ GeV and $k_{\pi T,min} = 3$ GeV we see that relaxing the cut on $k_{\pi T}$ increases the rate by about a factor 3.5 in the lower x bin and a factor 2.6 in the higher x bin. So we see that lowering $k_{\pi T,min}$ is certainly advantageous from the experimental point of view. However, as becomes evident from Fig. 7.7, it has the side effect that the ratio of the cross sections obtained including and neglecting BFKL evolution becomes somewhat smaller, in other words, the BFKL effect is less visible. More important, there is a caveat from the theoretical point of view. Recall that as we explained one of the ideas behind the DIS + forward jet measurement is that jets are selected whose transverse momentum squared $k_{jT}^2 \simeq Q^2$. This implies that DGLAP evolution is neutralized. We imposed this constraint by requiring that $\frac{1}{2}Q^2 < k_{jT}^2 < 2Q^2$. For the DIS + π^0 process we cannot

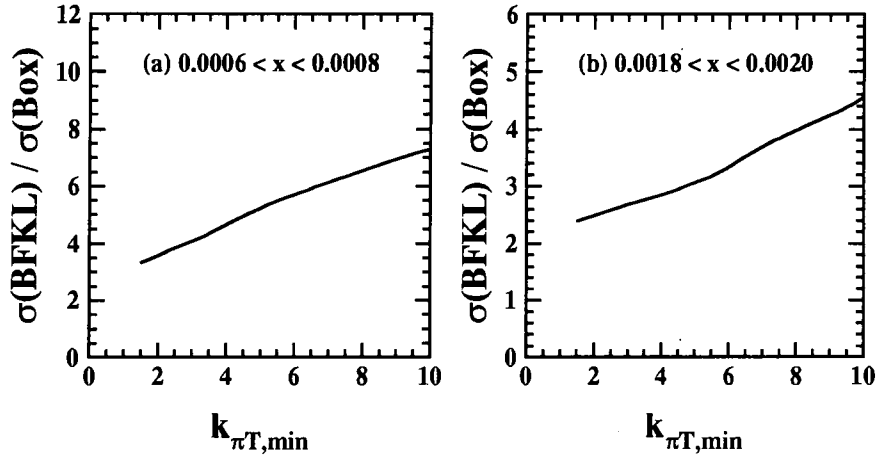

Figure 7.7: The ratio of the DIS + π^0 cross section calculated as for Fig. 7.6 and the cross section obtained when using the quark box approximation $\Phi = \Phi^{(0)}$. The results are shown for the bins defined by $20 < Q^2 < 30$ GeV^2 and (a) $6 \times 10^{-4} < x < 8 \times 10^{-4}$ and (b) $1.8 \times 10^{-3} < x < 2 \times 10^{-3}$.

introduce an explicit cut on k_{jT}^2 because the forward jet is not identified. There is only an implicit cut due to the kinematic constraint $k_{jT} > k_{\pi T}$. However, we still need the transverse momentum of the jet squared $k_{jT}^2 \simeq Q^2$ to safely neglect DGLAP evolution. Let us check what the lowest value of k_{jT}^2 is on average. We have $\langle k_{jT} \rangle = k_{\pi T}/\langle z_\pi \rangle$ where the average fraction of the parton jet's transverse and longitudinal momentum which the emitted π^0 carries $\langle z_\pi \rangle \simeq 0.4$. (For clarity we here use z_π instead of z as in Chapter 5.) This means that for $k_{\pi T} > 3$ GeV we have on average $k_{jT}^2 > 56$ GeV^2 which is of the right order for all Q^2 values which we considered in Fig. 7.5. If we take $k_{\pi T} > 1.5$ GeV then $k_{jT}^2 > 14$ GeV^2 on average which is somewhat low for the higher Q^2 bins. Note that here in principle k_{jT}^2 can be as small as 2.25 GeV^2. This value of k_{jT}^2 may even be too small for perturbation theory to be applicable. Therefore a higher luminosity would be desirable which would allow for a higher cut on $k_{\pi T}$ to be imposed while the DIS + π^0 rate would still be large enough for reasonable statistics.

The cut on the longitudinal momentum fraction of the π^0

Having investigated the new cut on the transverse momentum of the π^0 we now turn to studying the effect of relaxing the cut on its longitudinal momentum fraction x_π. In

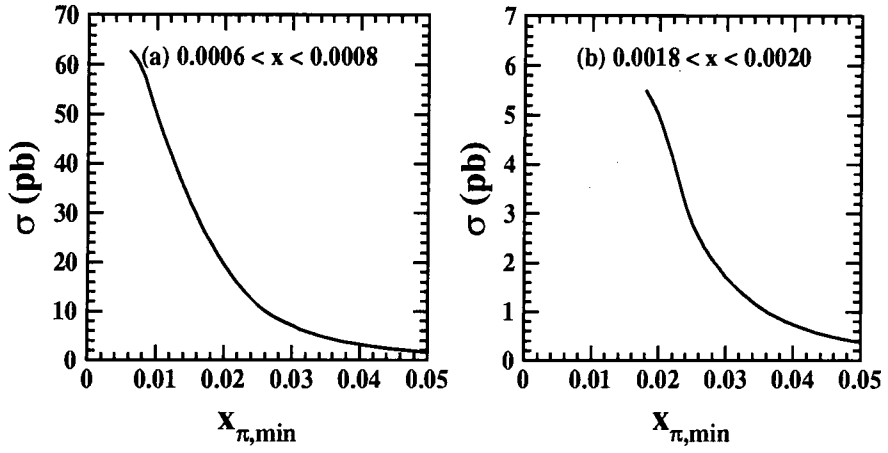

Figure 7.8: The DIS + π^0 cross section the bins $20 < Q^2 < 30$ GeV^2 and (a) $6 \times 10^{-4} < x < 8 \times 10^{-4}$ and (b) $1.8 \times 10^{-3} < x < 2 \times 10^{-3}$. We use the same fragmentation scale and cuts as for Fig. 7.4 but we vary the lower limit $x_{\pi,min}$ on the longitudinal momentum fraction of the π^0.

analogy to Fig. 7.6 we show in Fig. 7.8 the dependence of the DIS + π^0 cross section on the minimum allowed value $x_{\pi,min}$ of x_π. We plot the cross section integrated over the bins defined by $20 < Q^2 < 30$ GeV^2 and (a) $6 \times 10^{-4} < x < 8 \times 10^{-4}$ and (b) $1.8 \times 10^{-3} < x < 2 \times 10^{-3}$ calculated as for Fig. 7.4 but vary $x_{\pi,min}$. Recall that in Chapter 5 we required $x_\pi > 0.05$. If we instead demand $x_\pi > 0.01$ (corresponding approximately to $E_\pi > 8$ GeV) then we gain a factor of 31 in the rate in the lower x bin. For the higher x bin displayed in Fig. 7.8(b) lowering $x_{\pi,min}$ beyond 0.018 does not lead to an additional increase of the cross section due to the requirement (7.6). Therefore in this bin changing $x_{\pi,min}$ from 0.05 to approximately 0.01 only yields a factor of 15 in the rate. Nevertheless the increase of the cross section caused by the relaxation of the cut on x_π is considerable in both bins. On the other hand, smaller x_π means that x_j can be smaller due to the kinematic constraint $x_j > x_\pi$. This, however, implies that x/x_j is larger and therefore the evolution length for BFKL evolution is shorter. As a consequence the ratio between the results for the cross section obtained including and neglecting BFKL evolution in the calculation becomes smaller as $x_{\pi,min}$ is lowered. From Fig. 7.9 we see that in the bin limited by $6 \times 10^{-4} < x < 8 \times 10^{-4}$ the ratio of the two cross sections drops by a factor of 2 when $x_{\pi,min} \simeq 0.01$ rather than 0.05 is used. In the higher x bin where the lowest $x_{\pi,min}$ which can be reached is 0.018 the cross section ratio is reduced

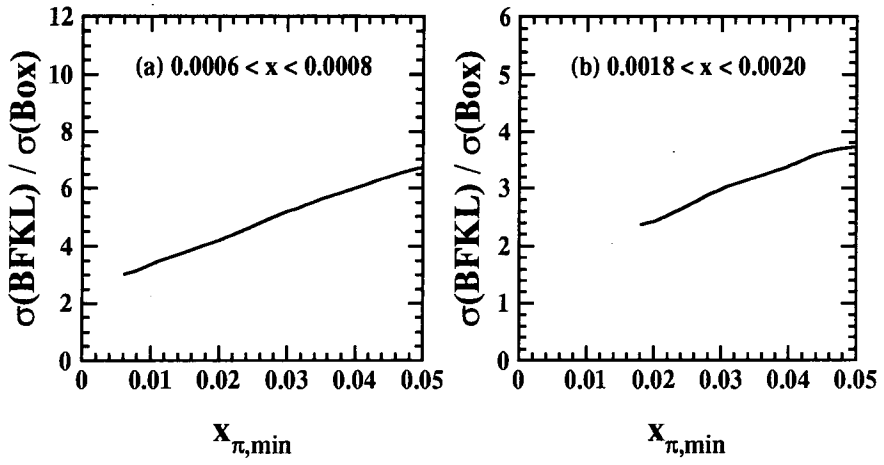

Figure 7.9: The ratio of the DIS + π^0 cross section calculated as for Fig. 7.8 and the cross section obtained when neglecting BFKL evolution ($\Phi = \Phi^{(0)}$). Again the results are shown for the bins defined by $20 < Q^2 < 30$ GeV^2 and (a) $6 \times 10^{-4} < x < 8 \times 10^{-4}$ and (b) $1.8 \times 10^{-3} < x < 2 \times 10^{-3}$.

by a factor 1.6. Comparing these factors with the factors 31 and 15 which we gained in the DIS + π^0 cross section in the lower and higher x bins, respectively, we notice that the reduced evolution length has a rather small effect. The strong increase of the rate towards lower $x_{\pi,min}$ is mainly due to the smaller values of $z_\pi = x_\pi/x_j$ which can be reached since the fragmentation functions fall rapidly with increasing z_π. The behaviour of the pion fragmentation functions which we used in the calculation of the DIS + π^0 cross section can for example be seen in Fig. 1(a) in ref. [61].

7.3.3 Comparison with the DIS + forward jet rate

In the previous subsection we saw by how much the DIS + π^0 cross section is increased when the cuts on the pion momenta are relaxed. Let us now investigate how the results for the DIS + π^0 cross section obtained for the new set of cuts given in (7.1) and (7.3) – (7.5) compare with the cross section for the DIS + forward jet process. Recall that we proposed the DIS + π^0 measurement as an alternative to DIS + jet because π^0's are easier to identify in an experiment. In fact, in the DIS + π^0 measurement events can be included where x_j is very large and the parent jet is lost in the proton beam pipe. In Chapter 5 we pointed out that π^0 production is suppressed by the fragmentation and

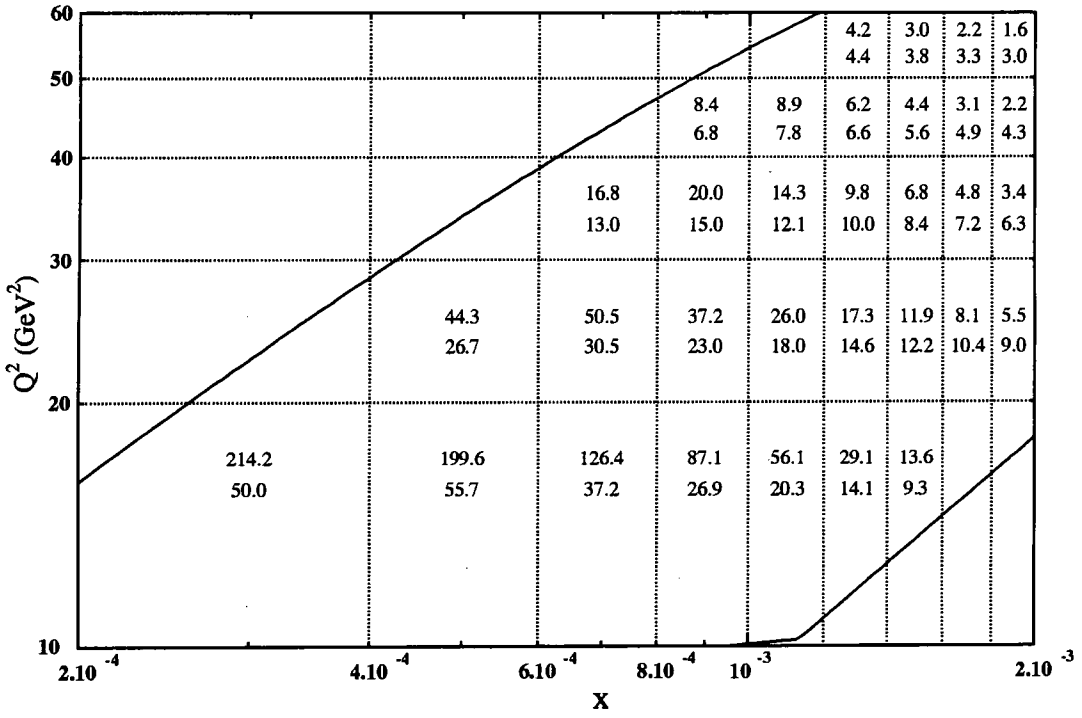

Figure 7.10: The upper and lower numbers correspond to the DIS + π^0 and the DIS + jet cross sections in pb, respectively. The results are shown in bins in x and Q^2 which are accessible at HERA. The DIS + π^0 cross section was calculated as for Fig. 7.5 and the DIS + jet cross section was obtained as for Fig. 7.1 but subject to the same electron acceptance region as the π^0 which is given in (7.1).

that it is an experimental issue whether the loss in signal can be compensated by the advantages of the new measurement.

To be able to compare the cross sections for the DIS + π^0 and the DIS + jet process we proceed in the following way. We calculate the DIS + π^0 rate as for Fig. 7.5 that is subject to the cuts on the outgoing lepton and the π^0 given in (7.1) and (7.3) – (7.6), respectively. Next we compute the DIS + jet rate as explained in Chapter 6. To be precise, we use the BFKL functions Φ_i which were normalized by comparing with the H1 forward jet data. We impose the cuts given in (6.2) and require $\frac{1}{2}Q^2 < k_{jT}^2 < 2Q^2$ where k_{jT} is the transverse momentum of the forward jet. The calculation only differs from the one presented in Chapter 6 in one point, namely the electron acceptance region. Rather than utilizing (6.1) we here demand that the outgoing electron fulfils the cuts listed in (7.1) so that we can compare the cross sections for the two processes in the same bins.

This does not affect the cross section in the bins in the centre of the accessible (x, Q^2) region at HERA. The resulting values for the DIS + jet cross section in pb are displayed as the numbers in the bottom rows in the bins in Fig. 7.10. The numbers shown in the top rows give the corresponding values for the DIS + π^0 cross section in pb. We see that for the new cuts (7.3) – (7.5) on the π^0 in the smaller x bins the DIS + π^0 cross section is now higher than the DIS + jet cross section. In the higher x bins the DIS + jet cross section is larger. For example for the bin defined by $6 \times 10^{-4} < x < 8 \times 10^{-4}$ and $20 < Q^2 < 30$ GeV^2 the ratio of the DIS + π^0 and the DIS + jet cross section is about 1.7, whereas in the bin with $1.8 \times 10^{-3} < x < 2 \times 10^{-3}$ and the same Q^2 range this ratio is 0.6. As was explained above and shown in Fig. 7.8 the smaller x the smaller $x_{\pi,min}$ can be in the DIS + π^0 measurement due to the requirement (7.6). Smaller $x_{\pi,min}$, however, implies that smaller values of z_π can be reached and therefore higher values of the fragmentation functions. That the two cross sections are comparable indicates that for the cuts given in (7.3) – (7.5) the DIS + π^0 cross section is large enough to be measured at HERA.

7.4 Comparison with the H1 data

The first DIS + π^0 measurement has in fact just been performed by the H1 collaboration [68]. In their analysis the scattered lepton was required to fulfil (7.1) and the π^0 the cuts given in (7.2) – (7.4). H1 present the data in the form $(dn_\pi/dx)/N$ where n is the multiplicity and N the total number of π^0's in the x interval under consideration. This x spectrum can be calculated from

$$\frac{1}{N}\frac{dn_\pi}{dx} = \frac{1}{\sigma_{tot}}\frac{\partial\sigma_\pi}{\partial x} \tag{7.7}$$

where $\partial\sigma_\pi/\partial x$ is obtained as explained in Section 7.2, but keeping the differential in x. In particular we again fix the normalisation of the BFKL prediction by demanding that the functions Φ_i utilized in the calculation allow for a description of the H1 DIS + jet data. The total differential cross section σ_{tot} is computed from the structure functions F_2 and F_L given by the MRS(R2) [21] set of parton distributions. We utilize (1.45) where we include the Q^2 dependence of $F_{2,L}$ and integrate over x and Q^2. Since in the experiment

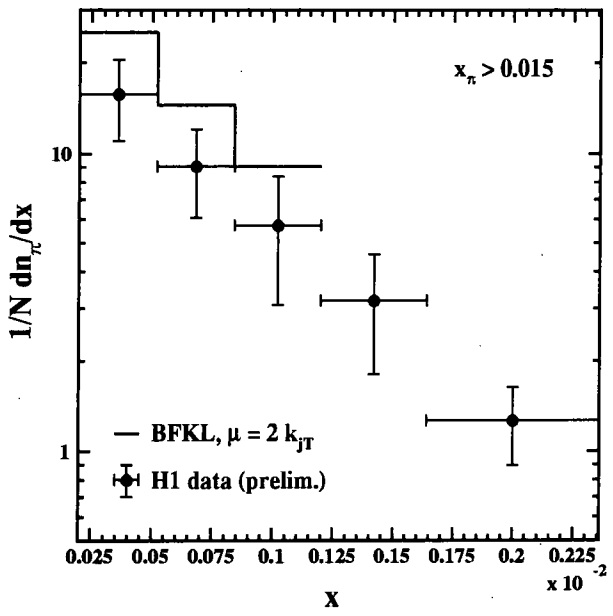

Figure 7.11: The forward π^0 spectra in x for the cuts given in (7.1) – (7.4) and $x_\pi > 0.015$. Note that here $k_{\pi T} > 1$ GeV. The prediction obtained from BFKL dynamics is depicted as a solid line. The fragmentation functions were evaluated at scale $\mu^2 = (2k_{jT})^2$ and the additional theoretical cut (7.6) was imposed. Also shown are the data points from the recent H1 measurement of the DIS + π^0 events [68].

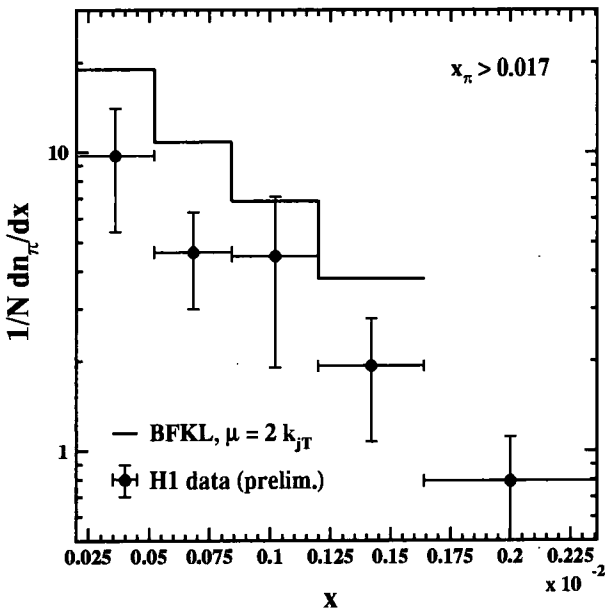

Figure 7.12: As Fig. 7.12, but for $x_\pi > 0.017$.

data is collected in bins in x we in practice use

$$\frac{1}{N}\frac{dn_\pi}{dx} = \frac{1}{\sigma_{tot}}\frac{\sigma_\pi}{\Delta x} \tag{7.8}$$

instead of (7.7) where Δx is the width of the x bin. The corresponding Q^2 range is determined by the electron acceptance region (7.1).

In Fig. 7.11 we show a comparison of the H1 DIS + π^0 data with the BFKL prediction obtained from (7.8). In addition to the cuts given in (7.1) - (7.4), the π^0 was here required to obey $x_\pi > 0.015$. The x range which determines N and σ_{tot} is $0.0002 < x < 0.00236$. In the BFKL calculation the fragmentation functions were evaluated at scale $\mu^2 = (2k_{jT})^2$. Note that the BFKL prediction does not extend over the whole x range of the data to avoid a violation of the theoretical cut (7.6) which ensures that the BFKL formalism is applicable. A comparison between the BFKL prediction and the H1 data is also shown in Fig. 7.12 where now $x_\pi > 0.017$. For both cuts on x_π the BFKL prediction overestimates the data. This may be due to the very low limits on x_π and $k_{\pi T}$. In Section 7.3.2 we explained that already $k_{\pi T} > 1.5$ GeV is rather low for our BFKL formalism to be valid. Of course, the situation is even worse for $k_{\pi T} > 1$ GeV where we may indeed be entering the non-perturbative region. As we also pointed out in Section 7.3.2 for small x_π small values of z_π may be reached where the fragmentation functions assume very high values so that the BFKL prediction is very sensitive to the lower limit on x_π. So higher limits on x_π and $k^2_{\pi T}$ would be desirable from the theoretical point of view. However, to ensure that the statistics in the measurement are reasonable a compromise between theory and experiment has to be found. Work on this subject is still in progress.

7.5 Summary and conclusions

In this chapter we returned to the DIS + π^0 measurement and, in response to the experimental observations [9], we updated the predictions we gave in Chapter 5. In Section 7.2.1 we explained how the DIS + π^0 cross section can be normalized by comparing with the H1 DIS + jet data. This allowed us to give an absolute prediction for the DIS + π^0 cross

[9]The measurements were motivated by our earlier calculations.

section rather than focussing only on its x dependence. In the calculation we imposed the cuts which have been used in a measurement by the H1 collaboration (although in most calculations we required $k_{\pi T} > 1.5$ GeV rather than 1 GeV). We obtained the DIS + π^0 rate including and neglecting BFKL evolution in the computation and saw the strong enhanced increase due to BFKL soft gluon resummation. Next we studied the effect on the cross section of varying the cuts on the longitudinal and transverse momentum of the π^0. We found that the requirement $k_{\pi T} > k_{\pi T,min} = 1.5$ GeV is somewhat too low for the BFKL formalism to be applicable. Also we saw that the DIS + π^0 rate is very sensitive to the choice of $x_{\pi,min}$. We pointed out that lowering this value below $10x$ does not lead to an additional increase of the rate. Lowering $x_{\pi,min}$ has the side effect that the ratio of the cross sections calculated from BFKL dynamics and using the quark box approximation is smaller which means that the BFKL effect is less clearly visible. In Section 7.3.3 we compared the prediction for the DIS + π^0 cross section with the DIS + jet cross section. We computed the DIS + jet rate subject to the cuts imposed in the H1 forward jet analysis but for the same electron acceptance region as in the DIS + π^0 measurement. We found that for the new cuts on the π^0 the cross sections for the two measurements are comparable. Finally we showed a comparison of the prediction for the π^0 spectrum in x as obtained from BFKL dynamics with the preliminary H1 data. It turned out that the BFKL prediction overestimates the data. The reason could be that the cuts on the pion momenta are too low. This can lead to the fragmentation functions being evaluated at very small values of z_π where they are not well determined. The fragmentation functions are also being used at very low scales where the perturbative approach may not be valid. So concerning the cuts a compromise between theoretical and experimental requirements will have to be found.

We conclude that if the cuts on the π^0 which we suggested in Chapter 5 are relaxed the DIS + π^0 cross section is large enough to be measured. However, care should be taken not to choose too small values for the cuts on the transverse and longitudinal momentum of the π^0. This is necessary to ensure that BFKL dynamics are indeed applicable and for BFKL effects to become apparent. A higher luminosity would allow for stronger cuts while keeping the DIS + π^0 rate large enough for reasonable statistics in the experiment.

Now that the DIS + π^0 rate can be measured at HERA this process should allow for a clearer identification of the underlying dynamics than the DIS + jet process for the following reasons. Firstly, experimentally π^0's are easier to identify than a jet close to the proton remnant, and secondly in DIS + π^0 both theory and experiment obtain the cross section on the hadron level so that no simulations of hadronisation effects are necessary, although of course we now have to rely on the validity of the fragmentation functions.

Chapter 8

Single particle spectra in deep inelastic scattering as a probe of small x dynamics

8.1 Focussing on the diffusion in $\ln k_T^2$ accompanying BFKL evolution

In the previous chapters we tried to identify $\ln(1/x)$ effects by focusing on the $x^{-\lambda}$ behaviour predicted by BFKL dynamics. We for example proceeded in this way when studying the DIS + jet process depicted in Fig. 8.1(a). However, besides the $x^{-\lambda}$ growth as x decreases along the BFKL ladder, a second characteristic feature is the diffusion in $\ln k_T^2$ where k_T are the transverse momenta of the gluons emitted along the chain. One way the diffusion manifests itself is in an enhancement of the transverse energy (E_T) flow in the central region between the current jet and the proton remnants [69], see Fig. 8.1(b). In principle the diffusion can enhance E_T from both the "upper" and "lower" BFKL gluon ladders, which are denoted by Φ and f in Fig. 8.1(b). However, the x reach at HERA is insufficient to fully develop the $\ln k_T^2$ diffusion in both ladders simultaneously. Nevertheless, the effect is quite appreciable giving at the *parton* level an energy flow $E_T \lesssim 2$ GeV/unit of rapidity. However the clean parton level prediction can in practice be masked or mimicked by the effects of hadronisation. Thus, although the prediction for E_T is in

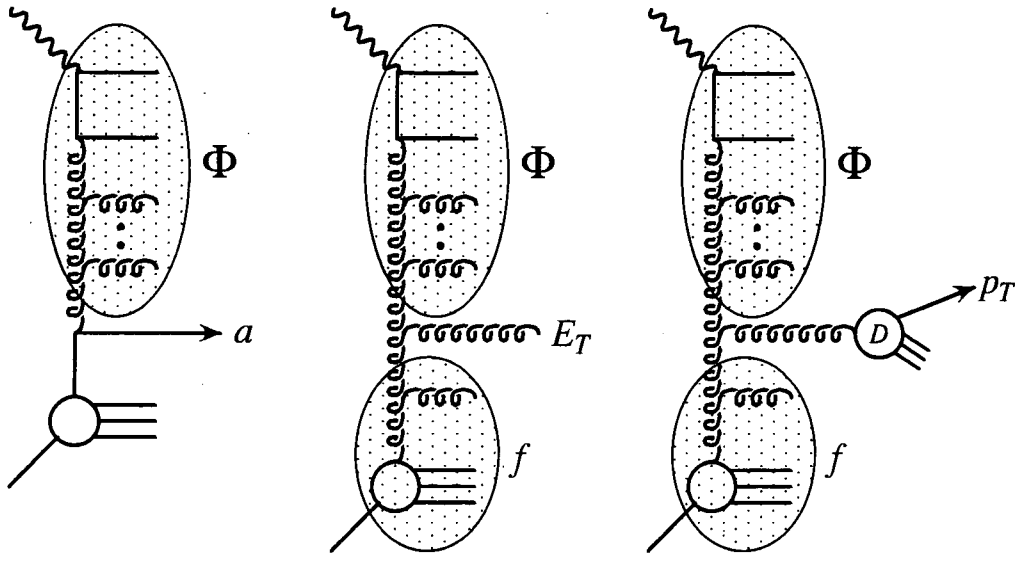

Figure 8.1: Diagrammatic representation of (a) the deep inelastic + forward jet, (b) the E_T flow, and (c) the single particle spectrum measurement.

agreement with observations [54] we cannot definitely conclude that it is due to $\ln(1/x)$ resummations.

An interesting way to overcome this ambiguity is to consider the emission of single particles at relatively large transverse momentum p_T in the central region away from the current jet and the proton remnants [70]. The process is shown diagrammatically in Fig. 8.1(c). The single particle spectrum at sufficiently large values of p_T should be much more immune from hadronisation and more directly reflect the $\ln k_T^2$ diffusion from the BFKL ladders. Basically the idea is that if DGLAP evolution is taking place the emission of a charged particle with high transverse momentum is suppressed by the fragmentation. If on the other hand BFKL gluon radiation is occuring then due to the random walk in transverse momentum along the ladder the production of a high-p_T particle is possible. Our aim in this chapter is to investigate whether BFKL effects can indeed be identified by studying single particle transverse momentum spectra at HERA.

We start with a discussion of the formalism for single particle production. In particular

we explain how we fix the normalisation of the BFKL prediction. Then we will proceed to describing how the cross section for charged particle production is calculated and how the p_T spectrum can be obtained from it. We will show predictions for the single particle spectra in bins in x and Q^2 and compare with data collected by the H1 collaboration. In Section 8.4 we discuss the p_T spectrum in a chosen bin in more detail and investigate the effect of changing the pseudorapidity interval in which the measurement is performed. The final section of this chapter contains our conclusions.

8.2 Formalism for charged particle production

To be able to make predictions for the single particle transverse momentum spectra we first have to calculate the cross section for the production of a charged particle in the central region. The process is depicted in Fig. 8.1(c).

8.2.1 Normalisation of the prediction

As we pointed out in Section 3.2.4 the normalisation of BFKL predictions is subject to uncertainties. In fact, even the shape is dependent on subleading $\ln(1/x)$ corrections. However, to be able to compare the BFKL result for the single particle spectrum with the experimental data we have to be able to make an *absolute* prediction. In Chapter 7 we were able to show an absolute prediction for the DIS + π^0 cross section by normalizing the solution Φ of the BFKL equation. This was done by requiring that the DIS + jet cross section as obtained from BFKL dynamics agrees with the H1 data. Here we can proceed in the same way since both the deep inelastic + jet and the charged particle production cross section depend on the same functions Φ_i as is shown symbolically in Fig. 8.1. To be precise, as outined in Section 7.2.1, we fix the "starting point" z_0 of the BFKL evolution by requiring that the DIS + jet cross section obtained with the resulting functions Φ_i describes the data. In Section 7.2.1 we found that the H1 data can be described best using the Φ_i calculated with $z_0 = 0.15$ and the infrared cutoff in the BFKL equations $k^2_{min} = 1$ GeV^2. We assumed a charm quark mass $m_c = 1.4$ GeV^2. In the following we

will see how the single particle spectrum can be computed utilizing these Φ_i.

8.2.2 The cross section for charged particle production

We first use Fig. 8.1(c) to obtain the differential cross section for the production of a hadron of transverse momentum p_T and longitudinal momentum fraction x_h. Then, in the following section, will we calculate the charged particle spectra relevant to the recent observations at HERA [71].

The cross section for single particle production is obtained by convoluting the inclusive cross section for the production of a single parton with the parton fragmentation function. That is we proceed analogously to how we calculated the DIS + π^0 rate from the DIS + jet rate in Chapter 5. The differential cross section for the inclusive production of a single parton of longitudinal momentum fraction x_j and transverse momentum k_{jT} has the generic form of (3.6). We have

$$\frac{\partial\sigma_j}{\partial x_j\,\partial k_{jT}^2\,\partial x\,\partial Q^2} = \frac{4\pi\alpha^2}{xQ^4}\left[(1-y)\frac{\partial F_2}{\partial x_j\,\partial k_{jT}^2} + \frac{1}{2}y^2\frac{\partial F_T}{\partial x_j\,\partial k_{jT}^2}\right]. \tag{8.1}$$

Now for small x, and in the central region away from the current jet and the proton remnants, we expect gluonic partons to dominate where the gluons are radiated within the BFKL ladder. The differential structure functions occurring in (8.1) are then given by

$$x_j\frac{\partial F_i}{\partial x_j\,\partial k_j^2} = \int\frac{d^2k_p}{\pi k_p^4}\int\frac{d^2k_\gamma}{k_\gamma^4}\left[\frac{\overline{\alpha}_S(k_j^2)\,k_p^2\,k_\gamma^2}{k_j^2}\right] \times f(x_j,k_p^2)\,\Phi_i\left(\frac{x}{x_j},k_\gamma^2,Q^2\right)\delta^2(k_j-k_p-k_\gamma) \tag{8.2}$$

with $i=T,L$ and where for simplicity we omitted the subscript T from the gluon transverse momenta, k_{jT}, k_{pT} and $k_{\gamma T}$, see Fig. 8.2. As before $\overline{\alpha}_S \equiv 3\alpha_S/\pi$. The expression in square brackets in (8.2) arises from the (square of the) BFKL vertex for real gluon emission, c.f. (2.23). Recall that above we fixed the normalisation of the BFKL functions Φ_i by comparing with the DIS + jet data. The function f in (8.2) is the unintegrated

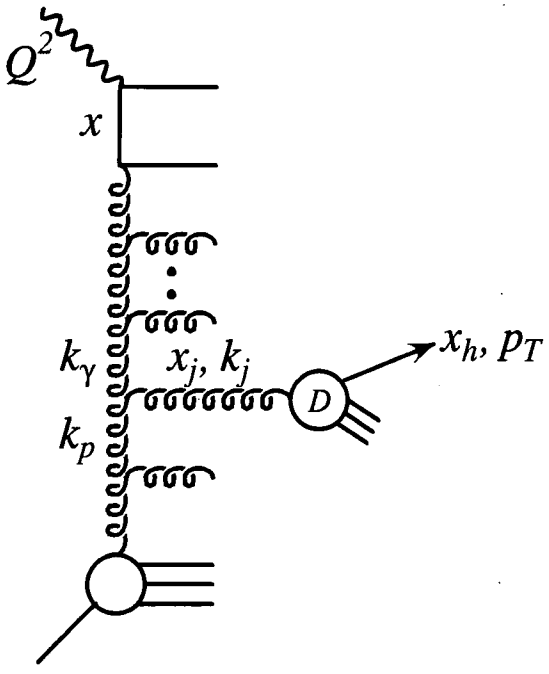

Figure 8.2: Diagrammatic representation of the cross section for emission of a high transverse momentum p_T particle.

gluon distribution in the proton which satisfies the BFKL equation

$$-z\frac{\partial f(z,k^2)}{\partial z} = \overline{\alpha}_S\, k^2 \int_0^\infty \frac{dk'^2}{k'^2}\left[\frac{f(z,k'^2)-f(z,k^2)}{|k'^2-k^2|} + \frac{f(z,k^2)}{\sqrt{4k'^4+k^4}}\right] \tag{8.3}$$

In practice we evolve (8.3) down in z from the boundary condition

$$f(\overline{z}_0,k^2) = f^{AP}(\overline{z}_0,k^2) = \frac{\partial\left[\overline{z}_0\, g^{AP}(\overline{z}_0,k^2)\right]}{\partial \ln(k^2/k_0^2)} \tag{8.4}$$

where here $z=\overline{z}_0$ with $\overline{z}_0 = 10^{-2}$, and where g^{AP} is the conventional gluon distribution obtained from a global set of partons. As before we allow the coupling to run, that is we take $\alpha_S(k^2)$ in (8.3). Moreover, we impose an infrared cut-off $k_0^2 = 1\text{GeV}^2$. That is we require the arguments of f to satisfy $k^2, k'^2 > k_0^2$. Similarly, the integrations in (8.2) are restricted to the regions k_p^2, $k_\gamma^2 > k_0^2$. We can include the contribution ΔF_i from the region $k_p^2 < k_0^2$ by assuming the strong ordering approximation, $k_p^2 \ll k_\gamma^2 \sim k_j^2$, at the gluon vertex. This contribution to (8.2) then becomes

$$x_j \frac{\partial(\Delta F_i)}{\partial x_j \, \partial k_j^2} = \overline{\alpha}_S(k_j^2) \int^{k_0^2} \frac{dk_p^2}{k_p^2} \frac{1}{k_j^4} f(x_j, k_p^2) \, \Phi_i\left(\frac{x}{x_j}, k_j^2, Q^2\right)$$
$$= \overline{\alpha}_S(k_j^2) \frac{x_j g(x_j, k_0^2)}{k_j^4} \, \Phi_i\left(\frac{x}{x_j}, k_j^2, Q^2\right). \tag{8.5}$$

Most of the time, however, for the calculation relevant to the HERA data, the variable x_j is not small enough for the BFKL equation to be applicable for the function f. In these cases, that is when $x_j > \overline{z}_0$, we therefore again assume strong ordering $k_p^2 \ll k_\gamma^2 \sim k_j^2$. In addition we include the contributions from quark and antiquark jets which we expect to contribute for the larger x_j values. We then obtain

$$x_j \frac{\partial F_2}{\partial x_j \, \partial k_j^2} = \overline{\alpha}_S(k_j^2) \frac{x_j \left[g + \frac{4}{9}\sum_q (q + \bar{q})\right]}{k_j^4} \, \Phi_i\left(\frac{x}{x_j}, k_j^2, Q^2\right). \tag{8.6}$$

where the parton distributions are to be evaluated at (x_j, k_j^2).

The differential cross section for single particle (h) production is obtained by convoluting the jet cross section with the fragmentation functions D for the parton $\rightarrow h$ transition

$$\frac{\partial \sigma_h}{\partial x_h \partial p_T^2 \partial x \partial Q^2} = \int_{x_h}^1 dz \int dx_j \int dk_j^2 \, \delta(x_h - z x_j) \delta(p_T - z k_j)$$
$$\times \left\{ \frac{\partial \sigma_g}{\partial x_j \partial k_j^2 \partial x \partial Q^2} D_g^h(z, \mu^2) + \right. \tag{8.7}$$
$$\left. + \frac{4}{9} \sum_q \left[\frac{\partial \sigma_q}{\partial x_j \partial k_j^2 \partial x \partial Q^2} D_q^h(z, \mu^2) + \frac{\partial \sigma_{\overline{q}}}{\partial x_j \partial k_j^2 \partial x \partial Q^2} D_{\overline{q}}^h(z, \mu^2) \right] \right\}$$

where σ_g and σ_q are the contributions to the cross section σ_j for gluon and quark and antiquark jets, respectively. The fragmentation scale μ^2 is of the order of k_j^2, and we will test the effect of varying it on the cross section later. The cross section for charged particle production is obtained by summing over all possible charged hadrons h.

8.3 Predictions for the single particle p_T spectra

In the following we will explain how the single particle spectrum can be calculated from the cross section for charged particle production which we obtained above. After discussing

the cuts imposed in the calculation we will be in the position to show our prediction for the p_T spectra and compare with the data.

8.3.1 Calculation of the single particle spectrum

The data for the single (charged) particle p_T spectra are presented in the form $(dn/dp_T)/N$ where n is the multiplicity and N the total number of charged particles in a given x, Q^2 bin [71]. To calculate this p_T spectrum we evaluate

$$\frac{1}{N}\frac{dn}{dp_T} = \left(\sum_h \frac{\partial\sigma_h}{\partial p_T\,\partial x\,\partial Q^2}\right) \Big/ \frac{\partial\sigma_{tot}}{\partial x\,\partial Q^2}\,. \tag{8.8}$$

where $\partial\sigma_h/\partial p_T \partial x \partial Q^2$ is obtained from (8.7) by integrating over x_h. We take the central values of x, Q^2 in the bin. The integration limits are fixed by the limits on the pseudorapidity interval under consideration. To be precise we use

$$x_h = \sqrt{\frac{x}{Q^2}}\, p_T\, e^{-\eta} \tag{8.9}$$

where η is the pseudorapidity of the charged particle, $\eta = -\ln\tan(\theta/2)$ with θ the angle with respect to the virtual photon direction. Finally we calculate the total differential cross section $\partial\sigma_{tot}/\partial x \partial Q^2$ in (8.8) from the structure functions F_2 and F_L given by the MRS(R2) [21] set of parton distributions.

As explained in the previous section, our aim is to make an absolute BFKL-based prediction to compare with the p_T spectra observed by the H1 collaboration. We fix the parameters occurring in the calculation of the BFKL functions Φ_i by requiring the prediction for the DIS + jet cross section to give the correct normalisation of the H1 forward jet measurements. The next step is to use the functions Φ_i obtained in this way in the computation of the differential structure functions from (8.2), (8.5) and (8.6). In this way we are able to calculate a normalized p_T spectrum from (8.8).

Neglecting BFKL evolution

The BFKL prediction for the single particle spectra may be compared with the result which would be obtained if the BFKL gluon radiation is neglected. That is in (8.2), (8.5)

and (8.6) we replace the functions Φ_i which describe the solution of the BFKL equation with the boundary condition given by the quark box with the quark box $\Phi_i^{(0)}$ only. In addition we now also assume strong ordering for $x_j < \overline{z}_0$ and carry out the k_p^2 integration in (8.2). This amounts to assuming that in a fixed-order treatment the dominant subprocess is $\gamma g \to q\overline{q}g$. In our calculation the κ integration is infrared finite since we allow for the virtuality of both the gluon and the photon.

8.3.2 Comparison with the H1 data

We are now in the position to give a BFKL prediction for the single particle spectra which can be compared with the H1 data. In their measurement [71] the H1 collaboration collected data in nine different kinematic bins in two pseudorapidity intervals. We will focus on the three smallest x bins where BFKL effects should become visible. Also we will only show results for the lower pseudorapidity interval, $0.5 < \eta < 1.5$, where we expect no contamination due to the fragmentation of the current jet which has not been included in the calculation. We subtract 10% off the total cross section σ_{tot} to account for diffractive events with large rapidity gaps which have been excluded from the measurement. Finally, in the sum over the charged hadrons h in (8.8) we include $\pi^{\pm}$ and $K^{\pm}$, and we use the next-to-leading order fragmentation functions by Binnewies et al. [61].

Electron acceptance region

In the calculation of the p_T spectra we use $E_e = 27.5$ GeV and $E_p = 820$ GeV and impose the cuts which where used in the H1 measurement. That is we require the outgoing electron to lie in the region

$$\begin{aligned} y &> 0.05 \\ 157^\circ < \theta'_{ep} &< 173^\circ \\ E'_e &> 12 \text{ GeV} \end{aligned} \tag{8.10}$$

in the HERA laboratory frame. The cuts on y and θ'_{ep} define a region in (x, Q^2) which is shown in Fig. 8.3.

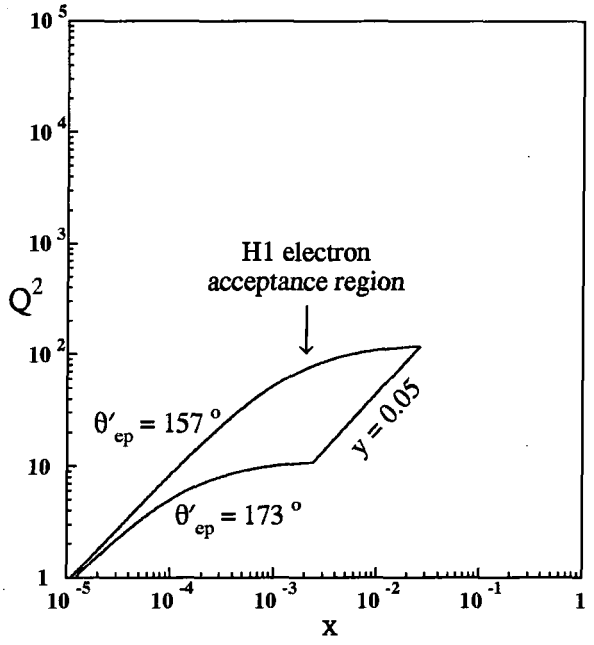

Figure 8.3: The acceptance region for the scattered electron specified by $0.05 < y < 1$ and $157° < \theta'_{ep} < 173°$ in the HERA laboratory frame.

Results

We now show the predictions for the single particle spectra obtained as described above and test if they agree with the H1 data. In Fig. 8.4 we plot predictions for the charged particle p_T spectrum in kinematic bin 1 of the H1 analysis with central values $x = 1.6 \times 10^{-4}$ and $Q^2 = 7$ GeV^2. We compare the results when BFKL small x resummation is included in the calculation with the case when gluon radiation is neglected in the way described above. In both cases we demonstrate the effect of changing the fragmentation scale from $\mu^2 = k_j^2$ to $\mu^2 = (2k_j)^2$. We see that the BFKL prediction gives a good description of both the shape and the normalisation [10] of the H1 data. On the other hand, when the BFKL effects are neglected the predictions lie considerably below the data. We are particularly interested in the shape of the spectrum in p_T. Recall that the idea behind the measurement of the p_T spectra is that in DGLAP evolution the transverse momenta

[10] Even though we have normalised Φ to the DIS + jet data, there still remains some residual uncertainty in the overall normalisation associated with the choice of infrared cut-off used in the k_γ integration in (8.2). Our results are shown for the natural choice $k_{\gamma 0}^2 = 1$ GeV^2.

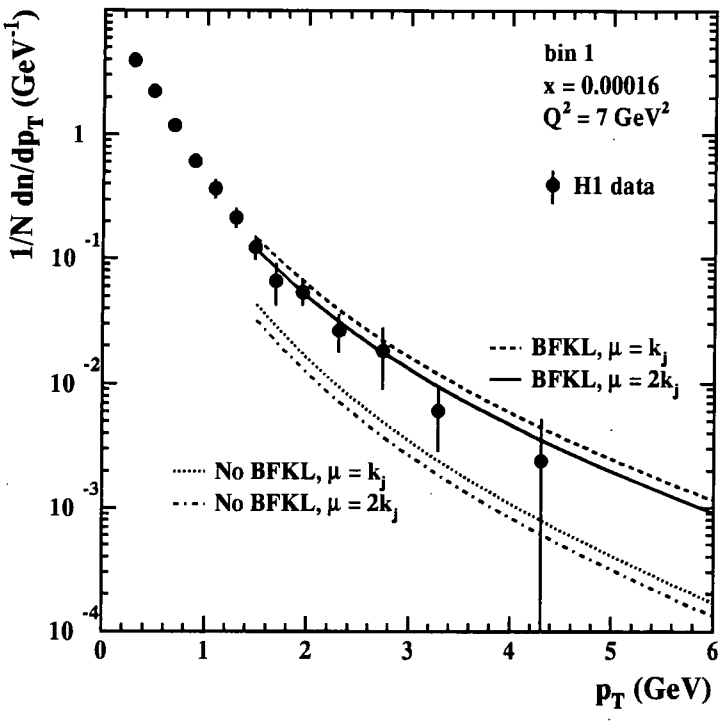

Figure 8.4: The transverse momentum spectrum of charged particles (π^+, π^-, K^+, K^-) in the pseudo-rapidity interval $0.5 < \eta < 1.5$ in the virtual photon-proton centre-of-mass frame. The results are shown for kinematic bin 1 with the central values $x = 1.6 \times 10^{-4}$ and $Q^2 = 7$ GeV^2. The continuous and the dashed curve show the spectra obtained with Φ_i and f calculated from the BFKL equation. They only differ in the choice of fragmentation scale: for the continuous curve the fragmentation functions were evaluated at scale $\mu^2 = (2k_j)^2$ and for the dashed curve at scale $\mu^2 = k_j^2$. When BFKL radiation is neglected in the calculation of the p_T spectra, i.e. when the quark box approximation $\Phi_i = \Phi_i^{(0)}$ is used and strong ordering at the gluon vertex is assumed, then the dash-dotted and dotted curves are obtained. The fragmentation functions were evaluated at scales $\mu^2 = (2k_j)$ and k_j^2 respectively. The data points shown are from the H1 measurement of the charged particle spectra [71].

are strongly ordered along the gluon chain which means that a gluon jet in the central region should have comparably small transverse momentum. In this case the emission of a high-p_T particle is suppressed by the fragmentation functions. BFKL evolution on the other hand is accompanied by a random walk in the transverse momentum of the gluons along the chain. This implies that high-p_T gluon jets can be emitted leading to a tail in the spectrum at larger p_T. Looking at Fig. 8.4 we indeed see that the spectrum decreases more rapidly with p_T when BKFL evolution is neglected than when the BFKL resummation is included. For example for $p_T = 1.5$ GeV the two predictions differ by

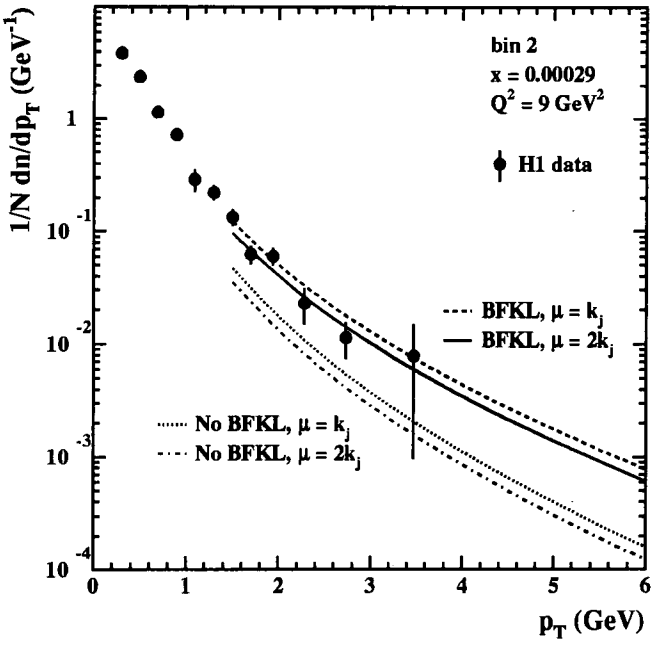

Figure 8.5: As Fig. 8.4, but for kinematic bin 2, $x = 2.9 \times 10^{-4}$ and $Q^2 = 9$ GeV^2.

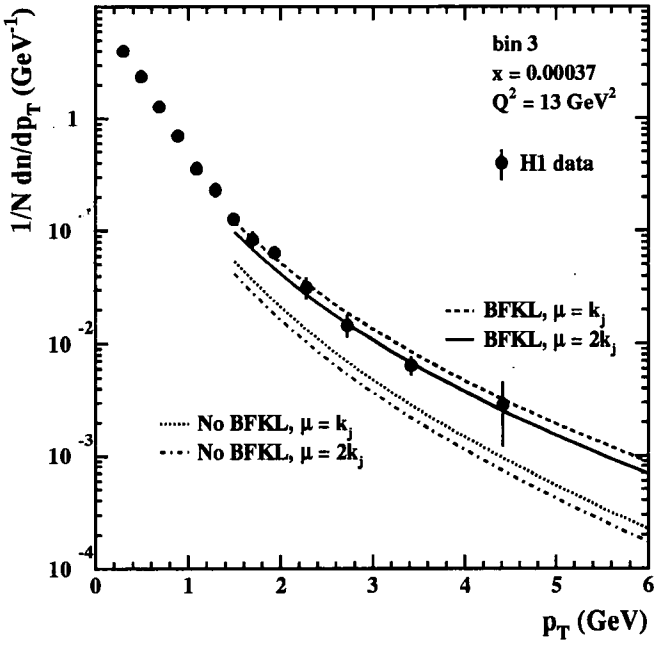

Figure 8.6: As Fig. 8.4, but for kinematic bin 3, $x = 3.7 \times 10^{-4}$ and $Q^2 = 13$ GeV^2.

a factor 3.6, whereas for $p_T = 6$ GeV this factor is almost 10. This is a reflection of the diffusion in $\ln k_T^2$ along the BFKL ladder. From Fig. 8.4 we also notice that the effect of varying the fragmentation scale by a reasonable factor is small compared to the difference between the BFKL-based predictions and the ones where BFKL resummation was neglected.

The same general behaviour as in Fig. 8.4 is seen in Figs. 8.5 and 8.6 where we show the comparison for kinematic bins 2 and 3, with central values $x = 2.9 \times 10^{-4}$, $Q^2 = 9$ GeV^2 and $x = 3.7 \times 10^{-4}$, $Q^2 = 13$ GeV^2, respectively. We find that in all three small x bins of the H1 analysis the data strongly support the inclusion of BFKL resummation in the calculation of the p_T spectra. Reasonable variations of the fragmentation scale do not allow for a description of the data when BFKL effects are neglected.

8.4 A closer look at the single particle p_T spectra

Having shown predictions for the single particle spectra our aim is now to investigate the p_T spectrum in a particular bin in more detail.

8.4.1 Contributions to the spectrum from the three different regions

Above, in Section 8.2.2, we explained how we calculate the differential structure functions $\partial F_i/\partial x_j \partial k_j^2$ $(i = T, L)$. Expression (8.2) for the differential structure functions is only applicable in the region where $x_j < \overline{z}_0$ and $k_p^2 > k_0^2$. In this case there are two BFKL ladders as shown in Fig. 8.1(c), to be precise we obtained Φ and f by solving BFKL equations. Next we considered the region where $x_j < \overline{z}_0$ but now $k_p^2 < k_0^2$. Here we assumed that the transverse momenta of the gluons at the triple gluon vertex are strongly ordered, that is $k_p^2 \ll k_\gamma^2 \sim k_j^2$. This allowed us to perform the k_p^2 integration leaving us with one BFKL ladder, Φ, only. The resulting contribution to the differential structure functions is given by (8.5). Finally we pointed out that most of the time $x_j > \overline{z}_0$. In this case we again use the strong ordering approximation and evaluate the k_p^2 integral. Then

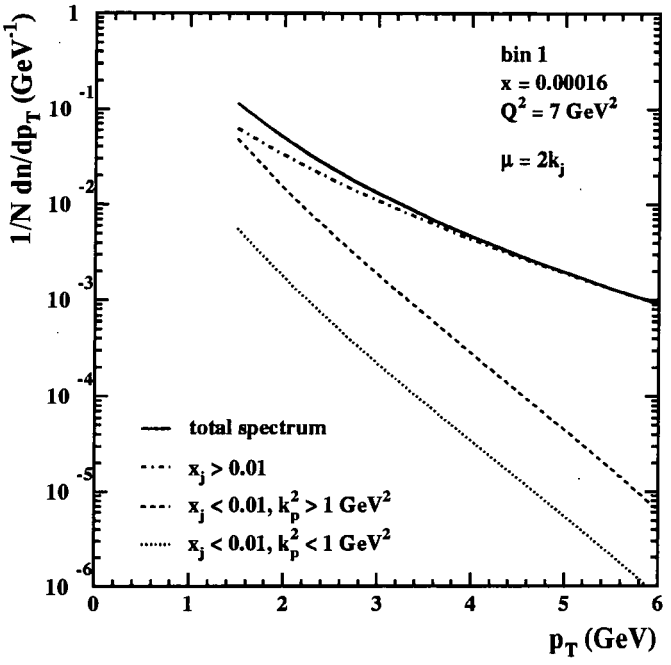

Figure 8.7: Contributions to the single particle spectrum in kinematic bin 1 with the central values $x = 1.6 \times 10^{-4}$ and $Q^2 = 7$ GeV^2. Shown as a solid line is the total spectrum calculated as for Fig. 8.4 including BFKL resummation in the calculation and evaluating the fragmentation functions at scale $\mu^2 = (2k_j)^2$. Dash-dotted and dotted lines represent the contributions from the regions $x_j > 10^{-2}$ and $x_j < 10^{-2}$, $k_p^2 < 1$ GeV^2, respectively. In these cases only one BFKL ladder, Φ, is included. Two BFKL ladders, Φ and f, contribute to the differential structure functions – and therefore the p_T spectrum – in the region $x_j < 10^{-2}$, $k_p^2 > 1$ GeV^2, as is displayed as a dashed line.

we are left with the BFKL ladder starting from the quark box (Φ) only, and the F_i are described by (8.6). Here we also included the contributions from quark and antiquark jets. Note that expression (8.6) for the differential structure functions is the same as for the deep inelastic + jet process depicted in Fig. 8.1(a), c.f. eqn. (3.7).

In Fig. 8.7 we show the contributions of the three different regions which we just discussed to the single particle spectrum in kinematic bin 1 with $x = 1.6 \times 10^{-4}$ and $Q^2 = 7$ GeV^2. As before we used $\overline{z}_0 = 10^{-2}$ and $k_0^2 = 1$ GeV^2. The total spectrum which is represented by a solid line is calculated as for Fig. 8.4 including BFKL evolution and choosing the fragmentation scale $\mu^2 = (2k_j)^2$. From Fig. 8.7 we see that the main contribution to the spectrum shown as a dash-dotted line comes from the region where $x_j > \overline{z}_0 = 10^{-2}$. Recall that in this case we only have BFKL evolution starting from the

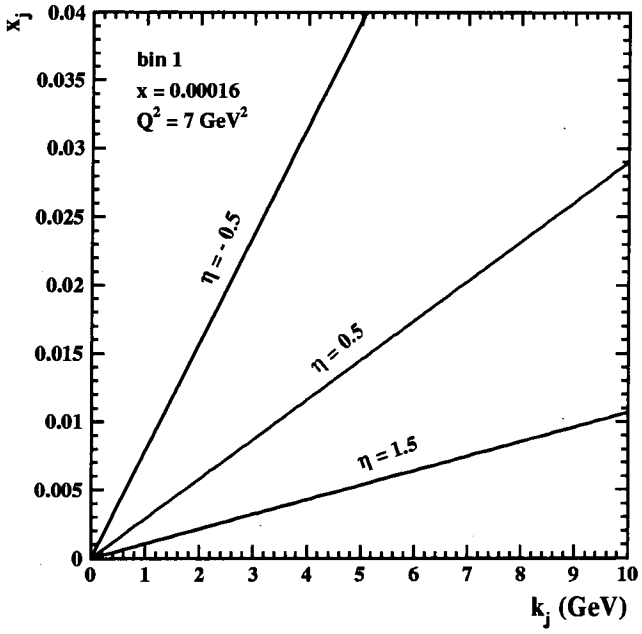

Figure 8.8: The relation between the jet kinematic variables for fixed values of the pseudorapidity η in the virtual photon – proton centre-of-mass frame. The results are shown for kinematic bin 1 with $x = 1.6 \times 10^{-4}$ and $Q^2 = 7$ GeV^2.

quark box. Represented by a dashed line is the contribution to the p_T spectrum from the region where $x_j < \overline{z}_0$ and $k_p^2 > k_0^2 = 1$ GeV^2. Here two BFKL ladders, Φ and f, are included in the calculation. We see that this region is only important for the small values of p_T. The contribution from the third region, $x_j < \overline{z}_0$ and $k_p^2 < k_0^2$, is always small. In the following we will present a brief explanation for why the main part of the p_T spectrum in the region $0.5 < \eta < 1.5$ comes from the region $x_j > 10^{-2}$.

8.4.2 The pseudorapidity interval

The results for the charged particle p_T spectra shown above where obtained in the pseudorapidity interval $0.5 < \eta < 1.5$ in the virtual photon – proton centre-of-mass frame. In analogy to (8.9) we can find an expression for the longitudinal momentum fraction x_j of the jet in terms of its transverse momentum k_j and the pseudorapidity η. We have

$$x_j = \sqrt{\frac{x}{Q^2}}\, k_j\, e^{-\eta}. \tag{8.11}$$

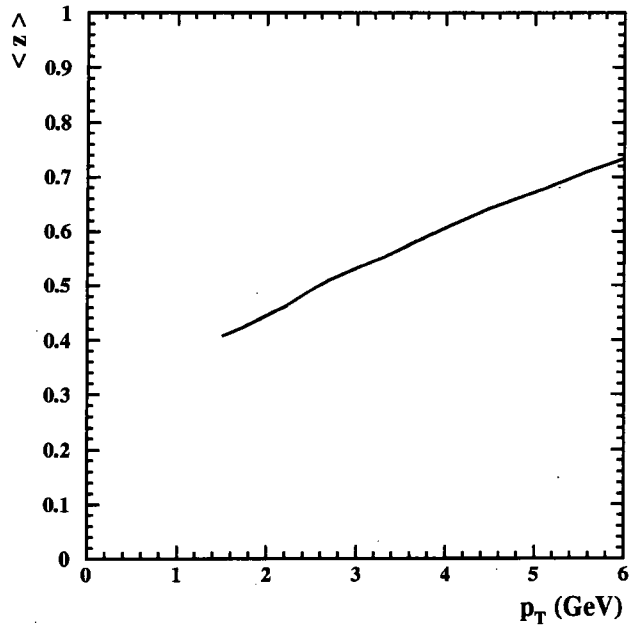

Figure 8.9: The average value of the fraction z of the parton jet's momentum which the emitted hadron carries away versus the transverse momentum p_T of the hadron.

In a given (x, Q^2) bin we are then able to compute the relation between the jet kinematic variables for fixed η. In Fig. 8.8 we show this relation for different values of η. The lines corresponding to $\eta = 0.5$ and $\eta = 1.5$ represent the boundaries on the accessible (x_j, k_j) region in the calculation of the p_T spectra presented above.

In Fig. 8.9 we plot the average value of z versus p_T. Recall that z is the fraction of the parton jet's momentum which the emitted hadron h carries away, $z = x_h/x_j = p_T/k_j$ assuming collinear fragmentation. We see that for the intermediate values of p_T, $p_T \simeq 3$ GeV, the hadron's transverse momentum is on average $p_T \simeq k_j/2$. This means that, for example, a hadron with $p_T = 3$ GeV originates from a parton with $k_j \simeq 6$ GeV. Returning to Fig. 8.8 we find that already for this comparably small value of p_T, $x_j > 10^{-2}$ most of the time.

As we saw, the main contribution to the single particle spectrum in the pseudorapidity interval $0.5 < \eta < 1.5$ is due to events where the parton jet has a longitudinal momentum fraction $x_j > 10^{-2}$. This implies that most of the time only one BFKL ladder is involved in the calculation of the cross section. In this case BFKL evolution starts from the quark

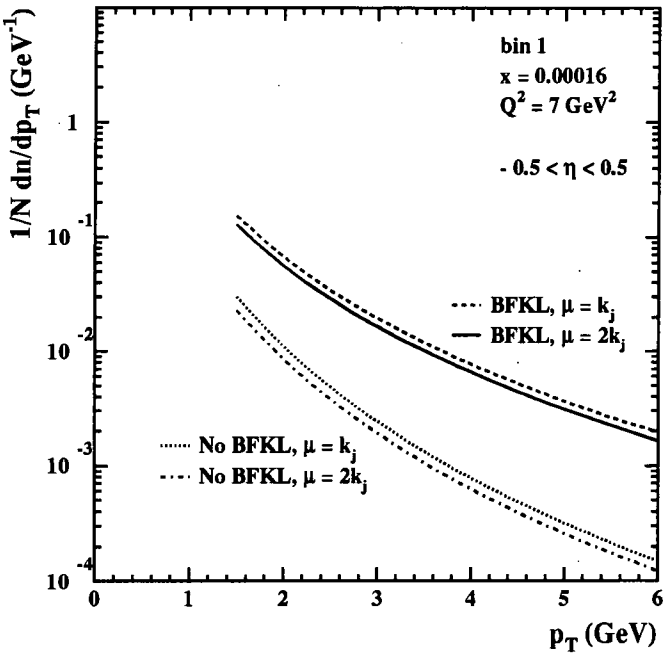

Figure 8.10: The transverse momentum spectrum of charged particles (π^+, π^-, K^+, K^-) in the pseudorapidity interval $-0.5 < \eta < 0.5$ in the virtual photon-proton centre-of-mass frame, otherwise as for Fig. 8.4.

box with the solution of the BFKL equation given by Φ. We notice that this means that we could consider a pseudorapidity interval which is closer to the proton direction, namely $-0.5 < \eta < 0.5$. The boundaries on the accessible (x_j, k_j) range which correspond to these limits on η are shown in Fig. 8.8. We see that here values of $x_j < 10^{-2}$ can only be reached for the smallest values of p_T. Focussing on the region $-0.5 < \eta < 0.5$ has the advantage that a longer BFKL evolution starting from the quark box is possible making the difference between the BFKL-based prediction and the approximate fixed order result more clearly visible. One the other hand we do not lose much by allowing for less BFKL evolution from the proton end because, as we pointed out above, already for $0.5 < \eta < 1.5$ the contribution from the region where two BFKL ladders are involved in the calculation is small for the higher values of p_T. In Fig. 8.10 we plot the single particle spectrum computed as for Fig. 8.4 but in the new pseudorapidity interval, $-0.5 < \eta < 0.5$. As before we compare the BFKL prediction with the case where BFKL radiation is neglected and try varying the fragmentation scale. We see that now for $p_T = 6$ GeV the difference

between the BFKL curve for one fragmentation scale and the corresponding "no BFKL" curve is about a factor of 15. So BFKL effects indeed become more apparent in this η-range.

8.5 Conclusion

In Chapter 6 we studied the DIS + forward jet process including massive charm in the quark box and solving the BFKL equation numerically for running coupling. We found that BFKL dynamics describe the shape of the x distribution of the HERA data well. Here we used these data to fix the normalisation of the solution of the BFKL equation with the boundary condition given by the quark box. This enabled us to give an absolute prediction for charged particle transverse momentum spectra at small x. We calculated the spectrum for large values of p_T first including BFKL small x resummation in the calculation and second neglecting gluon radiation. It turned out that the BFKL prediction shows excellent agreement with the H1 data both in shape and normalisation, whereas the approximate fixed order result underestimates the data and decreases too rapidly with p_T. We therefore conclude that we found evidence for the existence of $\ln(1/x)$ effects and for the diffusion in $\ln k_T^2$ which accompanies BFKL evolution. Despite these encouraging results it would, however, still be useful to compare the BFKL prediction for the p_T spectrum with the result of the complete fixed order calculation. Experimental data for higher values of p_T would allow an even clearer distinction between the different predictions. BFKL effects would also become more apparent in the pseudorapidity interval $-0.5 < \eta < 0.5$ which corresponds to higher values of x_j and therefore to a longer BFKL evolution starting from the quark box. Of course higher x_j also means less BFKL evolution from the proton end. This is, however, not a disadvantage, since already for the pseudorapidity interval which we considered the main contribution to the spectrum comes from the region $x_j > \overline{z}_0$. We conclude that more experimental data especially for higher values of p_T would be useful. Nevertheless, as can be seen from Figs. 8.4 – 8.6, the existing spectra already show the presence of BFKL effects at small x at HERA.

Chapter 9

Summary and conclusions

In this thesis we addressed the problem of whether $\ln(1/x)$ effects are observable in the small x region accessible in the present experiments at the DESY electron – proton collider HERA. We explained that the DGLAP equation resums the $\alpha_S^n \ln^n(Q^2/Q_0^2)$ terms in the perturbative expansion whereas the BFKL equation resums the $\alpha_S^n \ln^n(1/x)$ contributions. While it is clear that the DGLAP equation is valid if x is large and that the BFKL equation is appropriate when x is small, it is not obvious which of the two evolution equations gives the predominant behaviour of the gluon distribution in the HERA small x regime. If the gluon has the characteristic BFKL $x^{-\lambda}$ shape in x then the structure function F_2 will show the same behaviour due to the k_T-factorisation theorem. So one might think that it is possible to identify the underlying dynamics by measuring F_2. It turns out, however, that as we outlined in Section 3.1 both DGLAP and leading order BFKL dynamics allow for a description of the H1 and ZEUS data. In addition the leading order BFKL prediction for F_2 is subject to uncertainties due to the diffusion in $\ln k_T^2$ which accompanies the BFKL evolution of an input gluon distribution to smaller values of x. This diffusion can lead to a penetration of the infrared region where perturbative QCD ceases to be valid. Also subleading corrections to the BFKL equation will suppress the strong $x^{-\lambda}$ rise. It is therefore necessary to consider less inclusive quantities and to expose the deep inelastic final state [11]. Various final state measurements have been suggested in the past [74]. In

[11] In addition to investigating the deep inelastic final state it has also been suggested to study $\ln(1/x)$ effects in hadron collisions [72] and e^+e^- [73] scattering.

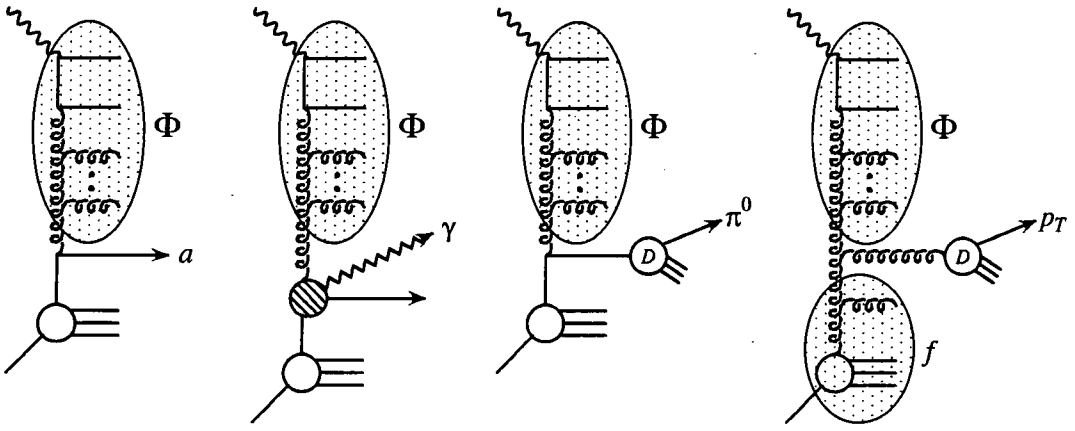

Figure 9.1: Diagrammatic representation of (a) the deep inelastic + forward jet, (b) the DIS + forward γ, (c) the DIS + forward π^0, and (d) the single particle spectrum measurement.

this thesis we studied again the original deep inelastic + forward jet process as proposed by Mueller and introduced two extensions of this idea, namely DIS + forward photon and DIS + forward π^0 events. In addition to these two projects we also studied whether single particle transverse momentum spectra can be used to identify $\ln(1/x)$ dynamics. A diagrammatic representation of the four processes is given in Fig. 9.1.

As we explained in Chapter 3 the **DIS + forward jet measurement** which is shown diagrammatically in Fig. 9.1(a) is very suitable for identifying BFKL dynamics at HERA from the theoretical point of view. It has various advantages: Firstly, since the transverse momentum of the jet is required to fulfil $k_{jT}^2 \simeq Q^2$ where Q^2 is not too small, DGLAP evolution along the gluon chain is neutralized and a penetration of the infrared region due to the diffusion in $\ln k_T^2$ is avoided. Secondy, because the longitudinal momentum fraction x_j of the jet is chosen to be large while x is small, the $(x/x_j)^{-\lambda}$ behaviour as $x/x_j \to 0$ can be studied. Furthermore input parton distributions are only needed at values of x_j where they are well-known from the global analyses. On the other hand, experimentally the DIS + jet measurement proves very difficult since jets with large longitudinal momentum $x_j p$ are emitted close to the proton direction and therefore are hard to identify and to measure accurately. Nevertheless, experimental results have been obtained by the H1 and ZEUS collaborations. In Chapter 6 we compared the H1 DIS + jet data with predictions

obtained including and neglecting BFKL dynamics in the calculation. We found that only the BFKL based prediction yields a good description of the data and therefore concluded that the H1 data show signs of BFKL soft gluon resummation. As a check it will be useful to compare also with the ZEUS results which are for slightly different cuts and which have very recently been shown in preliminary form. On the experimental side data for a higher cut on the transverse momentum of the jet and smaller angles of the jet with respect to the proton direction would of course be helpful. Nevertheless the results already look very promising for studying $\ln(1/x)$ resummation effects.

Since the DIS + jet measurement is experimentally difficult, in Chapter 4 we proposed an alternative process, namely **deep inelastic events containing an identified forward photon**, see Fig. 9.1(b). This process has the advantage that the measurement of a photon is cleaner than that of a jet, and less ambiguous, particularly at the lower values of k_T. Furthermore since the quark or antiquark jet is not identified events can be included in the data sample in which its constituents mingle with the proton remnants. On the other hand the DIS + γ cross section is suppressed relative to DIS + jet due to the additional electromagnetic coupling and because isolation of the photon has to be required to ensure that it does not origin in the decay of a π^0 in the jet. Our study showed that for the set of cuts which we imposed we lose about a factor 400 in going from the DIS + jet to the DIS + γ measurement. At present HERA luminosities the DIS + γ rate is too small to be measured. If luminosities of the order of 1 fb^{-1} could be reached the DIS + γ process should allow an identification of the underlying dynamics.

Despite the fact that the DIS + γ rate turned out to be quite small, nevertheless it prompted another and more promising possibility. To be specific, in Chapter 5 we proposed another final state measurement which is a modification of the original DIS + jet process. We suggested that the forward jet is identified through the measurement of a single energetic decay product, the π^0 as shown in Fig. 9.1(c). Just like the DIS + γ process, **DIS + forward π^0** has the advantage that a π^0 is easier to identify than a jet but it should have a much higher rate. In Chapter 5 we performed an exploratory study of this process investigating whether it could be used to identify $\ln(1/x)$ dynamics at HERA. Our results prompted the H1 collaboration to look at this process and indeed

preliminary data have just become available. As a consequence, in Chapter 7 we updated our π^0 prediction taking advantage of the new H1 DIS + jet data. Note that the functions Φ_i which describe the gluon ladder coupling to the virtual photon are the same for the DIS + π^0 process as for DIS + jet, as is indicated by shaded blobs in Fig. 9.1. Therefore we fixed the normalisation of the BFKL prediction for DIS + π^0 by adjusting the parameters determining the Φ_i so that the resulting DIS + jet cross section agreed with the H1 data. We found that the DIS + π^0 rate for the H1 experimental cuts is of the same order as the DIS + jet rate and therefore measureable at HERA. The BFKL based π^0 prediction somewhat overestimates the preliminary H1 data. This may be due to the low experimental cuts on the π^0 momenta as a consequence of which we may be evaluating the fragmentation functions in regions where they are not valid. Work on the comparison between the BFKL prediction and the H1 data is still in progress. Now that the DIS + π^0 rate is measureable at HERA this process should be better suited to identify the underlying dynamics than the original DIS + jet process since it is a lot cleaner.

In the measurements discussed above we tried to identify $\ln(1/x)$ dynamics focussing on the BFKL $x^{-\lambda}$ behaviour of the observables. On the other hand we could also search for effects which are due to the diffusion in $\ln k_T^2$ along the BFKL ladder. The study of **single particle transverse momentum spectra** (see Fig. 9.1(d)) is based on the idea that due to this diffusion particles with high transverse momentum can be emitted in the central region between the current jet and the proton remnant. In DGLAP dynamics the transverse momenta of the gluons are strongly ordered and therefore the emission of a high transverse momentum particle is suppressed by the fragmentation functions. In comparison with the E_T flow measurement the single particle spectrum at sufficiently large values of p_T has the advantage that it is less affected by hadronisation effects and should reflect the diffusion along the BFKL ladders more obviously. In Chapter 8 we calculated the single particle spectrum fixing the normalisation of the BFKL prediction in the same way as for the DIS + π^0 process. We then compared the BFKL prediction with the data published by the H1 collaboration in the beginning of this year and found excellent agreement in both the shape and the normalisation. We therefore concluded that we discovered signatures of $\ln(1/x)$ resummation and the diffusion in $\ln k_T^2$ along the

BFKL ladders. Clearly data for higher values of p_T would be useful.

The studies presented in this thesis were based on leading order BFKL dynamics. Therefore, in principle, next-to-leading order corrections should be included in the calculations. These important effects are somewhat neutralized in the results which we presented in Chapters 7 and 8 since there we normalize the BFKL function Φ to the available DIS + jet data. Indeed the predictions for the DIS + jet cross section and the single particle spectra show excellent agreement with the data. This means that we found signs for BFKL resummation effects and the diffusion in $\ln k_T^2$ which accompanies the evolution to small x. Research on the deep inelastic final state will remain a hot topic and should allow for a clear identification of the underlying dynamics at HERA as both the theory and experiment develop and improve.

Appendix A

Analytic solution of the BFKL equation for fixed coupling

The leading order BFKL equation was written for fixed coupling constant. In this case it is possible to solve the equation analytically as we will demonstrate in this appendix [12]. We start by calculating the Mellin transform of f which is given by

$$\tilde{f}(x,\omega) \equiv \int_0^\infty dk_T^2 \, (k_T^2)^{-\omega-1} \, f(x,k_T^2). \tag{A.1}$$

We will see that this has the advantage that the BFKL equation (2.21) factorizes. Applying the Mellin transform technique we find

$$\begin{aligned}
\frac{\partial \tilde{f}(x,\omega)}{\partial \ln(1/x)} &= \int_0^\infty dk_T^2 \, (k_T^2)^{-\omega-1} \, \frac{\partial f(x,k_T^2)}{\partial \ln(1/x)} \\
&= \overline{\alpha}_S \int_0^\infty dk_T^2 \, (k_T^2)^{-\omega-1} \\
&\quad \times \int_0^\infty dk_T'^2 \, \frac{k_T^2}{k_T'^2} \left\{ \frac{f(x,k_T'^2) - f(x,k_T^2)}{|k_T'^2 - k_T^2|} + \frac{f(x,k_T^2)}{[4k_T'^4 + k_T^4]^{\frac{1}{2}}} \right\} \\
&\equiv \overline{\alpha}_S \int_0^\infty dk_T^2 \, (k_T^2)^{-\omega-1} \, \mathcal{I},
\end{aligned} \tag{A.2}$$

say. Substituting $u \equiv k_T'^2/k_T^2$ then yields

$$\begin{aligned}
\mathcal{I} &= \int_0^\infty du \, k_T^2 \, \frac{1}{u} \left\{ \frac{f(x,uk_T^2) - f(x,k_T^2)}{|k_T^2 u - k_T^2|} + \frac{f(x,k_T^2)}{[4k_T^4 u^2 + k_T^4]^{\frac{1}{2}}} \right\} \\
&= f(x,k_T^2) \int_0^\infty \frac{du}{u} \left\{ \frac{f(x,k_T^2 u)/f(x,k_T^2) - 1}{|u-1|} + \frac{1}{[4u^2+1]^{\frac{1}{2}}} \right\}
\end{aligned} \tag{A.3}$$

[12] A brief outline of this calculation is also given in ref. [7].

where $f(x,k_T^2u)/f(x,k_T^2) = u^\omega$. This can easily be shown by expressing $f(x,k_T^2)$ in terms of the derivative $\partial\tilde{f}(x,k_T^2)/\partial k_T^2$ and obtaining the analogous equation for $f(x,uk_T^2)$. We now have

$$\mathcal{I} \;=\; f(x,k_T^2)\,\frac{\tilde{K}(\omega)}{\overline{\alpha}_S} \tag{A.4}$$

where $\tilde{K}$ is the Mellin transform of the BFKL kernel K,

$$\tilde{K}(\omega) \;=\; \overline{\alpha}_S \int_0^\infty \frac{du}{u}\left\{\frac{u^\omega-1}{|u-1|} - \frac{1}{[4u^2+1]^{\frac{1}{2}}}\right\}. \tag{A.5}$$

Substituting $\mathcal{I}$ into (A.2) we find the BFKL equation for $\tilde{f}$,

$$\frac{\partial\tilde{f}(x,\omega)}{\partial\ln(1/x)} \;=\; \tilde{K}(\omega)\,\tilde{f}(x,\omega), \tag{A.6}$$

which factorizes as anticipated. The next step is to evaluate the integral over u in (A.5). We perform this calculation of $\tilde{K}(\omega)$ in Appendix B with the result

$$\tilde{K}(\omega) \;=\; \overline{\alpha}_S\,[2\Psi(1) - \Psi(\omega) - \Psi(1-\omega)] \tag{A.7}$$

where $\Psi(\omega) \equiv \Gamma'(\omega)/\Gamma(\omega)$. Now we are in the position to solve the BFKL equation (A.6). The solution has the form

$$\begin{aligned}\tilde{f}(x,\omega) \;&=\; \tilde{f}(x_0,\omega)\,\exp\left[\tilde{K}(\omega)\ln\left(\frac{x_0}{x}\right)\right] \\ &=\; \tilde{f}(x_0,\omega)\,\left(\frac{x}{x_0}\right)^{-\tilde{K}(\omega)}\end{aligned} \tag{A.8}$$

with $\tilde{f}(x_0,\omega)$ some input distribution. Having solved the BFKL equation for $\tilde{f}(x,\omega)$ our aim is to use our knowledge of $\tilde{f}$ to derive an expression for the solution $f(x,k_T^2)$ of the original BFKL equation (2.21). We therefore perform the inverse Mellin transform

$$\begin{aligned}f(x,k_T^2) \;&=\; \frac{1}{2\pi i}\int_{c-i\infty}^{c+i\infty} d\omega\,(k_T^2)^\omega\,\tilde{f}(x,\omega) \\ &=\; \frac{1}{2\pi i}\int_{c-i\infty}^{c+i\infty} d\omega\,(k_T^2)^\omega\,\tilde{f}(x_0,\omega)\,\left(\frac{x}{x_0}\right)^{-\tilde{K}(\omega)}.\end{aligned} \tag{A.9}$$

To further simplify this equation we have to evaluate $\tilde{f}(x_0,\omega)$ and the exponent $\tilde{K}(\omega)$ in turn. It is convenient to start with the former by Taylor expanding about the point

$\omega = 1/2$ which yields

$$\tilde{f}(x_0,\omega) \simeq \tilde{f}\left(x_0,\frac{1}{2}\right)\left[1+\left(\omega-\frac{1}{2}\right)\frac{1}{\tilde{f}}\frac{d\tilde{f}}{d\omega}+\frac{\left(\omega-\frac{1}{2}\right)^2}{2}\frac{1}{\tilde{f}}\frac{d^2\tilde{f}}{d\omega^2}+\mathcal{O}(\omega^3)\right]. \tag{A.10}$$

Next we substitute

$$i\nu \equiv \omega-\frac{1}{2} \tag{A.11}$$

and define

$$\ln \overline{k}_T^2 \equiv -\frac{1}{\tilde{f}}\frac{d\tilde{f}}{d\omega}, \qquad A \equiv \frac{1}{\tilde{f}}\frac{d^2\tilde{f}}{d\omega^2} \tag{A.12}$$

which will prove useful later. Then we find

$$\tilde{f}(x_0,\omega) \simeq \tilde{f}(x_0,\frac{1}{2})\left[1-i\nu\ln\overline{k}_T^2-\frac{1}{2}\nu^2 A\right] \tag{A.13}$$

which we consider as our final result for $\tilde{f}(x_0,\omega)$. We also rewrite $(k_T^2)^\omega$ utilizing the substitution (A.11) and obtain

$$(k_T^2)^\omega = (k_T^2)^{\frac{1}{2}+i\nu} = (k_T^2)^{\frac{1}{2}}\exp(i\nu\ln k_T^2). \tag{A.14}$$

Now we turn to the Mellin transform $\tilde{K}(\omega)$ of the BFKL kernel. Substitution (A.11) and Taylor expansion about $\omega = 1/2$ yield

$$\tilde{K}\left(\frac{1}{2}+i\nu\right) \simeq \tilde{K}\left(\frac{1}{2}\right)+i\nu\frac{\partial\tilde{K}\left(\frac{1}{2}\right)}{\partial\omega}+\frac{(i\nu)^2}{2}\frac{\partial^2\tilde{K}\left(\frac{1}{2}\right)}{\partial\omega^2}+\mathcal{O}((i\nu)^3). \tag{A.15}$$

Choosing $\lambda = \tilde{K}(\frac{1}{2})$ as an eigenvalue of $\tilde{K}$ and keeping only real terms

$$\tilde{K}\left(\frac{1}{2}+i\nu\right) \simeq \lambda-\frac{\lambda''\nu^2}{2}. \tag{A.16}$$

On the other hand we also have expression (A.7) for $\tilde{K}$ where we can perform the same substitution (A.11). We then Taylor expand the Ψ functions about $1/2$ and again only keep the real contributions which gives

$$\tilde{K}\left(\frac{1}{2}+i\nu\right) \simeq \overline{\alpha}_S\left[2\Psi(1)-2\Psi\left(\frac{1}{2}\right)+\nu^2\Psi''\left(\frac{1}{2}\right)\right]. \tag{A.17}$$

On utilizing $\Psi(1) = -\gamma_E$, the Euler-Mascheroni constant, and $\Psi(\frac{1}{2}) = -\gamma_E - 2\ln 2$ and equating with (A.16) we find

$$\lambda-\frac{\lambda''\nu^2}{2} = \overline{\alpha}_S\left[4\ln 2+\nu^2\Psi''\left(\frac{1}{2}\right)\right]. \tag{A.18}$$

Since the eigenvalue

$$\begin{aligned}\lambda &= \tilde{K}\left(\frac{1}{2}\right) = \bar{\alpha}_S \left[2\Psi(1) - 2\Psi\left(\frac{1}{2}\right)\right] \\ &= \frac{3\alpha_S}{\pi} 4\ln 2 \end{aligned} \tag{A.19}$$

its second derivative

$$\lambda'' = -\frac{3\alpha_S}{\pi} 2\Psi''\left(\frac{1}{2}\right). \tag{A.20}$$

We can try to further simplify this expression by taking into account the integral form of the Ψ function [75],

$$\Psi(z) = \int_0^\infty dt \, \frac{e^{-t} - e^{-zt}}{1 - e^{-t}} - \gamma_E. \tag{A.21}$$

We calculate the second derivative of Ψ and substitute $x = -t/2$ which yields

$$\Psi''\left(\frac{1}{2}\right) = -8 \int_0^\infty dx \, \frac{x^2 e^x}{e^{2x} - 1}. \tag{A.22}$$

If we now note that the ζ function has the integral representation

$$\zeta(z) = \frac{2^z}{(2^z - 1)\Gamma(z)} \int_0^\infty dx \frac{x^{z-1} e^x}{e^{2x} - 1} \tag{A.23}$$

for $\Re(z) > 1$ which when evaluated at $z = 3$ results in

$$\zeta(3) = \frac{4}{7} \int_0^\infty dx \, \frac{x^2 e^x}{e^{2x} - 1} \tag{A.24}$$

we finally find

$$\Psi''\left(\frac{1}{2}\right) = -14\zeta(3). \tag{A.25}$$

Therefore the second derivative of the eigenvalue of the Mellin transformed BFKL kernel

$$\lambda'' = \frac{3\alpha_S}{\pi} 28\zeta(3) \tag{A.26}$$

where $\zeta(3) = 1.202$. We can now return to the expression (A.9) for the solution f of the BFKL equation in terms of $\tilde{f}$ and substitute (A.13) for $\tilde{f}(x_0, \omega)$, (A.14) for $(k_T^2)^\omega$ and (A.16) for $\tilde{K}(\omega)$ which yields

$$\begin{aligned} f(x, k_T^2) = \frac{1}{2\pi i} \int_{c-i\infty}^{c+i\infty} d\omega \, \Big\{ &(k_T^2)^{\frac{1}{2}} \exp(i\nu \ln k_T^2) \, \tilde{f}\left(x_0, \frac{1}{2}\right) \\ &\times \left[1 - i\nu \ln \overline{k}_T^2 - \frac{\nu^2 A}{2}\right] \left(\frac{x}{x_0}\right)^{-\lambda + \lambda'' \nu^2/2} \Big\}. \end{aligned} \tag{A.27}$$

The final step is to notice that the integrand has a saddle point at $\omega = \frac{1}{2} + i\nu$ with $\nu = 0$ and to perform the saddle point integration. We again substitute $\omega = \frac{1}{2} + i\nu$ leading to

$$f(x,k_T^2) = \frac{1}{2\pi}\int_{-\infty}^{\infty} d\nu \left\{ (k_T^2)^{\frac{1}{2}} \exp(i\nu \ln k_T^2)\, \tilde{f}\Big(x_0, \frac{1}{2}\Big) \times \left[1 - i\nu \ln \overline{k}_T^2 - \frac{\nu^2 A}{2}\right] \left(\frac{x}{x_0}\right)^{-\lambda+\lambda''\nu^2/2} \right\}. \tag{A.28}$$

Rewriting this expression using $\exp(-x) \simeq 1 - x + x/2$ yields

$$f(x,k_T^2) = \left(\frac{x}{x_0}\right)^{-\lambda} \frac{\tilde{f}\Big(x_0,\frac{1}{2}\Big)\,(k_T^2)^{\frac{1}{2}}}{2\pi} \int_{-\infty}^{\infty} d\nu \times \exp\left[i\nu \ln k_T^2 + \nu^2 \frac{\lambda''}{2} \ln\Big(\frac{x}{x_0}\Big) - i\nu \ln \overline{k}_T^2 - \frac{\nu^2 A}{2}\right] \tag{A.29}$$

which can be evaluated taking into account that the integral

$$\int_{-\infty}^{\infty} d\nu\, \exp(-a\nu^2 + ib\nu) = \int_{-\infty}^{\infty} d\nu\, \exp\left[-a\left(\nu + \frac{ib}{2a}\right)^2\right] \exp\left[-\frac{b^2}{4a}\right] = \sqrt{\frac{\pi}{a}} \exp\left[-\frac{b^2}{4a}\right]. \tag{A.30}$$

Then setting

$$a \equiv \frac{\lambda''}{2} \ln\Big(\frac{x}{x_0}\Big) + \frac{A}{2} \tag{A.31}$$

$$b \equiv \ln\left(\frac{k_T^2}{\overline{k}_T^2}\right) \tag{A.32}$$

we finally find that $f(x,k_T^2)$ is given by (2.43).

Appendix B

Calculation of the Mellin transform of the BFKL kernel

In this appendix we give a derivation of equation (2.40) for the Mellin transformed BFKL kernel [13]. Our aim is to evaluate the singular integral (A.5) which we obtained in Appendix A,

$$\tilde{K}(\omega) \;=\; \overline{\alpha}_S \int_0^\infty \frac{du}{u} \left\{ \frac{u^\omega - 1}{|u-1|} - \frac{1}{[4u^2+1]^{\frac{1}{2}}} \right\}.$$

It proves useful to isolate the singularities at $u = 0, 1$ by splitting the kernel into two parts,

$$\tilde{K} \;=\; \frac{3\alpha_S}{\pi} (\tilde{K}_1 + \tilde{K}_2), \tag{B.1}$$

where

$$\tilde{K}_1(\omega) \;=\; \int_1^\infty \frac{du}{u} \frac{u^\omega - 1}{u-1} \tag{B.2}$$

$$\tilde{K}_2(\omega) \;=\; \lim_{\epsilon,\delta \to 0+} \left[\int_0^1 \frac{du}{u^{1-\epsilon}} \frac{u^\omega}{(1-u)^{1-\delta}} - \int_0^1 \frac{du}{u^{1-\epsilon}} \frac{1}{(1-u)^{1-\delta}} + \int_0^\infty \frac{du}{u^{1-\epsilon}} \frac{1}{\sqrt{4u^2+1}} \right]. \tag{B.3}$$

ϵ and δ regulate any divergence of the integrals as $u \to 0, 1$. The plan is now to evaluate each integral separately. Let us start with $\tilde{K}_1$ which is somewhat easier. As a first step

[13] This derivation is briefly outlined in ref. [76].

we substitute $v = 1/u$ leading to

$$\tilde{K}_1(\omega) \;=\; -\int_0^1 dv\, \frac{v^{-\omega}-1}{v-1}. \tag{B.4}$$

It is possible to express this in terms of the Ψ function which is defined as [77]

$$\Psi \;=\; \frac{\Gamma'(z)}{\Gamma(z)} \;=\; \int_0^1 dt\, \frac{t^{z-1}-1}{t-1} \;-\; \gamma_E \tag{B.5}$$

where γ_E is the Euler-Mascheroni constant, $\gamma_E = -\Psi(1)$. Setting $z - 1 = -\omega$ we obtain

$$\tilde{K}_1(\omega) \;=\; \Psi(1-\omega) - \Psi(1). \tag{B.6}$$

$\tilde{K}_2(\omega)$ can be evaluated in terms of β functions utilizing [75]

$$\beta(x,y) \;=\; \int_0^1 dt\, t^{x-1}(1-t)^{y-1} \tag{B.7}$$

$$\beta(x,y) \;=\; 2\int_0^\infty dt\, \frac{t^{2x-1}}{(1+t^2)^{x+y}}. \tag{B.8}$$

In this way we find

$$\tilde{K}_2(\omega) \;=\; \lim_{\epsilon,\delta\to 0^+} \left[2^{-\epsilon-1}\beta\Big(\frac{\epsilon}{2}, \frac{1}{2} - \frac{\epsilon}{2}\Big) \;+\; \beta(\omega+\epsilon,\delta) \;-\; \beta(\epsilon,\delta)\right] \tag{B.9}$$

which we rewrite using the definition of the β function,

$$\beta(x,y) \;=\; \frac{\Gamma(x)\Gamma(y)}{\Gamma(x+y)} \;=\; \frac{\Gamma(x+1)\Gamma(y)}{x\Gamma(x+y)}. \tag{B.10}$$

We then see the pole structure of $\tilde{K}_2$ in ϵ and δ explicitely:

$$\begin{aligned}
\tilde{K}_2(\omega) \;&=\; \lim_{\epsilon,\delta\to 0^+} \left[2^{-\epsilon}\, \frac{\Gamma\left(\frac{\epsilon}{2}+1\right)\Gamma\left(\frac{1}{2}-\frac{\epsilon}{2}\right)}{\Gamma\left(\frac{1}{2}\right)}\, \frac{1}{\epsilon} \;+\; \frac{\Gamma(\delta+1)\,\Gamma(\omega+\epsilon)}{\Gamma(\omega+\epsilon+\delta)}\, \frac{1}{\delta}\right. \\
&\qquad \left. -\; \frac{\Gamma(1+\epsilon)\,\Gamma(1+\delta)}{\Gamma(1+\epsilon+\delta)}\, \frac{(\epsilon+\delta)}{\epsilon\delta}\right] \\
&\equiv\; \tilde{K}_{2a}(\omega) \;+\; \tilde{K}_{2b}(\omega) \;+\; \tilde{K}_{2c}(\omega),
\end{aligned} \tag{B.11}$$

say. Now we have to take the limits $\epsilon, \delta \to 0^+$. We begin with the limit in ϵ considering all three terms in (B.11) separately. Using the Taylor expansion

$$\Gamma(z+\epsilon) = \Gamma(z) + \epsilon\Gamma'(z) + \mathcal{O}(\epsilon^2) \tag{B.12}$$

on taking the limit $\epsilon \to 0^+$ the second term simply gives

$$\tilde{K}_{2b}(\omega) \;=\; \lim_{\delta\to 0^+} \frac{1}{\delta}\,\frac{\Gamma(\delta+1)\Gamma(\omega)}{\Gamma(\omega+\delta)}. \tag{B.13}$$

Proceeding analogously for the first and third term in (B.11) utilizing $2^{-\epsilon} \simeq 1-\epsilon\ln 2$ and $\Gamma(1+\epsilon)\simeq 1-\gamma_E\epsilon$ and noting that

$$[\Gamma(1+\epsilon+\delta)]^{-1} \;\simeq\; [\Gamma(1+\delta)]^{-1}\,[1-\epsilon\Psi(1+\delta)] \tag{B.14}$$

we obtain

$$\begin{aligned}\tilde{K}_{2a}(\omega)+\tilde{K}_{2c}(\omega) \;=\; \lim_{\epsilon,\delta\to 0^+} \frac{1}{\epsilon}\Big\{&[1-\epsilon\ln 2]\left[1-\gamma_E\frac{\epsilon}{2}\right]\left[1-\frac{\epsilon}{2}\Psi\left(\frac{1}{2}\right)\right]\\ &-\;[1-\gamma_E\epsilon]\,[1-\epsilon\Psi(1+\delta)]\left[1+\frac{\epsilon}{\delta}\right]\Big\}\end{aligned} \tag{B.15}$$

to $\mathcal{O}(\epsilon)$. Now we take the limit in ϵ and keep only the finite part which leads to

$$\begin{aligned}\tilde{K}_{2a}(\omega)+\tilde{K}_{2c}(\omega) \;&=\; \lim_{\delta\to 0^+}\left[-\ln 2-\frac{\gamma_E}{2}-\frac{\Psi(1/2)}{2}+\gamma_E+\Psi(1+\delta)-\frac{1}{\delta}\right]\\ &=\; \lim_{\delta\to 0^+}\left[-\Psi(1)+\Psi(1+\delta)-\frac{1}{\delta}\right].\end{aligned} \tag{B.16}$$

where we replaced $\Psi(1/2)$ by $-\gamma_E-2\ln 2$. The final step is to evaluate the limit $\delta\to 0^+$ in (B.13) and (B.16) in a similar way as we just described for ϵ again only retaining the finite part. The result is

$$\tilde{K}_2(\omega) \;=\; \Psi(1)-\Psi(\omega) \tag{B.17}$$

which on combining with $\tilde{K}_1(\omega)$ as given in (B.6) yields (2.40).

Bibliography

[1] I. J. R. Aitchison and A. J. G. Hey, *Gauge theories in particle physics*, Adam Hilger (1989).

[2] A. D. Martin, Contemporary Physics **36** (1995) 335.

[3] M. Gell-Mann, Phys. Lett. **8** (1964) 214.

[4] G. Zweig, CERN preprints 8182/TH.401, 8419/TH.412 (1964).

[5] O. Nachtmann, *Elementary particle physics*, Springer (1989).

[6] F. Halzen and A. D. Martin, *Quarks and leptons*, Wiley (1984).

[7] A. D. Martin, Proceedings of the 1993 European school of high-energy physics, ed. by N. Ellis and M. B. Gavela, Addendum, CERN yellow report no. 94-04.

[8] M. R. Pennington, *Cornerstones of QCD*, Rep. Prog. Phys. **46** (1983) 393.

[9] R. P. Feynman, *Photon Hadron Interactions*, W. A. Benjamin (1972).

[10] J. D. Bjorken, Phys. Rev. **179** (1969) 1547.

[11] S. Brodsky and G. Farrar, Phys. Rev. Lett. **31** (1973) 1153.

[12] P. J. Sutton, Proceedings of the 36th Cracow School of Theoretical Physics, Acta Phys. Polon. **B27** (1996) 3481.

[13] J. R. Forshaw and D. A. Ross, *Quantum chromodynamics and the pomeron*, Cambridge University Press (1997).

[14] See for example:
SLAC-MIT collaboration, G. Miller et al., Phys. Rev. **D5** (1972) 528.

[15] Results of measurements of the proton structure function F_2 in fixed target experiments can be found in:
BCDMS collaboration: A. C. Benvenuti et al., Phys. Lett. **223** (1989) 485;
WA25 collaboration: D. Allasia et al., Z. Phys. **C28** (1991) 321;
E665 collaboration: M. R. Adams et al., Phys. Rev. **D54** (1996) 3006;
EMC collaboration: J. J. Aubert et al., Nucl. Phys. **B259** (1985) 189; K. A. Bazizi et al., CERN preprint CERN-PPE/90-175 (1990);
NMC collaboration: M. Arneodo et al., Phys. Lett. **B364** (1995) 107;
SLAC: L. W. Whitlow, Ph.D. Thesis, Stanford University, 1990.

[16] The results of the most recent HERA measurement of F_2 can be found in:
H1 collaboration: S. Aid et al., Nucl. Phys. **B470** (1996) 3;
ZEUS collaboration: M. Derrick et al., Z. Phys. **C69** (1996) 607; Z. Phys. **C72** (1996) 399.

[17] R. K. Ellis, W. J. Stirling and B. R. Webber, *QCD and Collider Physics*, Cambridge University Press (1996).

[18] Yu. Dokshitzer, Sov. Phys. JETP **46** (1977) 641.

[19] V. N. Gribov and L. N. Lipatov, Sov. J. Nucl. Phys. **15** (1972) 438, 675;
G. Altarelli and G. Parisi, Nucl. Phys. **B126** (1977) 298.

[20] G. Curci, W. Furmanski and R. Petronzio, Nucl. Phys. **B175** (1980) 27.
W. Furmanski and R. Petronzio, Phys. Lett. **B97** (1980) 437; Z. Phys. **C11** (1982) 293.

[21] A. D. Martin, R. G. Roberts and W. J. Stirling, Phys. Lett. **B387** (1996) 419.

[22] A. D. Martin, R. G. Roberts and W. J. Stirling, Phys. Rev. **D50** (1994) 6734; Phys. Lett. **B354** (1995) 155.

[23] CTEQ: H. L. Lai et al., Phys. Rev. **D51** (1995) 4763; Phys. Rev. **D55** (1997) 1280.

[24] M. Glück, E. Reya and A. Vogt, Z. Phys. **C67** (1995) 433.

[25] J. Kwiecinski, A. D. Martin, R. G. Roberts and W. J. Stirling, Phys. Rev. **D42** (1990) 3645.

[26] E. A. Kuraev, L. N. Lipatov and V. Fadin, Zh. Eksp. Teor. Fiz. **72** (1977) 373 [Sov. Phys. JETP **45** (1977) 199];
Ya. Ya. Balitskij and L. N. Lipatov, Yad. Fiz. **28** (1978) 1597 [Sov. J. Nucl. Phys. **28** (1978) 822];
L. N. Lipatov, in *Perturbative QCD*, ed. by A. H. Mueller, World Scientific, Singapore (1989), p. 441;
J. B. Bronzan and R. L. Sugar, Phys. Rev. **D17** (1978) 585.

[27] L. V. Gribov, E. M. Levin and M. G. Ryskin, Phys. Rep. **100** (1983) 1.

[28] T. Jaroszewicz, Acta Phys. Polon. **B11** (1980) 965.

[29] A. Donnachie and P. V. Landshoff, Phys. Lett. **B296** (1992) 257.

[30] A. J. Askew, J. Kwiecinski, A. D. Martin and P. J. Sutton, Phys. Rev. **D49** (1994) 4402.

[31] V. Del Duca, Proceedings of the 5th International Workshop on "Deep Inelastic Scattering and QCD" (DIS 97), Chicago, USA, June 1997.

[32] V. S. Fadin, Proceedings of the 5th International Workshop on "Deep Inelastic Scattering and QCD" (DIS 97), Chicago, USA, June 1997.

[33] M. Ciafaloni and G. Camici, contribution to the workshop "New Trends in HERA Physics", Ringberg, Germany, May 1997.

[34] J. R. Forshaw, P. N. Harriman and P. J. Sutton, Nucl. Phys. **B416** (1994) 739; J. Phys. **G19** (1993) 1616.

[35] M. Ciafaloni, Nucl. Phys. **B296** (1988) 49;
B. Andersson, G. Gustafson and J. Samuelsson, Nucl. Phys. **B467** (1996) 443.

[36] J. Kwiecinski, A. D. Martin and P. J. Sutton, Z. Phys. **C71** (1996) 585.

[37] J. Kwiecinski, Proceedings of the 32nd Internationale Universitätswochen für Kern- und Teilchenphysik, Schladming, Austria, 1993, Springer.

[38] E. M. Levin and M. G. Ryskin, Phys. Rep. **189** (1990) 267.

[39] A. H. Mueller, Nucl. Phys. B (Proc. Suppl.) **18C** (1990) 125; J. Phys. **G17** (1991) 1443.

[40] A. D. Martin, Proceedings of the 33rd Cracow School of Theoretical Physics, Acta Phys. Polon. **B25** (1994) 265.

[41] A. J. Askew, J. Kwiecinski, A. D. Martin and P. J. Sutton, Phys. Rev. **D47** (1993) 3775.

[42] S. Catani, M. Ciafaloni and F. Hautmann, Phys. Lett. **B242** (1990) 97; Nucl. Phys. **B366** (1991) 135;
J. C. Collins and R. K. Ellis, Nucl. Phys. **B360** (1991) 3;
E. M. Levin, M. G. Ryskin, Yu. M. Shabelskii and A. G. Shuvaev, Sov. J. Nucl. Phys. **53** (1991) 657.

[43] J. Bartels and H. Lotter, Phys. Lett. **B309** (1993) 400.

[44] W. K. Tang, Phys. Lett. **B278** (1992) 363.

[45] J. Bartels, A. De Roeck and M. Loewe, Z. Phys. **C54** (1992) 635.

[46] A. De Roeck, Nucl. Phys. B (Proc. Suppl.) **29A** (1992) 61.

[47] J. Kwiecinski, A. D. Martin and P. J. Sutton, Phys. Lett. **B287** (1992) 254.

[48] J. Kwiecinski, A. D. Martin and P. J. Sutton, Phys. Rev. **D46** (1992) 921.

[49] J. Kwiecinski, A. D. Martin and P. J. Sutton, Nucl. Phys. B (Proc. Suppl.) **29A** (1992) 67.

[50] C. Catani, M. Ciafaloni and F. Hautmann, Proceedings of the workshop "Physics at HERA", held at DESY in Oct. 1991, ed. by W. Buchmüller and G. Ingelman, Hamburg, Germany, 1992.

[51] M. Klein, Proceedings of the workshop "Physics at HERA", held at DESY in Oct. 1991, ed. by W. Buchmüller and G. Ingelman, Hamburg, Germany, 1992.

[52] J. Bartels, M. Besancon, A. De Roeck and J. Kurzhoefer, Proceedings of the workshop "Physics at HERA", held at DESY in Oct. 1991, ed. by W. Buchmüller and G. Ingelman, Hamburg, Germany, 1992.

[53] P. J. Sutton, Ph.D. Thesis, Durham University, 1992.

[54] H1 collaboration: S. Aid et al., Phys. Lett. **B356** (1995) 118.

[55] H1 Collaboration, C. Adloff et al., contributed paper pa03-049, ICHEP '96, Warsaw, Poland, July 1996.

[56] S. Wölfle, on behalf of the ZEUS collaboration, Proceedings of the 5th International Workshop on "Deep Inelastic Scattering and QCD" (DIS 97), Chicago, USA, June 1997.

[57] J. Bartels, V. Del Duca, A. De Roeck, D. Graudenz, and M. Wüsthoff, Phys. Lett. **B384** (1996) 300.

[58] P. D. B. Collins and A. D. Martin, *Hadron Interactions*, Adam Hilger (1984).

[59] P. Chiappetta, M. Greco, J. Ph. Guillet, S. Rolli and M. Werlen, Nucl. Phys. **B412** (1994) 3.

[60] J. Binnewies, B. A. Kniehl and G. Kramer, Z. Phys. **C65** (1995) 471.

[61] J. Binnewies, B. A. Kniehl and G. Kramer, Phys. Rev. **D52** (1995) 4947.

[62] S. Rolli, Berkeley preprint LBNL-39176, Proceedings of the 31st Rencontres de Moriond, "QCD and High-Energy Hadronic Interactions", Les Arcs, France, March 1996, ed. by Jean Tran Thanh Van, Editions Frontieres (1996).

[63] *Review of Particle Physics*, R. M. Barnett et al., Phys. Rev. **D54** (1996) 1.

[64] J. F. Owens, Rev. Mod. Phys. **59** (1987) 465.

[65] J. Binnewies, private communication.

[66] M. Wobisch, on behalf of the H1 collaboration, Proceedings of the 5th International Workshop on "Deep Inelastic Scattering and QCD" (DIS 97), Chicago, USA, June 1997.

[67] M. Kuhlen, private communication.

[68] H1 collaboration, contributed paper 255 to the International Europhysics Conference on High Energy Physics, HEP 97, Jerusalem, Israel, August 1997.

[69] K. Golec-Biernat, J. Kwiecinski, A. D. Martin and P. J. Sutton, Phys. Rev. **D50** (1994) 217; Phys. Lett. **B335** (1994) 220.

[70] M. Kuhlen, Phys. Lett. **B382** (1996) 441; Proccedings of the Workshop on "Future Physics at HERA", Hamburg, Germany, 1996, hep-ex/9610004.

[71] H1 Collaboration, C. Adloff *et al.*, Nucl. Phys. **B485** (1997) 3.

[72] A review of the proposed measurements is given in:
V. T. Kim and G. B. Pivovarov, Proceedings of the VIIth Blois Workshop "Recent Advances in Hadron Physics", Seoul, Korea, June 1997, hep-ph/9709304.

[73] J. Bartels, A. De Roeck and H. Lotter, Phys. Lett. **B389** (1996) 742;
S. J. Brodsky, F. Hautmann and D. E. Soper, SLAC preprint SLAC-PUB-7480, hep-ph/9706427.

[74] See also:
A. J. Askew, D. Graudenz, J. Kwiecinski and A. D. Martin, Phys. Lett. **B338** (1994) 92;
J. Bartels, V. Del Duca and M. Wüsthoff, Z. Phys. **C76** (1997) 75.

[75] See for example:

I. S. Gradshteyn and I. M. Ryzhik, *Tables of Integrals, Series and Products*, 5th edition, Academic Press (1994).

[76] A. J. Askew, Ph.D. Thesis, Durham University, 1995.

[77] See for example:

I. N. Bronstein and K. A. Semendjajew, *Taschenbuch der Mathematik*, 24th edition in German, Harry Deutsch (1989).